Multi-core Fibre Design and Analysis using Artificial Intelligence

A thesis submitted to UCL (University College London) for the partial fulfilment of the requirements for the degree of Doctor of Philosophy (PhD)

by

Xun Mu

Optical Networks Group
Department of Electronic and Electrical Engineering
UCL (University College London)

15th October 2023

Declaration

I, Xun Mu, confirm that the work presented in this thesis is my own. Where information has been derived from other sources, I confirm that this has been indicated in the thesis.

Copyright Notice

Abstract

The emerging cloud services and communication/computation applications exponentially increase data traffic and demand, exceeding the standard single-mode fibre's capacity. It renders the development of high-capacity fibre necessary. Space Division Multiplexing (SDM), as one of the auspicious solutions, has been intensively researched in the past decade. Among the members in SDM, the single-mode Multi-Core Fibre (MCF) in standard cladding diameter has the highest potential to be applied in the existing fibre transmission systems. It can prevent complex multi-input multi-output digital signal processing while having negligible inter-core Crosstalk (XT) and being compatible with the standard single-mode fibre and the relative components. Regarding the single-mode MCF design, there are multiple parameters to optimise due to several variants of the core index profile per type of core and heterogeneous structure which can lead to lower XT. Meanwhile, multiple properties need to be addressed to meet the application requirements and maintain feasibility. These make it time- and computation-consuming to optimise MCF comprehensively. Therefore, an automatic and efficient artificial intelligence-based toolkit has been proposed in this thesis for MCF design and optimisation.

In the toolkit, for the sake of computation efficiency, machine learning methods were used to do the regression of optical properties and then replace the numerical methods, which results in up to $10^6\times$ speed up. Particle Swarm Optimisation (PSO) algorithm optimises the particles which each represent one MCF structure according to the fitness value given by the objective function. Each objective function is designed to include the objective and the constraints of properties based on the application requirements. 6-core and 8-core fibres in standard cladding diameter were designed for three objectives respectively: minimising XT, maximising effective mode area, or maximising fabrication yield. Moreover, based on the optimised MCFs, the relationships between the properties and capacity also were investigated thoroughly. Further suggestions were given for future MCF design.

Keywords: *Space Division Multiplexing*, *Artificial Intelligence-based Optimisation*, *Multi-core Fibre Capacity Investigation*, *Fabrication Yield Optimisation*

Impact Statement

Fibre is an essential element in modern and future optical transmission systems, such as the data centre which is the operational core of the internet, and transatlantic and transpacific telecommunication. With the advancement of technology, the transmission systems have been scaled and new applications have been emerging simultaneously. The increasing workload of the fibre is approaching its inherent limitation. Therefore, it becomes pressing to develop some new types of fibre with higher capacity for preparing for the near-future capacity crunch. MCF is one of the most promising solutions because of its great transmission performance and compatibility with existing systems as proven in past research.

This thesis contributes to the automaticity, reliability and computation- and time-efficiency of MCF design with artificial intelligence, such as machine learning and swarm intelligence. The typical process of MCF design is mainly based on parameter sweeping and empiricism. Here a tool kit is developed including an optical property toolbox which allows estimating the optical properties of each MCF structure in around 30 μs, an optimisation toolbox which allows designing MCF for various application requirements on optical properties and/or fabrication yield and a capacity estimation toolbox.

This work has proven the feasibility of using Artificial Intelligence (AI) methods to conduct MCF design and optimisation work. Meanwhile, during the tool kit development, the relationships among the structure parameters, optical properties and transmission capacity are thoroughly analyzed resulting in a deeper understanding of the MCF properties and guidance on future MCF designs. From the standpoint of MCF manufacturers, this tool kit can significantly improve their time-efficiency when the customers require customised MCF with special properties demands and provide better MCF design compared to the traditional MCF design method. In addition, the toolkit allows people without great knowledge of MCF and/or AI to conduct MCF design.

Acknowledgements

First and foremost, I would like to express my heartfelt gratitude to my supervisor, Prof. Georgios Zervas, for providing me with the invaluable opportunity to pursue the Ph.D. degree. I am deeply grateful for his unwavering guidance, support, and profound insights throughout the entire research process. His mentorship has been instrumental in shaping my research direction, assisting me in problem-solving, and offering understanding during times of mistakes. Without his help, trust, and encouragement, I would not have achieved all that I have.

I would also like to extend my thanks to my previous second supervisor, Dr. Domanic Lavery, who has moved to Infinera, as well as my current second and third supervisors, Prof. Robert Killey and Prof. Polina Bayvel. Their exceptional expertise and dedication as researchers and supervisors have provided me with valuable support and guidance in both my research and academic journey.

My deepest appreciation goes to all the members of ONG who have accompanied me throughout the research process and my daily life over the years. I am especially grateful to Dr. Filipe M. Ferreira for sharing his profound knowledge of fiber and assisting me in paper writing, Mr. Alessandro Ottino for his valuable suggestions that have significantly shaped my research, Dr. Eric Sillekens for his invaluable help in various aspects, including coding and theoretical knowledge of transmission systems and Dr. Daniel Semrau for insightful discussions on the Gaussian noise model for capacity estimation, and. I would also like to thank Dr. Joshua Benjamin, Dr. Paris Andreades, Dr. Wenting Yi, Mr. Zichuan Zhou, and Mr. Jiaqian Yang for engaging in discussions within and beyond work, making my time in London enjoyable and memorable.

Lastly, I would like to express my deepest gratitude to my parents, Dongying Sun and Lunwen Mu, for their unwavering support and encouragement throughout this journey. I would also like to thank my friends, Dr. Xiujun Zheng, Miss Fengting Zhou, Miss Yanqin Lin, and Miss Jintao Li, for their continuous support. Additionally, I would like to offer special thanks and heartfelt condolences to my grandfather, Fanghuai Mu, who passed away in December 2019.

Table of Contents

List of Figures

List of Tables

List of Terms and Abbreviations

AI Artificial Intelligence 5, 22, 23, 67, 68, 91, 93, 110, 111, 113, 114, 126, 128, 129, 131, 138, 143–147

ANN Artificial Neural Network 68, 71

ASE Amplified Spontaneous Emission 20, 48–50, 52, 95, 105, 119

CD Chromatic Dispersion 16, 39, 81, 120, 129, 131, 135, 139, 146

CL Coating Loss 95, 110, 139

CMF Core Multiplicity Factor 47

CP core pitch 21, 94, 130

DMD differential mode dispersion 58, 147

DSP Digital Signal Processing 54, 58, 65

EDFA Erbium-doped Fibre Amplifier 53, 65

FDE Finite Difference Eigenmode 30, 74–78, 81

GA Genetic Algorithm 67, 68, 89

GeLU Gaussian Error Linear Unit 72

GFF Gain Flattening Filter 50

GN Gaussian Noise 22, 49, 51, 52, 95, 98, 104, 111, 114, 144, 146

GPU Graphics processing unit 76, 78

Hete-TA-MCF Heterogeneous Trench-assisted Fibre 42, 95, 96

Homo-TA-MCF Homogeneous Trench-assisted Fibre 44

IEC International Electrotechnical Commission 39

ISRS Inter-channel Stimulated Raman Scattering . 20, 22, 48–52, 95, 98, 104, 105, 111, 114, 122, 144, 146

JSD Jensen–Shannon divergence 135

MCF Multi-Core Fibre 4, 5, 11, 13–15, 20–24, 44–49, 53–55, 57–66, 68, 70, 78, 81, 91–97, 100–105, 107–119, 121, 122, 124–131, 135–138, 143–147

MD Mode Dispersion 53–55

MDL Mode Dependent Loss 53–55

MFD Mode Field Diameter 38, 63

MIMO Multi-input Multi-output 54, 65

ML Machine Learning 23, 68, 70, 83, 91, 128, 144, 145, 147

NF Noise Figure 119, 122

NLI Nonlinear Interference 20, 48, 51, 52, 95, 105, 107, 114, 119, 146

NN Neural Network 68

OCT Outer Cladding Thickness 46, 47, 55–57, 60–62, 115, 130

PCC Power Coupling Coefficient 44, 59, 101

PML Perfect Matching Layer 40

PSO Particle Swarm Optimisation . 4, 13, 23, 67, 68, 70, 76, 85–91, 93–95, 97, 98, 100–104, 110, 111, 115–117, 128, 130, 131, 135, 143, 144

RCF Relative Capacity Factor 109–111

RCMF Relative Core Multiplicity Factor 22, 24, 48, 58, 64, 102–104, 111, 117, 144, 146

ReLU Rectified Linear Unit 72, 76

SDM Space Division Multiplexing 4, 20, 53, 144

SGD Stochastic Gradient Descent 73

SMF Single-mode Fibre 40, 62, 66, 109

SNR Signal-to-Noise Ratio . 20, 22, 48, 52, 66, 67, 95, 98, 104, 105, 107, 109–111, 119, 124

SPM Self-phase Modulation 51

SSE spectral-spatial efficiency 122, 123, 126, 145

SSMF Standard Single-mode Fibre . . . 41, 48, 65, 66, 102, 114, 117, 119, 122, 144

STD Standard deviation 83

TA Trench-assisted . 12, 22–24, 39, 40, 42, 57, 58, 60, 63, 77, 93–95, 112, 114, 126, 138, 144, 146, 147

TRX Tranceiver Noise 52, 119

ULL Ultra-low Loss 107, 109, 111

WDM Wavelength Division Multiplexing 20, 51, 89

XPM Cross-phase Modulation 51

XT Crosstalk 4, 14, 20–24, 46, 48, 53–62, 64–66, 90, 93–96, 98, 100–105, 107–111, 113–117, 119, 121–126, 129, 130, 133–139, 144–147

Chapter 1

Introduction

1.1 Scope of the thesis

The increasing data traffic because of emerging applications, such as cloud computing and distributed deep learning, stimulates the development of Space Division Multiplexing (SDM). As one of the methods to improve the transmission capacity of optical networks, SDM has attracted intensive research interest in the past decade [3, 4, 5]. The use of SDM with Multi-Core Fibre (MCF) has revealed its ability to improve the network performance while delivering increased energy and cost efficiency [6, 7]. MCF interconnect systems have shown the potential to increase the front panel density [8] with silicon photonic on-board transceivers [9] without fan-in/out or core pitch conversion devices.

Overcoming the capacity crunch is the mission of MCFs. However, there are numerous complex and non-linear relationships between the fibre design parameters and the theoretical maximum capacity as shown in Fig. 1.1. The solid line denotes direct dependency and impact of a parameter while the dashed line denotes indirect influence. These indirect relationships bring limitations to the elements. The trade-off is needed when optimisation is conducted on the parameters influenced by indirect relationships.

The parameters that can be optimised are the index profile of each core and the core pitch between adjacent cores in the MCF design illustrated in the light-blue box at the bottom layer. They directly determine the fibre cores' optical properties: cutoff wavelength which indicates the bandwidth, effective mode area (A_{eff}) and Crosstalk (XT). Apropos of the direct dependencies, wider bandwidth leads to more Wavelength Division Multiplexing (WDM) channels. However, a wider bandwidth impacts the contribution of Nonlinear Interference (NLI) and Amplified Spontaneous Emission (ASE) to Signal-to-Noise Ratio (SNR) via the power profile which is highly influenced by the energy transfer of Inter-channel Stimulated Raman Scattering (ISRS) over the whole bandwidth. Meanwhile, the nonlinear coefficient (γ) is inversely proportional to the A_{eff} and influences NLI. XT brings a penalty on the SNR. As for the number of cores in the standard cladding diameter, higher core density means more spatial

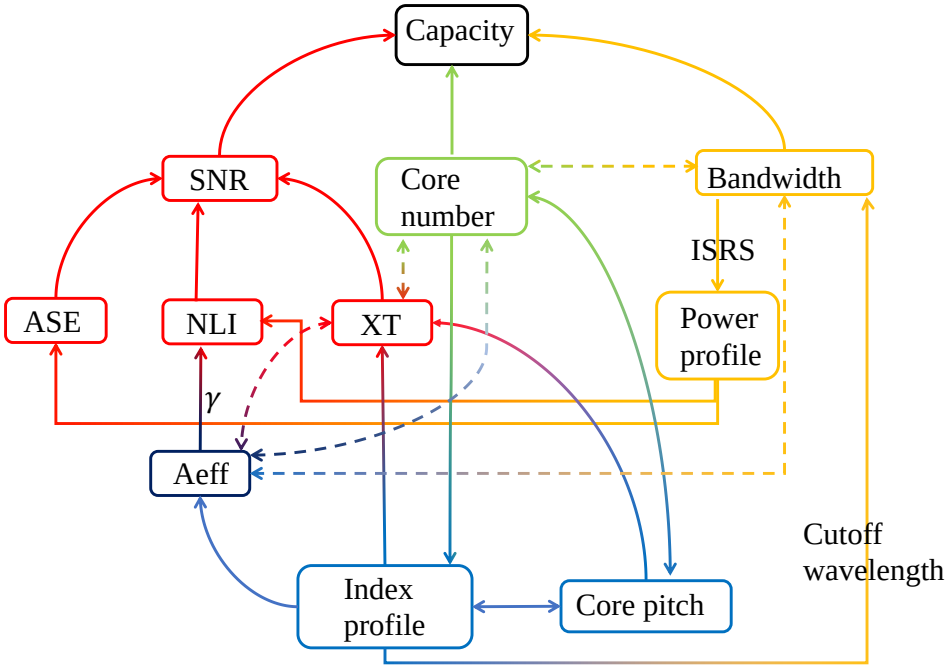

Fig. 1.1: The main factors which influence the capacity of a single-mode MCF and their relationships.

channels but will limit the choices of the index profiles and reduce the Core pitch (CP) between cores. As for the indirect relationships, the wider the bandwidth requirement is, the more limited the range of the parameters that define the index profile. Then it becomes difficult to reach large A_{eff} and low XT, simultaneously. If large A_{eff} is required, XT will stay high because of the weaker light confinement. The more cores one tries to fit in the MCF, the higher will be the inter-core XT, in this way forcing/favouring solutions with narrower cores and closer CP. Taking all these factors into consideration, the capacity of MCFs is influenced by several parameters which interact with each other directly or indirectly rendering the MCF capacity-optimisation design a multi-dimensional complex problem.

To optimise the fibre design, several index profiles and core arrangements have been proposed in the past decades. The details about them and the methods of design MCF are reviewed in Chapter 3. In an MCF, especially the heterogeneous ones, there are tens of parameters that lead to more than $\sim 10^{15}$ permutations. The brute-force method would take months to go through the permutations and find the optimal structure for each application. Thus, in the past MCF designs, most of the parameters were fixed and merely two or three parameters were considered to do optimisation. Nevertheless, it still takes a long time to calculate the optical properties and then pick some good MCF structures. Many MCF structures with great performances have been proposed and fabricated. But the automatic, reliable MCF design method is needed to save time and conduct optimisation to find out the optimal MCFs.

Additionally, the cost consumption of MCF fabrication and implementation is still

the barrier to massive production for practical use. According to the comparison between MCF design and fabrication in the literature, there is still a gap between the MCF design and fabrication because of the inevitable fabrication error, which results in yield limitation. Thus, including fabrication errors in the optimisation process and optimising MCF for optimal yield are necessary.

1.2 Key contributions

The key contributions from the work presented in this thesis are listed below:

- For the first time, an automatic and reliable Artificial Intelligence (AI)-based method is proposed for optimising heterogeneous MCF. All the index-profile parameters are treated as variables and the optimisation includes all the concerned MCF optical properties, such as A_{eff}, cutoff wavelength, chromatic dispersion, coating loss and inter-core XT. The optimisation goes through various objectives and constraint combinations and obtains optimal MCF structures with a high success ratio. The details about the method were published in [10] and [1].

- New 6-core fibres in standard cladding diameter were designed with the aforementioned method under traditional fibre cutoff estimation. Presented in Chapter 5, -92.1 dB/km ultra-low XT for the C+L band and -64 dB/km for E+S+C+L-band were obtained for 6-core fibre. Meanwhile, the upper limit of A_{eff} was explored when given different bandwidth constraints resulting in a 6.82 Relative Core Multiplicity Factor (RCMF). The optimised fibres and their corresponding properties are shown in [10] and [1].

- New cutoff wavelength regressor which considers the unique Trench-assisted (TA) fibre core's loss behaviour was proposed as presented in Section 4.1.2.2. New 6-core and 8-core fibre designs in standard cladding diameter were designed. 6-core fibres' inter-core XT at 1550 nm is ultra-low between -91.16 and -57.41 dB/km. The XT of 8-core fibres is optimised to -58.43 dB/km for the C+L band and -54.98 dB/km for the S+C+L band. This work has been accepted for publication as [2].

- The SNR and capacity of the optimised MCFs were also estimated with ISRS Gaussian Noise (GN) model. A comprehensive analysis and discussion on the relationship between the optimised MCF design and their transmission performance are conducted. The optimal designs and the influence of bandwidth, A_{eff}, XT and the core number on capacity are presented in [1] and [2].

- Regressors of optical properties in MCF are trained with data sets covering the fabrication error. For the first time, the regressors are designed to predict the linear relationship and the residuals separately to achieve accurate regression. They speed up the calculations up to around 10^6 times with high accuracy. The process of training and their performance are presented in Chapter 7.
- The modelling of MCF fabrication error is introduced and added to the optimisation objective. A workflow that includes a new cost function suitable for all the constraints was proposed for the fabrication yield optimisation of MCFs. The yield of heterogeneous MCFs was optimised under various constraint combinations and in most cases, the yield after optimisation is above 90%.

1.3 Chapter Overview

The remainder of this thesis is organised as follows:

- **In Chapter 2**, the theoretical background, the numerical methods of fibre optical properties calculation, and the MCF evaluation metrics calculation are described. It starts with the mode-solve methods, followed by the optical properties calculation methods including both general fibre properties and special properties of MCFs. Then, the MCF evaluation methods are introduced: core multiplicity factor and transmission capacity.
- **In Chapter 3**, the existing MCFs are reviewed from three aspects: the core distributions, core index profile and design methods. In addition, the MCF fabrication methods and the performance evaluation are presented. It offers an overview of the MCF development and current state.
- **Chapter 4** focuses on the AI tool kit I designed for the MCF design. The Machine Learning (ML) toolboxes are designed for predicting optical properties. Then, based on the application requirements, some of them are chosen to be used in the objective function of the optimisation toolbox. The theory of the ML methods used for optical properties regression is presented and the training process and the performance of the regressors and classifiers are demonstrated. Subsequently, the development of the Particle Swarm Optimisation (PSO) algorithm and the hyper-parameters tuning are reviewed. Then, the PSO algorithm and the hyper-parameters used in the MCF designs are introduced.
- **In Chapter 5**, a novel AI-based optimisation method is proposed. A combination of coating loss classifier and regressor is used to accelerate the calculation time while providing 0% false positives. The 6-core TA fibres are optimised for minimising XT or maximising A_{eff}. They are compared to the

other fibres in both XT and RCMF. This chapter also includes the transmission performance of the optimised MCFs investigation and comparison in two transmission-length cases.

- **In Chapter 6**, a cutoff wavelength regressor is introduced that aims to cover the TA core's unique loss behaviour. It is added to the optimisation process. New 6-core and 8-core fibre designs for the C + L and S + C + L bands are investigated with various combinations of constraints. Based on the optimised MCF structures, this chapter also evaluates the impact of optical properties on the MCF capacity, in terms of bandwidth, A_{eff}, XT and core number.

- **In Chapter 7**, the fabrication error of MCF is modelled and added to the optimisation process. The fabrication-yield objective function is designed with new cost functions to encompass all the constraints. The ability of this optimisation method to improve the fabrication yield is assessed by optimising MCFs in several cases.

- **In Chapter 8**, the work demonstrated in this thesis is summarised and suggestions for future work are presented.

1.4 Publications Related to this Thesis

The original contributions made in the course of the research carried out during this PhD are as follows:

Journal papers

- **X. Mu**, A. Ottino, F. M. Ferreira and G. Zervas, "Optimization of 125-μm Heterogeneous Multi-Core Fibre Design Using Artificial Intelligence," in IEEE Journal of Selected Topics in Quantum Electronics, vol. 28, no. 4, pp. 1-13, July-Aug. 2022.

- **X. Mu**, A. Ottino, F. M. Ferreira, and G. Zervas, "Design and transmission analysis of TA multi-core fibre in standard cladding diameter," Opt. Express 30, 38152-38166 (2022)

- **X. Mu**, A. Ottino, and G. Zervas, "Fabrication yield optimisation of heterogeneous multi-core fibres with Machine Learning," to be submitted to Scientific Report after the patent is filed.

Conference papers

- **X. Mu**, F. M. Ferreira, A. Ottino, and G. Zervas, "Design Optimization of Uncoupled Six-core Fibers in Standard Cladding Diameter Using Artificial

Intelligence," in Optical Fiber Communication Conference (OFC) 2021, paper Th1A.34.

- H. Alkharsan, C. W. F. Parsonson, Z. Shabka, **X. Mu**, A. Ottino, and G. Zervas, "Optimal and Low Complexity Control of SOA-Based Optical Switching with Particle Swarm Optimisation," in European Conference on Optical Communication (ECOC) 2022, paper Tu3C.5.

Patent

- **X. Mu**, A. Ottino, F. M. Ferreira, and G. Zervas, "Methods and apparatus for optical fibre design and production, " P122374GB, filed on 28 May 2021, UKIPO.

Chapter 2

Fundamentals of multi-core fibre

In this chapter, the optical properties of the multi-core fibre are described. First, the basic equations for general optical waveguides and circular fibre and the methods we used to find solutions are introduced. Then, the definition and the calculation of each optical property are explained including the general optical properties of the fibre core and two special ones in a multi-core fibre.

An optical waveguide with a proper refractive index profile can confine the light inside and allow the light to propagate along the optical waveguide. Generally, the refractive index is higher at the waveguide centre than around. Optical fibre is an important category of the optical waveguide, which encompasses a round core inside and annular cladding around the core. The behaviour of optical light, as an electromagnetic wave, inside the waveguide can be described with Maxwell's equation.

$$\nabla \cdot (\boldsymbol{\varepsilon}\tilde{\mathbf{E}}) = \rho, \tag{2.1}$$

$$\nabla \cdot \tilde{\mathbf{B}} = 0, \tag{2.2}$$

$$\nabla \times \tilde{\mathbf{E}} = -\frac{\partial \tilde{\mathbf{B}}}{\partial t}, \tag{2.3}$$

$$\nabla \times \tilde{\mathbf{B}} = \mu(J + \boldsymbol{\varepsilon}\frac{\partial \tilde{\mathbf{E}}}{\partial t}), \tag{2.4}$$

where $\tilde{\mathbf{E}}$ and $\tilde{\mathbf{B}}$ are electric field and magnetic flux density. The magnetic field $\tilde{\mathbf{H}} = \tilde{\mathbf{B}}/\mu - \mathbf{M}$, where $\mathbf{M}$ is the magnetization vector. When the material is not magnetic, $\mathbf{M} = 0$ and $\mu = \mu_0$. $\boldsymbol{\varepsilon}$ is the permittivity. Here we consider merely isotropic material. Thus, $\varepsilon = \varepsilon(x, y, z)$. The ε_0 and μ_0 are permittivity and permeability of free space. They have the following relationships with light velocity c and the refractive index n:

$$c^2 = \frac{1}{\varepsilon_0 \mu_0}, \tag{2.5}$$

$$n^2 = \frac{\varepsilon}{\varepsilon_0}. \tag{2.6}$$

ρ is charge density and J is current density. $\nabla\cdot$ is divergence operator while $\nabla\times$ is curl

operator.

Along the fibre, when the light travels away from the light source, Maxwell's equation can be treated as source-free. In other words, ρ and J are zeros.

$$\nabla \cdot (\varepsilon \tilde{\mathbf{E}}) = 0, \tag{2.7}$$

$$\nabla \cdot \tilde{\mathbf{H}} = 0, \tag{2.8}$$

$$\nabla \times \tilde{\mathbf{E}} = -\mu_0 \frac{\partial \tilde{\mathbf{H}}}{\partial t}, \tag{2.9}$$

$$\nabla \times \tilde{\mathbf{H}} = \varepsilon \frac{\partial \tilde{\mathbf{E}}}{\partial t}. \tag{2.10}$$

The assumption of the implicit time dependent $exp(jwt)$ is made for $\tilde{\mathbf{E}}$ and $\tilde{\mathbf{H}}$, where $w = \frac{2\pi c}{\lambda}$ is the angular frequency. Then, the fields can be expressed as:

$$\tilde{\mathbf{E}} = \mathbf{E} exp(jwt), \;\; \mathbf{E} = \hat{\mathbf{r}} E_r + \hat{\boldsymbol{\phi}} E_\phi + \hat{\mathbf{z}} E_z, \tag{2.11}$$

$$\tilde{\mathbf{H}} = \mathbf{H} exp(jwt), \;\; \mathbf{H} = \hat{\mathbf{r}} H_r + \hat{\boldsymbol{\phi}} H_\phi + \hat{\mathbf{z}} H_z, \tag{2.12}$$

Now we ignore the time dependence and focus on the spatial dependence of the fields $\mathbf{E}$ and $\mathbf{H}$.

$$\nabla \times \mathbf{E} = -jw\mu_0 \mathbf{H}, \tag{2.13}$$

$$\nabla \times \mathbf{H} = jw\varepsilon \mathbf{E}. \tag{2.14}$$

Substituting Eq. 2.11 and Eq. 2.12 into the above two equations, the transverse fields E_r and E_ϕ, H_r and H_ϕ can be expressed in the longitudinal fields E_z and H_z. Moreover, for the optical fibre, the longitudinal in-variance can be assumed, for instance,
$E_z = E_t exp(-j\beta z) = R_E(r)\Phi_E(\phi) exp(-j\beta z)$.

$$E_r = \frac{-j}{k^2 n^2 - \beta^2} \big(\frac{\mu w}{r} \frac{\partial H_z}{\partial \phi} + \beta \frac{\partial E_z}{\partial r} \big), \tag{2.15}$$

$$H_r = \frac{-j}{k^2 n^2 - \beta^2} \big(\beta \frac{\partial H_z}{\partial r} - \frac{\varepsilon w}{r} \frac{\partial E_z}{\partial \phi} \big), \tag{2.16}$$

$$E_\phi = \frac{-j}{k^2 n^2 - \beta^2} \big(\frac{\beta}{r} \frac{\partial E_z}{\partial \phi} - \mu w \frac{\partial H_z}{\partial r} \big), \tag{2.17}$$

$$H_\phi = \frac{-j}{k^2 n^2 - \beta^2} \big(\varepsilon w \frac{\partial E_z}{\partial r} + \frac{\beta}{r} \frac{\partial H_z}{\partial \phi} \big), \tag{2.18}$$

where β is the propagation constant.

Thus, when E_z and H_z are known, the others can be obtained subsequently. By applying the curl operator to both sides of Eq. 2.13 and substituting Eq. 2.14, the wave

equation of the electric field can be derived.

$$\nabla^2 E_z + w^2 \mu_0 \varepsilon E_z = \nabla(\nabla \cdot E_z) \tag{2.19}$$

Substituting the equations about the w, n and the wave number $k = \frac{2\pi}{\lambda}$ into the above one, it becomes:

$$\nabla^2 E_z + k^2 n^2 E_z = \nabla(\nabla \cdot E_z) \tag{2.20}$$

When the medium is uniform—ε and n become constant, Eq. 2.7 becomes $\nabla \cdot \tilde{\mathbf{E}} = 0$. This leads to the Helmholtz equation.

$$\nabla^2 E_z + k^2 n^2 E_z = 0 \tag{2.21}$$

In cylindrical coordinates, the above Helmholtz equation can be expressed as [11]:

$$\frac{\partial E_z^2}{\partial r^2} + \frac{1}{r}\frac{\partial E_z}{\partial r} + \frac{1}{r^2}\frac{\partial E_z^2}{\partial \phi^2} + \frac{\partial E_z^2}{\partial z^2} + k^2 n^2 E_z = 0, \tag{2.22}$$

Taking $E_z = E_t exp(-j\beta z) = R_E(r)\Phi_E(\phi)exp(-j\beta z)$ into the above equation

$$\frac{\partial E_t^2}{\partial r^2} + \frac{1}{r}\frac{\partial E_t}{\partial r} + \frac{1}{r^2}\frac{\partial E_t^2}{\partial \phi^2} + (k^2 n^2 - \beta^2)E_t = 0, \tag{2.23}$$

Considering the variables separation, Eq. 2.23 becomes two parts:

$$\frac{\partial R_E(r)^2}{\partial r^2} + \frac{1}{r}\frac{\partial R_E(r)}{\partial r} + (k^2 n^2 - \beta^2)R_E(r) = 0, \tag{2.24}$$

$$\frac{1}{r^2}\frac{\partial \Phi_E(\phi)^2}{\partial \phi_E^2} + (k^2 n^2 - \beta^2)\Phi_E(\phi) = 0. \tag{2.25}$$

For $\Phi_E(\phi)$, according to Eq.2.25,

$$\Phi_E(\phi) \sim exp(l\phi), \tag{2.26}$$

where l is an integer. Thus, $E_z = R_E(r)exp(l\phi)exp(-j\beta z)$

For $R_E(r)$, when $k^2 n^2 - \beta^2 > 0$, the solution would be

$$R_E(r) = A_1 J_m(\xi r) + B_1 N_m(\xi r), \;\; \xi = \sqrt{k^2 n^2 - \beta^2}, \tag{2.27}$$

and when $k^2 n^2 - \beta^2 < 0$, the solution would be

$$R_E(r) = A_2 I_m(\zeta r) + B_2 K_m(\zeta r), \;\; \zeta = \sqrt{\beta^2 - k^2 n^2}, \tag{2.28}$$

where the A_1 and B_1, A_2 and B_2 are coefficients. J_m is the m-th Bessel function and

N_m is the m-th Neumann function. I_m and K_m are the m-th first kind and second kind modified Bessel functions respectively.

The same derivation can be applied on H_z.

$$R_H(r) = C_1 J_m(\xi r) + D_1 N_m(\xi r), \quad \xi = \sqrt{k^2 n^2 - \beta^2}, \tag{2.29}$$

and when $k^2 n^2 - \beta^2 < 0$, the solution would be

$$R_H(r) = C_2 I_m(\zeta r) + D_2 K_m(\zeta r), \quad \zeta = \sqrt{\beta^2 - k^2 n^2}. \tag{2.30}$$

Then all the fields can be expressed if the coefficients are found out. In Section 2.1, the methods to solve wave equations are introduced.

2.1 Fibre mode solution

Before explaining the mode-solving methods, it's important to note that the refractive index of the fibre material changes with the operating wavelength $n = f(\lambda)$. An example is shown in Fig. 2.1. Generally, a three-term Sellmeier equation [12] is

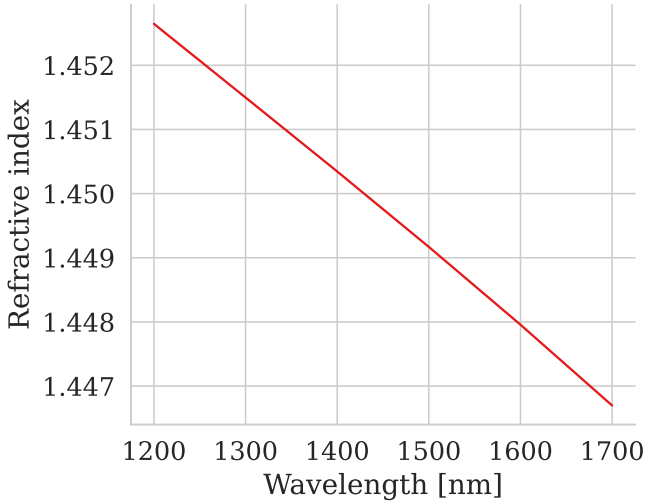

Fig. 2.1: Refractive index of the germanium-silica decreases with wavelength. Its refractive index difference to Silica is 0.3%.

utilised to describe the wavelength dependence of the refractive index.

$$n^2 - 1 = \sum_{i=1}^{3} \frac{a_i \lambda^2}{\lambda^2 - b_i^2}, \tag{2.31}$$

where a_i and b_i are the parameters purely depending on the material.

In a composite system, it is assumed that the Sellmeier parameters are the linear combination of those of the pure material. Therefore, a_i and b_i for binary glass,

germanium-silica (GeO_2-SiO_2) and fluorine-silica (F-SiO_2), are expressed as [13]:

$$a_i(X_{Ge}, X_F) = a_i^0 + X_{Ge} \cdot da_i^{Ge} + X_F \cdot da_i^F, \tag{2.32}$$

$$b_i(X_{Ge}, X_F) = b_i^0 + X_{Ge} \cdot db_i^{Ge} + X_F \cdot db_i^F, \tag{2.33}$$

where the a_i^0 and b_i^0 are the parameters of pure silica. The X_{Ge} and X_F are mole fractions of the GeO_2 and F respectively. The da_i^{Ge}, da_i^F and db_i^{Ge}, db_i^F are the first-order variation terms of the two materials respectively. The parameters obtained by the fitting are shown in [13]. When the X_{Ge} and X_F are known, the material's index can be obtained at each interesting wavelength.

For the fibre refractive index profile, the refractive index difference Δ is used for description.

$$\Delta = \frac{n_{co}^2 - n_{cl}^2}{2n_{co}^2} \tag{2.34}$$

when taking core (n_{co}) and cladding (n_{cl}) as example. At a fixed wavelength when the Δ is known with, for example, pure-silica cladding, the n_{co} can be obtained there. Then, with the foregoing equations and the known parameter, X_{Ge} can be solved. Thus, how n_{co} changes with wavelength can be described with the Sellmeier equation 2.31. When the whole refractive index profile of the fibre is known for all wavelengths, the fibre mode can be solved for further use.

In the past half century [14, 15], people devoted themselves to the development of optical mode solvers. Several groups of modal analysis methods were proposed. In this work, two of them are introduced. One is based on the series expansion [16] and was developed to be a matrix-based method. The other one is the finite difference method which is utilised in the Finite Difference Eigenmode (FDE) solver in Lumerical.

2.1.1 Numerical mode solver

Taking the step-index fibre as an example, β of the guided modes should be between kn_{co} and kn_{cl}. In the core, the $R(r)$ follows Eq. 2.27 while in the cladding it follows Eq. 2.28. Here there are two special cases: where $r = 0$, $R(r)$ cannot be infinite. Therefore, B_1, the coefficient of N_m, is zero because $N_m(0)$ is infinite. And when $r \to \infty$, $R(r) = 0$. Thus, A_2, the coefficient of I_m, is zero because I_m diverges at $r \to \infty$. Then Eq. 2.27 and Eq. 2.28 become:

$$R_E(r) = A_1 J_m(\xi r), \;\; \xi = \sqrt{k^2 n_{co}^2 - \beta^2}, r < a \tag{2.35}$$

in the core and

$$R_E(r) = B_2 K_m(\zeta r), \;\; \zeta = \sqrt{\beta^2 - k^2 n_{cl}^2}, r > a \tag{2.36}$$

in the cladding where a is the core radius.

Similar expressions for H_z are as follows:

$$R_H(r) = C_1 J_m(\xi r), \;\; \xi = \sqrt{k^2 n_{co}^2 - \beta^2}, r < a \tag{2.37}$$

in the core and

$$R_H(r) = D_2 K_m(\zeta r), \;\; \zeta = \sqrt{\beta^2 - k^2 n_{cl}^2}, r > a \tag{2.38}$$

in the cladding where a is the core radius. Fig. 2.2 illustrates the field intensity distribution of the fundamental mode of which $m = 0$.

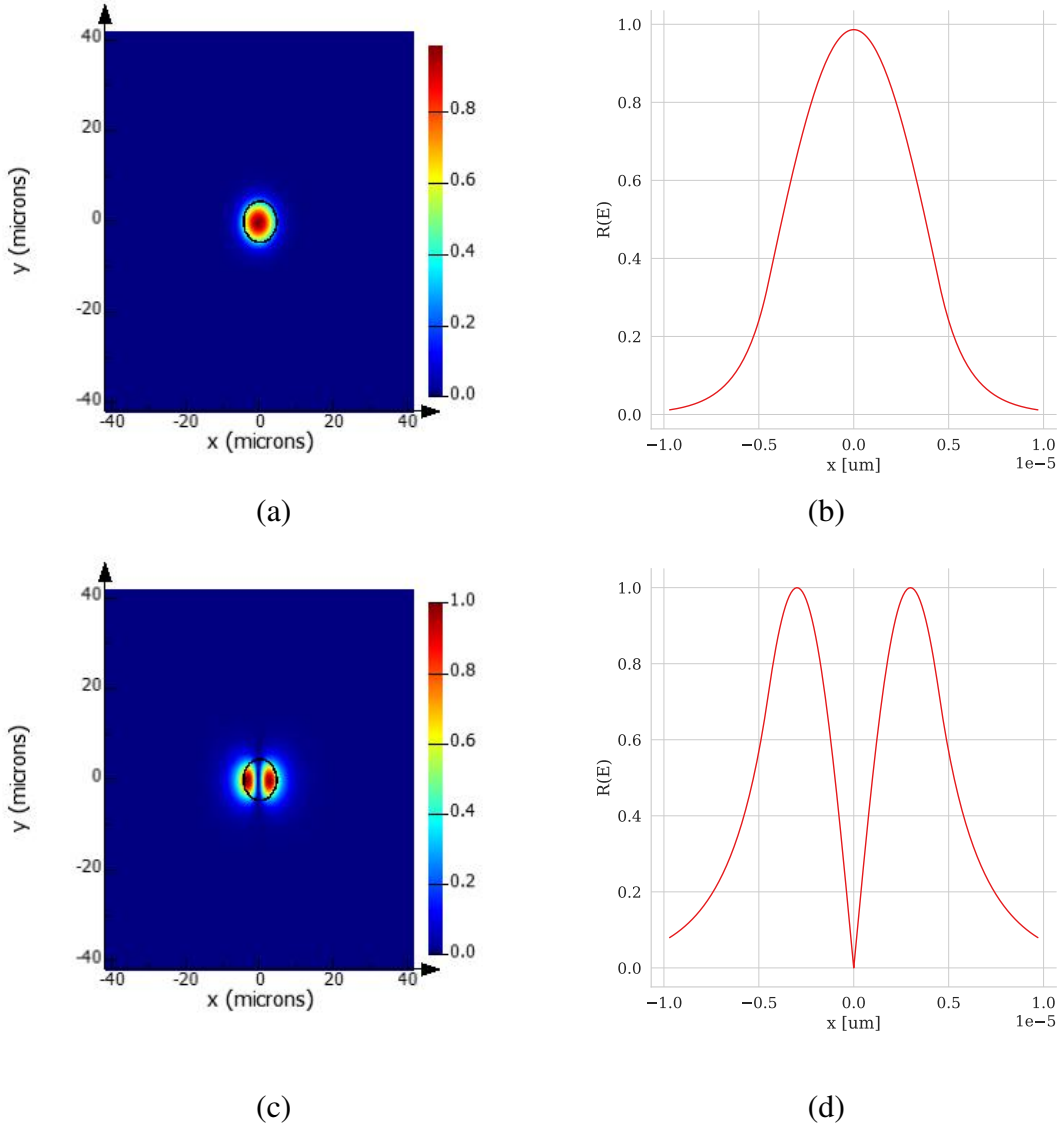

Fig. 2.2: (a) and (b) LP01 mode field distribution (c) and (d) LP11 mode field distribution.

At the interface of core and cladding, $r = a$, the tangential fields—E_z, H_z, E_ϕ,

H_ϕ—need to be continuous, in other words, they should equal to each other when $r = a$. This leads to the following four equations for the four tangential fields respectively.

$$A_1 J_m(\xi a) - B_2 K_m(\zeta a) = 0, \tag{2.39}$$

$$C_1 J_m(\xi a) - D_2 K_m(\zeta a) = 0, \tag{2.40}$$

$$\frac{-j}{\xi^2}\big(\frac{\beta l}{r} A_1 J_m(\xi a) - \mu w \xi C_1 J'_m(\xi a)\big) - \frac{-j}{\zeta^2}\big(\frac{\beta l}{r} B_2 K_m(\zeta a) - \mu w \zeta D_2 K'_m(\zeta a)\big) = 0, \tag{2.41}$$

$$\frac{-j}{\xi^2}\big(\varepsilon_{co} w \xi A_1 J'_m(\xi a) + \frac{\beta}{r} l C_1 J_m(\xi a)\big) - \frac{-j}{\zeta^2}\big(\varepsilon_{cl} w \zeta B_2 K'_m(\zeta a) + \frac{\beta}{r} l D_2 K_m(\zeta a)\big) = 0. \tag{2.42}$$

After collecting the terms, the above equations can be arranged as a matrix.

$$\begin{bmatrix} J_m(\xi a) & -K_m(\zeta a) & 0 & 0 \\ 0 & 0 & J_m(\xi a) & -K_m(\zeta a) \\ \frac{-j\beta l}{a\xi^2} J_m(\xi a) & \frac{j\varepsilon_{co} w}{a\zeta^2} K_m(\zeta a) & \frac{j\mu w}{\xi} J'_m(\xi a) & \frac{-j\mu w}{\zeta} K'_m(\zeta a) \\ \frac{-j\varepsilon_{co} w}{\xi} J'_m(\xi a) & \frac{j\varepsilon_{cl} w}{\zeta} K'_m(\zeta a) & \frac{-j\beta l}{a\xi^2} J_m(\xi a) & \frac{j\beta l}{a\zeta} K_m(\zeta a) \end{bmatrix} \begin{bmatrix} A_1 \\ B_2 \\ C_1 \\ D_2 \end{bmatrix} = M \begin{bmatrix} A_1 \\ B_2 \\ C_1 \\ D_2 \end{bmatrix} = 0$$

When $det(M) = 0$, there is a non-trivial solution for the coefficients. Thus, $det(M) = 0$ becomes the characteristic equation for the step-index profile. Each solution corresponds to a mode propagating inside the fibre.

For circular fibre with a radially in-homogeneous index profile, for example, a graded-index profile, in theory, the cross-section can be subdivided into thin layers. Within each layer, the index is treated as homogeneous and then an easier problem is to be solved. However, the number of equations will become large while the layers number increases. Thus, C. Yeh and G. Lindgren proposed a 4x4 matrix method to overcome the complex computation in [17]. In 2005, Steven R.A.Dods [18] made some improvements to make it more efficient.

Dividing the fibre cross-section into q regions, each region can be expressed by the matrix. For the very first region, the expressions of the tangential fields can be written

as follows:

$$\begin{bmatrix} E_z(1) \\ H_\phi(1) \\ H_z(1) \\ E_\phi(1) \end{bmatrix} = \begin{bmatrix} J_m(\xi_1 r) & 0 & 0 & 0 \\ \frac{-j\varepsilon_1 w}{\xi_1} J'_m(\xi_1 r) & 0 & \frac{-j\beta l}{r\xi_1^2} J_m(\xi_1 r) & 0 \\ 0 & 0 & J_m(\xi_1 r) & 0 \\ \frac{-j\beta l}{r\xi_1^2} J_m(\xi_1 r) & 0 & \frac{j\mu w}{\xi_1} J'_m(\xi_1 r) & 0 \end{bmatrix} \begin{bmatrix} A_1 \\ B_1 \\ C_1 \\ D_1 \end{bmatrix} = M_1 \begin{bmatrix} A_1 \\ 0 \\ C_1 \\ 0 \end{bmatrix}$$

In the q-th region, the fields are

$$\begin{bmatrix} E_z(q) \\ H_\phi(q) \\ H_z(q) \\ E_\phi(q) \end{bmatrix} = M_q \begin{bmatrix} A_q \\ B_q \\ C_q \\ D_q \end{bmatrix}$$

$$= \begin{bmatrix} J_m(\xi_q r) & -K_m(\xi_q r) & 0 & 0 \\ \frac{-j\varepsilon_q w}{\xi_q} J'_m(\xi_q r) & \frac{j\varepsilon_q w}{\xi_q} K'_m(\xi_q r) & \frac{-j\beta l}{r\xi_q^2} J_m(\xi_q r) & \frac{j\beta l}{r\xi_q^2} K_m(\xi_q r) \\ 0 & 0 & J_m(\xi_q r) & -K_m(\xi_q r) \\ \frac{-j\beta l}{r\xi_q^2} J_m(\xi_q r) & \frac{j\beta l}{r\xi_q^2} K_m(\xi_q r) & \frac{j\mu w}{\xi_q} J'_m(\xi_q r) & \frac{-j\mu w}{\xi_q} K'_m(\xi_q r) \end{bmatrix} \begin{bmatrix} A_q \\ B_q \\ C_q \\ D_q \end{bmatrix}$$

$$N_q \begin{bmatrix} E_z(1) \\ H_\phi(1) \\ H_z(1) \\ E_\phi(1) \end{bmatrix} = P_q \begin{bmatrix} A_1 \\ B_1 \\ C_1 \\ D_1 \end{bmatrix},$$

in which,

$$N_q = \begin{bmatrix} 1 & 0 & 0 & 0 \\ 0 & -1 & \frac{j\beta l}{r\xi_q^2} & 0 \\ 0 & 0 & 1 & 0 \\ \frac{j\beta l}{r\xi_q^2} & 0 & 0 & -1 \end{bmatrix}$$

$$P_q = \begin{bmatrix} J_m(\xi_q r) & -K_m(\xi_q r) & 0 & 0 \\ \frac{-j\varepsilon_q w}{\xi_q} J'_m(\xi_q r) & \frac{j\varepsilon_q w}{\xi_q} K'_m(\xi_q r) & 0 & 0 \\ 0 & 0 & J_m(\xi_q r) & -K_m(\xi_q r) \\ 0 & 0 & \frac{-j\mu w}{r\xi_q} J'_m(\xi_q r) & \frac{j\mu w}{r\xi_q} K'_m(\xi_q r) \end{bmatrix}$$

Thus, the coefficients of the $m+1$-th region can be expressed from that of the m-th layer.

$$\begin{bmatrix} A_{q+1} \\ B_{q+1} \\ C_{q+1} \\ D_{q+1} \end{bmatrix} = M_q(r_q) M_{q+1}^{-1}(r_q) \begin{bmatrix} A_q \\ B_q \\ C_q \\ D_q \end{bmatrix} = P_{q+1}^{-1}(r_q) N_{q+1}(r_q) N_q^{-1}(r_q) P_q(r_q) \begin{bmatrix} A_q \\ B_q \\ C_q \\ D_q \end{bmatrix},$$

Compared with M_q, N_q and P_q are easier to the matrix inverse. In the $(q+1)$-th region, the fields are

$$\begin{bmatrix} E_z(q+1) \\ H_\phi(q+1) \\ H_z(q+1) \\ E_\phi(q+1) \end{bmatrix} = M_{q+1} \begin{bmatrix} 0 \\ B_{q+1} \\ 0 \\ D_{q+1} \end{bmatrix}$$

$$= \begin{bmatrix} 0 & -K_m(\xi_{q+1} r) & 0 & 0 \\ 0 & \frac{j\varepsilon_{q+1} w}{\xi_{q+1}} K'_m(\xi_{q+1} r) & 0 & \frac{j\beta l}{r\xi_{q+1}^2} K_m(\xi_{q+1} r) \\ 0 & 0 & 0 & -K_m(\xi_{q+1} r) \\ 0 & \frac{j\varepsilon_{q+1} w}{r\xi_{q+1}^2} K_m(\xi_{q+1} r) & 0 & \frac{-j\mu w}{\xi_{q+1}} K'_m(\xi_{q+1} r) \end{bmatrix} \begin{bmatrix} A_{q+1} \\ B_{q+1} \\ C_{q+1} \\ D_{q+1} \end{bmatrix}$$

From the first region to the $(q+1)$-th region, there is a chain equation:

$$M_1 \begin{bmatrix} A_1 \\ 0 \\ C_1 \\ 0 \end{bmatrix} = M_2 M_2^{-1} M_3 M_3^{-1} ... M_q M_q^{-1} M_{q+1} \begin{bmatrix} 0 \\ B_{q+1} \\ 0 \\ D_{q+1} \end{bmatrix}$$

Rewriting the above equation gives:

$$\begin{bmatrix} J_m(\xi_1 r) & 0 & -M_{11} & -M_{21} \\ \frac{-j\varepsilon_1 w}{\xi_1} J'_m(\xi_1 r) & \frac{-j\beta l}{r\xi_1^2} J_m(\xi_1 r) & -M_{12} & -M_{22} \\ 0 & J_m(\xi_1 r) & -M_{13} & -M_{23} \\ \frac{-j\beta l}{r\xi_1^2} J_m(\xi_1 r) & \frac{j\mu w}{\xi_1} J'_m(\xi_1 r) & -M_{14} & -M_{24} \end{bmatrix} \begin{bmatrix} A_1 \\ C_1 \\ B_{q+1} \\ D_{q+1} \end{bmatrix} = 0,$$

where M_{mn} are the elements of the matrix M.

$$M = M_2 M_2^{-1} M_3 M_3^{-1} ... M_q M_q^{-1} M_{q+1} = P_2 N_2^{-1} P_2^{-1} N_2 N_3^{-1} P_3 .... P_q^{-1} N_q P_{q+1} N_{q+1}^{-1} \tag{2.43}$$

The dispersion equation can be obtained by setting the determinant of M to zero. Then the propagation constants of the modes in the fibre guide can be found by solving the equation.

2.1.2 Finite difference method

Transferring Eq. 2.15∼2.18 into Cartesian coordinate yields :

$$jw\varepsilon E_x = \frac{\partial H_z}{\partial y} - j\beta H_y, \tag{2.44}$$

$$jw\varepsilon E_y = j\beta H_x - \frac{\partial H_z}{\partial x}, \tag{2.45}$$

$$jw\varepsilon E_z = \frac{\partial H_y}{\partial x} - \frac{\partial H_x}{\partial y}, \tag{2.46}$$

$$-jw\mu_0 H_x = \frac{\partial E_z}{\partial y} - j\beta E_y, \tag{2.47}$$

$$-jw\mu_0 H_y = j\beta E_x - \frac{\partial E_z}{\partial x}, \tag{2.48}$$

$$-jw\mu_0 H_z = \frac{\partial E_y}{\partial x} - \frac{\partial E_x}{\partial y}, \tag{2.49}$$

Discretizing the above equations while scaling **E** by free space impedance $Z_0 = \sqrt{\mu_0/\varepsilon_0}$ leads to:

$$jk\varepsilon_x(l,m)E_x(l,m) = \frac{H_z(l,m) - H_z(l,m-1)}{\Delta y} - j\beta H_y(l,m), \tag{2.50}$$

$$jk\varepsilon_y(l,m)E_y(l,m) = j\beta H_x(l,m) - \frac{H_z(l,m) - H_z(l,m-1)}{\Delta x}, \tag{2.51}$$

$$jk\varepsilon_z(l,m)E_z(l,m) = \frac{H_y(l,m) - H_y(l,m-1)}{\Delta x} - \frac{H_x(l,m) - H_x(l,m-1)}{\Delta y}, \tag{2.52}$$

$$-jkH_x(l,m) = \frac{E_z(l,m+1) - E_z(l,m)}{\Delta y} - j\beta E_y(l,m), \tag{2.53}$$

$$-jkH_y(l,m) = j\beta E_x(l,m) - \frac{E_z(l,m+1) - E_z(l,m)}{\Delta x}, \tag{2.54}$$

$$-jkH_z(l,m) = \frac{E_y(l,m+1) - E_y(l,m)}{\Delta x} - \frac{E_x(l,m+1) - E_x(l,m)}{\Delta y}, \tag{2.55}$$

where

$$\varepsilon_x(l,m) = [\varepsilon(l,m) + \varepsilon(l,m-1)]/2, \tag{2.56}$$

$$\varepsilon_y(l,m) = [\varepsilon(l,m) + \varepsilon(l-1,m)]/2, \tag{2.57}$$

$$\varepsilon_z(l,m) = [\varepsilon(l,m) + \varepsilon_(l,m-1) + \varepsilon(l-1,m) + \varepsilon(l-1,m-1)]/4. \tag{2.58}$$

The discretisation scheme [19] can be illustrated as shown in Fig. 2.3

Eq. 2.50∼ 2.55 can be expressed in matrix format.

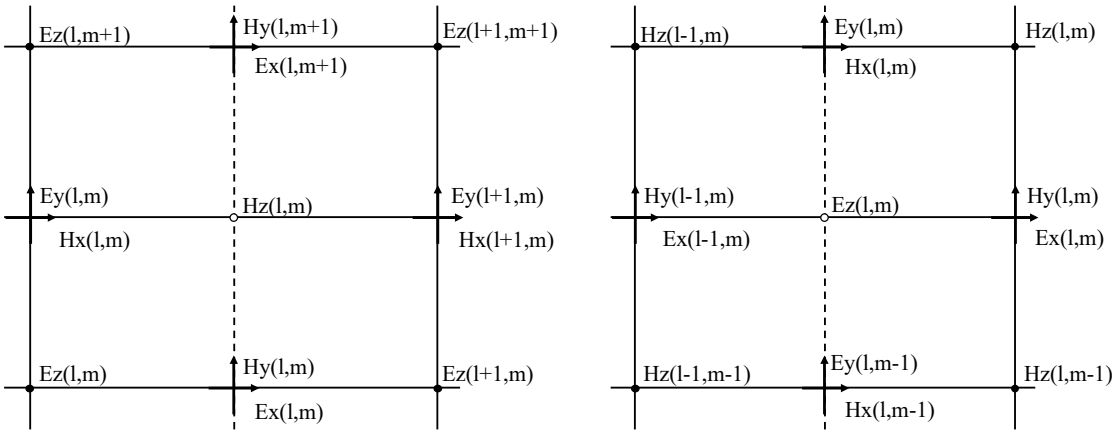

Fig. 2.3: 2D mesh.

$$jk\begin{bmatrix}\varepsilon_x & \mathbf{0} & \mathbf{0}\\ \mathbf{0} & \varepsilon_y & \mathbf{0}\\ \mathbf{0} & \mathbf{0} & \varepsilon_z\end{bmatrix}\begin{bmatrix}\mathbf{E}_x\\ \mathbf{E}_y\\ \mathbf{E}_z\end{bmatrix}=\begin{bmatrix}\mathbf{0} & -j\beta\mathbf{I} & \mathbf{U}_y\\ -j\beta\mathbf{I} & \mathbf{0} & -\mathbf{U}_x\\ -\mathbf{U}_y & \mathbf{U}_x & \mathbf{0}\end{bmatrix}\begin{bmatrix}\mathbf{H}_x\\ \mathbf{H}_y\\ \mathbf{H}_z\end{bmatrix}$$

$$-jk\begin{bmatrix}\mathbf{H}_x\\ \mathbf{H}_y\\ \mathbf{H}_z\end{bmatrix}=\begin{bmatrix}\mathbf{0} & -j\beta\mathbf{I} & \mathbf{V}_y\\ -j\beta\mathbf{I} & \mathbf{0} & -\mathbf{V}_x\\ -\mathbf{V}_y & \mathbf{V}_x & \mathbf{0}\end{bmatrix}\begin{bmatrix}\mathbf{E}_x\\ \mathbf{E}_y\\ \mathbf{E}_z\end{bmatrix}$$

$\mathbf{U}_x$,$\mathbf{U}_y$,$\mathbf{V}_x$,$\mathbf{V}_y$ are square matrix of the discretisation along x or y direction.

By replacing $\mathbf{E}_z$ and $\mathbf{H}_z$ with transverse fields, the equations between transverse fields can be derived [20].

$$\begin{bmatrix}\mathbf{P}_{xx} & \mathbf{P}_{xy}\\ \mathbf{P}_{yx} & \mathbf{P}_{yy}\end{bmatrix}\begin{bmatrix}\mathbf{E}_x\\ \mathbf{E}_y\end{bmatrix}=\beta^2\begin{bmatrix}\mathbf{E}_x\\ \mathbf{E}_y\end{bmatrix}$$

$$\begin{bmatrix}\mathbf{Q}_{xx} & \mathbf{Q}_{xy}\\ \mathbf{Q}_{yx} & \mathbf{Q}_{yy}\end{bmatrix}\begin{bmatrix}\mathbf{H}_x\\ \mathbf{H}_y\end{bmatrix}=\beta^2\begin{bmatrix}\mathbf{H}_x\\ \mathbf{H}_y\end{bmatrix}$$

Solving the above two equations provides the β and the modal fields of each guided mode.

2.2 General fibre core optical properties

From β and the modal fields of each guided mode, the optical properties of the fibre can be calculated and analyzed.

2.2.1 Effective refractive index

Effective refractive index (n_{eff}) can describe the phase delay of light propagation in the waveguide per unit length. n_{eff} can be obtained from β.

$$\beta = \frac{2\pi}{\lambda} n_{\text{eff}}, \tag{2.59}$$

Similar to β, n_{eff} depends on the refractive index profile of the waveguide. Since the refractive index has wavelength dependence, n_{eff} also changes with wavelength. Meanwhile, each mode has its own β and the corresponding n_{eff}. n_{eff} is called modal index as well. Generally, the higher order modes have smaller β and lower n_{eff}.

2.2.2 Effective mode area

Effective mode area (A_{eff}) or Mode Field Diameter (MFD) is utilised to describe the size of the mode fields. MFD is the diameter where the field strength decreases to its $1/e$ and

$$A_{\text{eff}} = \frac{(\int I \, dA)^2}{\int I^2 \, dA}, \tag{2.60}$$

$$= \frac{(\int E^2 \, dA)^2}{\int E^4 \, dA}, \tag{2.61}$$

where I is the optical intensity. The integral is made over the fibre cross-section.

A_{eff} represents the optical intensity distribution which influences the non-linearity effects inside the waveguide. The nonlinear phase shift depends on both the optical power and A_{eff}.

$$\varphi = \frac{2\pi PL}{\lambda A_{\text{eff}}} n_2, \tag{2.62}$$

$$= \gamma PL, \tag{2.63}$$

in which P is the optical power. L is waveguide length. n_2 is the nonlinear index. $\gamma = \frac{2\pi n_2}{\lambda A_{\text{eff}}}$ is the nonlinear coefficient. Therefore, the larger A_{eff}, the smaller the nonlinear effects. This is important, especially for long-haul transmission. The A_{eff} of the standard single-mode fibre is around 80 μm^2. There are fibre designs for large A_{eff} up to 148.3 μm^2 [21]. Meanwhile, for highly nonlinear fibre, the A_{eff} can be 12.4 μm^2.

2.2.3 Chromatic dispersion

As mentioned before, the refractive index changes with wavelengths. The light with different wavelengths propagates with different velocities $v = c/n(\lambda)$. Thus, they

arrive at the destination at different time points, resulting in pulse spreading. This phenomenon is described by chromatic dispersion.

Chromatic Dispersion (CD) includes two parts: material dispersion and waveguide dispersion. Material dispersion comes from the medium itself while waveguide dispersion is a result of the waveguide structure. When n_{eff} at various wavelengths are obtained, chromatic dispersion can be calculated:

$$CD = \frac{2\pi}{\lambda}(2\frac{dn_{\text{eff}}}{dw} + w\frac{d^2 n_{\text{eff}}}{dw^2}) \tag{2.64}$$

2.2.4 Cutoff wavelength

Cutoff wavelength is the longest wavelength where all the modes having higher orders than the mode interested in can propagate inside the waveguide. There are three types of cutoff wavelengths. The theoretical cutoff wavelength is the wavelength at which the n_{eff} equals the cladding index. The other two are fibre cutoff and cable cutoff. They correspond to standardized methods in the International Electrotechnical Commission (IEC) 60793-1-44 document. Taking single-mode operation as an example, the LP11 losses reach 19.34 dB with 2-m long fibre at 140 mm bending radius at fibre cutoff wavelength. As for cable cutoff wavelength, the LP11 modes have a loss of 19.34 dB but with 22-m long fibre on two 40 mm-radius loops. For the TA fibre core, when the

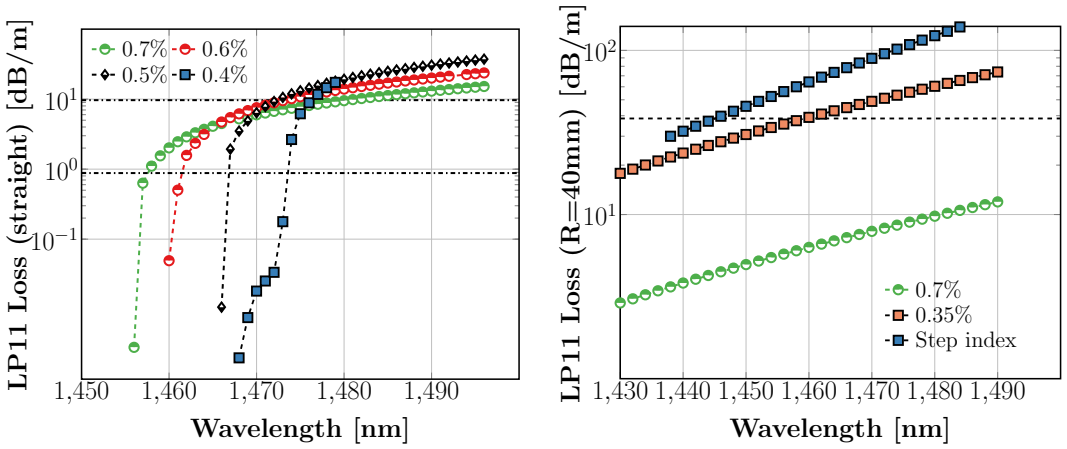

(a) (b)

Fig. 2.4: (a) LP11 loss of TA fibre at straight condition; (b) LP11 loss of TA fibre and SI fibre at a bending radius of 40 mm. The legends are the refractive index difference between the inner cladding and the trench.

trench is shallow, it behaves similarly to the step-index fibre. But as the trench becomes deep, its behaviour of the loss is different. In Fig. 2.4, how the LP11 loss changes with different trench depths under straight and bending conditions is illustrated. Because of the strong light confinement ability, the bending loss of the deep-trench fibre core

increases much more slowly compared to the shallow-trench and step-index fibre. Thus, to get the cutoff wavelength of the deep-trench fibre, the loss of LP11 mode at straight condition is calculated [22] using the Lumerical FDE solver with Perfect Matching Layer (PML) boundary condition in this work.

The deep-trench fibre reaches the fibre cutoff wavelength in the leaky regime in which the loss is large but increases slowly. As for the cable cutoff wavelength, sometimes it lies even in the guiding regime in which the loss is small but increases fast.

2.2.5 Fibre Attenuation

The attenuation of fibre represents the losses during the transmission from input to output. The losses increase with transmission length. Hence, after a certain length, the optical power and the signal-to-noise ratio will be too low for the receiver. This is one of the reasons why the span length is limited. Thus, low attenuation is attractive, especially in the submarine system. Generally, fibres have a low attenuation window in C-band. The attenuation of Single-mode Fibre (SMF) is around 0.2 dB/km at 1550 nm. Some ultra-low loss fibre can reach 0.17 dB/km. Optical fibre attenuation

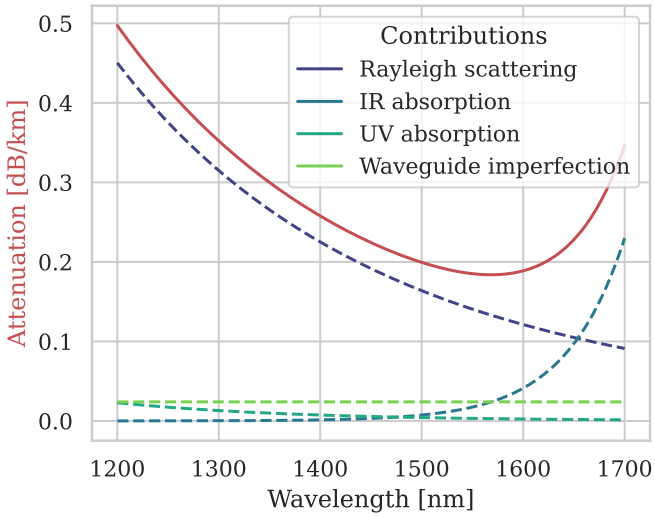

Fig. 2.5: The attenuation and its contributions [23, 24] of TA fibre core depicted in Fig. 2.6. (a_1= 4 μm, $w_{cl} = w_{tr}$= 2.5 μm, $\Delta_1 = 0.3\%$, $\Delta_2 = -0.7\%$.)

has several attributions: Rayleigh scattering, absorption due to the OH^- ion, waveguide imperfection, infrared absorption and ultra-violet absorption. In [23], the attenuation of SMF is modelled. Among them, the Rayleigh scattering is the most weighted. To model the Rayleigh scattering of our silica-based TA fibre core, we take the dopant concentration and optical power distribution into consideration[24] and calculate the Rayleigh scattering coefficient. Since Rayleigh scattering is proportional

to $1/\lambda^4$, we can model it over the whole bandwidth of the fibre core. The absorption due to the OH^- ion is ignored because we assume that the fibre is dry. Waveguide imperfections lead to losses with a constant value shown as the Eq.(3) in [23]. As for the infrared and ultra-violet absorption, the fitting functions Eq.(5) and Eq.(6) in [23] of the Standard Single-mode Fibre (SSMF) are used. One example of TA fibre core is shown in Fig. 2.5.

2.3 Special optical properties in multi-core fibre

In this section, two special properties of multi-core fibre—inter-core crosstalk and the loss due to the coating— are introduced.

2.3.1 Inter-core crosstalk

Light propagating in waveguides is generally referred to as stable mode patterns in the core region, alongside unguided continuous modes. These light waves influence each other when in close proximity. This coupling phenomenon is inevitable in the multi-core fibre because the cores are placed together inside one cladding. The analysis of coupling in multi-core fibre is based on the coupled-mode theory [25, 26].

2.3.1.1 Coupled-mode theory

Compared to the coupled-wave theory [27], the coupled-mode theory focuses on the interaction between the propagation modes. The assumption that the mode will not change significantly by the coupling introduces the perturbation theory.

Taking two parallel waveguides as an example, the eigenmode in each waveguide, E_q and H_q where $q = 1, 2$, satisfies the Maxwell equations as Eq. 2.13 and Eq. 2.14. We express the electromagnetic fields of the coupled waveguide as the sum of the mentioned eigenmodes.

$$\mathbf{E} = A(z)\mathbf{E}_1 + B(z)\mathbf{E}_2, \tag{2.65}$$

$$\mathbf{H} = A(z)\mathbf{H}_1 + B(z)\mathbf{H}_2. \tag{2.66}$$

Substituting the above equation into the equations Eq. 2.13 and Eq. 2.14, the relationship between the eigenmodes in two waveguides can be obtained:

$$(\mathbf{u}_z \times \mathbf{E}_1)\frac{dA}{dz} + (\mathbf{u}_z \times \mathbf{E}_2)\frac{dB}{dz} = 0, \tag{2.67}$$

$$(\mathbf{u}_z \times \mathbf{H}_1)\frac{dA}{dz} - jw\varepsilon_0(n^2 - n_1^2)A\mathbf{E}_1 + (\mathbf{u}_z \times \mathbf{H}_2)\frac{dB}{dz} - jw\varepsilon_0(n^2 - n_2^2)B\mathbf{E}_2 = 0, \tag{2.68}$$

where n is refractive index distribution over the whole region. n_1 and n_2 are the refractive index profiles of the two waveguides respectively.

With the mode orthogonality, the following equations between $A(z)$ and $B(z)$ can be derived [26]:

$$\frac{dA}{dz} + c_{12}\frac{dB}{dz}exp[-j(\beta_2 - \beta_1)z] + j\chi_1 A + j\kappa_{12}Bexp[-j(\beta_2 - \beta_1)z] = 0, \quad (2.69)$$

$$\frac{dB}{dz} + c_{21}\frac{dA}{dz}exp[j(\beta_2 - \beta_1)z] + j\chi_2 B + j\kappa_{21}Aexp[j(\beta_2 - \beta_1)z] = 0, \quad (2.70)$$

in which

$$\kappa_{pq} = \frac{w\varepsilon_0 \iint (n^2 - n_q^2)\mathbf{E}_p^* \cdot \mathbf{E}_q dxdy}{\iint \mathbf{u}_z \cdot (\mathbf{E}_p^* \times \mathbf{H}_p + \mathbf{E}_p \times \mathbf{H}_p^*)dxdy}, \quad (2.71)$$

$$c_{pq} = \frac{\iint \mathbf{u}_z \cdot (\mathbf{E}_p^* \times \mathbf{H}_q + \mathbf{E}_q \times \mathbf{H}_p^*)dxdy}{\iint \mathbf{u}_z \cdot (\mathbf{E}_p^* \times \mathbf{H}_p + \mathbf{E}_p \times \mathbf{H}_p^*)dxdy}, \quad (2.72)$$

$$\chi_p = \frac{w\varepsilon_0 \iint (n^2 - n_p^2)\mathbf{E}_p^* \cdot \mathbf{E}_p dxdy}{\iint \mathbf{u}_z \cdot (\mathbf{E}_p^* \times \mathbf{H}_p + \mathbf{E}_p \times \mathbf{H}_p^*)dxdy}. \quad (2.73)$$

κ_{pq} is the mode coupling coefficient between the two waveguides. Under the assumption of $c_{pq} = \chi_p = 0(p, q = 1, 2)$, the mode coupling between the waveguides along the propagation direction is as follows:

$$\frac{dA}{dz} = -j\kappa_{12}Bexp[-j(\beta_2 - \beta_1)z], \quad (2.74)$$

$$\frac{dB}{dz} = -j\kappa_{21}Aexp[j(\beta_2 - \beta_1)z]., \quad (2.75)$$

2.3.1.2 Coupling coefficient of Heterogeneous trench-assisted Multi-core Fibre

In this part, the coupling coefficient is derived in the case that the coupling happens between two different TA cores. Heterogeneous Trench-assisted Fibre (Hete-TA-MCF) diagram and core index profile are shown in Fig. 2.6. a_1, w_{clad} and w_{tr} denote the core radius, the width of inner cladding and the trench width, respectively. In the following expressions, $a_2 = a_1 + w_{clad}$ and $a_3 = a_1 + w_{clad} + w_{tr}$. n_{core}, n_{cl} and n_{tr} stand for the refractive index of core, cladding and trench, respectively. The cladding is assumed to be SiO_2 in this work. Δ_1 and Δ_2 are the relative refractive index difference between core and cladding, trench and cladding, respectively.

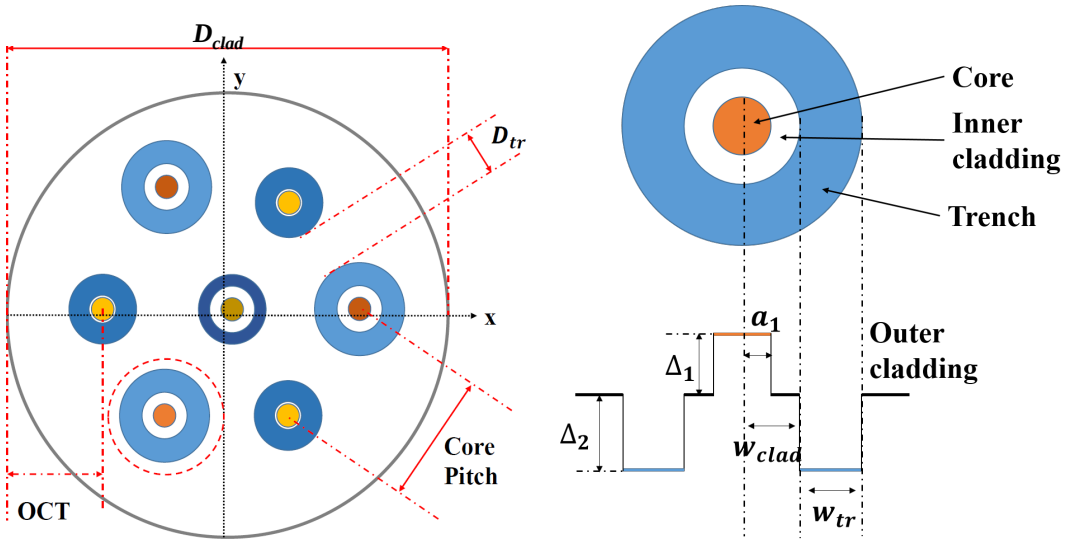

(a) (b)

Fig. 2.6: (a) Hete-TA-MCF layout (D_{clad}: cladding diameter; D_{tr}: the distance between the adjacent trench edges; OCT: outer cladding thickness);
(b) core index profile diagram for Hete-TA-MCF

As discussed in Section 2.1.1, the field of each TA core can be expressed [28]:

$$E_{pz} = \begin{cases} A_p J_n(\xi_p r_p), \quad \xi_p = \sqrt{k^2 n_{co}^2 - \beta^2} & \text{in core of fibre } p \\ B_p K_n(\zeta_p r_p), \quad \zeta_p = \sqrt{\beta^2 - k^2 n_{cl}^2} & \text{in cladding of fibre } p \\ C_p K_n(\zeta_p r_p), \quad \zeta_p = \sqrt{\beta^2 - k^2 n_{tr}^2} & \text{in trench of fibre } p \\ D_p K_n(\zeta_p r_p), \quad \zeta_p = \sqrt{\beta^2 - k^2 n_{cl}^2} & \text{in outer-cladding of fibre } p \\ E_p K_n(\zeta_p r_p), \quad \zeta_p = \sqrt{\beta^2 - k^2 n_{tr}^2} & \text{in trench of fibre } q \\ F_p K_n(\zeta_p r_p), \quad \zeta_p = \sqrt{\beta^2 - k^2 n_{cl}^2} & \text{in cladding of fibre } q \end{cases} \tag{2.76}$$

At each boundary, the field needs to be continuous. To satisfy the boundary condition, the coefficients $B_p \sim F_p$ can be expressed based on A_p. Meanwhile, A_p can be expressed as follows [26]:

$$A_p = \frac{U_{1-p} W_{1-p}}{\beta_p a_{1-p} V_{1-p} J_1(U_{1-p})} \sqrt{\frac{2P}{\pi \varepsilon_0 n_{1-p} c}}, \tag{2.77}$$

where $k = 2\pi/\lambda$ is the wave number and λ is the light wavelength in vacuum. $W_1^2 = a_1^2(\beta^2 - k^2 n_{cl}^2)$ and $U_1^2 = a_1^2(k^2 n_{core}^2 - \beta^2)$ in which β denotes the propagation constant. $V_1 = k a_1 \sqrt{(n_{core}^2 - n_{cl}^2)}$ stands for the normalized frequency.

Substituting the E_z into Eq. 2.71, the mode-coupling coefficient κ_{pq} between two

TA non-identical cores can be analytically expressed as [28].

$$\kappa_{pq} = \frac{k(n_p^2 - n_{cl}^2)W_{1-p}U_{1-p}L_q\sqrt{\frac{\pi a_{1-q}}{2W_{1-p}D}}\exp\left(-W_{1-q}\frac{D}{a_{1-q}}\right)}{\sqrt{n_p n_q}a_{1-p}a_{1-q}V_{1-p}V_{1-q}J_1(U_{1-p})J_1(U_{1-q})} \cdot \int_0^{a_{1-p}} J_0\left(U_{1-p}\frac{r}{a_{1-p}}\right)I_0\left[(\frac{W_{1-p}}{a_{1-p}} - \frac{P_2 - P_1 + Y_2 - Y_1}{D-r})r\right] \cdot \exp\left[(P_2 - P_1 + Y_2 - Y_1)\frac{D}{D-r}\right]rdr, \tag{2.78}$$

where D represents the distance between core pairs. L_q, P_1, P_2, Y_1 and Y_2 can be expressed as:

$$L_q = \frac{J_1(U_{1-q})K_1\left(\frac{W_{1-q}a_{2-q}}{a_{1-q}}\right)K_1\left(\frac{W_{2-q}a_{3-q}}{a_{1-q}}\right)}{K_1(W_{1-q})K_1\left(\frac{W_{2-q}a_{2-q}}{a_{1-q}}\right)K_1\left(\frac{W_{1-q}a_{3-q}}{a_{1-q}}\right)}, \tag{2.79}$$

$$P_1 = W_{1-q}\frac{D - a_{3-p}}{a_{1-q}}, \quad P_2 = W_{2-q}\frac{D - a_{3-p}}{a_{1-q}}, \tag{2.80}$$

$$Y_1 = W_{2-q}\frac{D - a_{2-p}}{a_{1-q}}, \quad Y_2 = W_{1-q}\frac{D - a_{2-p}}{a_{1-q}}, \tag{2.81}$$

$$P_1 - Y_1 + P_2 - Y_2 = (W_{1-q} - W_{2-q})\frac{D - W_{tr-p}}{a_{1-q}}, \tag{2.82}$$

where $V_2 = ka_1\sqrt{(n_{cl}^2 - n_{tr}^2)}$ and $W_2^2 = V_2^2 + W_1^2$. And $K_1(x)$ is the 2^{nd} kind modified Bessel function with first order.

This κ_{pq} can also be utilized in the homogeneous case and for the step-index profile. For Homogeneous Trench-assisted Fibre (Homo-TA-MCF), since the cores are all the same, the equation can be adjusted by removing core ID (p and q). The obtained κ are identical for all the core pairs. And to transfer the equation for the step-index profile, $a_1 = a_2 = a_3$ and $n_{tr} = n_{cl}$ need to be substituted into the mode-coupling equation.

2.3.1.3 Coupled-power Theory

Eq. 2.74 and Eq. 2.75 show that the mode coupling is dependent on the propagation distance. In coupled-mode theory, it is assumed that $\kappa_{pq} = K_{pq}f(z)$ in which K_{pq} is a constant while $f(z)$ is supposed to be a stationary random variable with Gaussian correlation function. Instead of the amplitude, the power change caused by the influence of other waveguides is explored [29]:

$$\frac{dP_p}{dz} = \sum h_{pq}[P_p - P_q], \tag{2.83}$$

where h_{pq} is the power-coupling coefficient. For a homogeneous MCF with a small bending radius, the Power Coupling Coefficient (PCC) [30] is between two identical

cores since $\Delta\beta = \beta_p - \beta_q \approx 0$.

$$h = \frac{2\kappa^2 R_b}{\beta\Lambda} \tag{2.84}$$

where R_b is the bending radius and Λ is the core pitch which is the distance between the two core centres.

For a Hete-MCF, effective refractive index difference Δn_{eff} between the cores leads to the propagation constant difference $\Delta\beta$. The influence of $\Delta\beta$ on the power coupling between a core pair (e.g. core p and core q) varies with R_b. Thus, considering an MCF that has a constant bending radius and is twisted continuously at a constant rate γ [31],

$$h_{pq} = K_{pq}^2 S(\Delta\beta'), \tag{2.85}$$

in which $\Delta\beta' = \Delta\beta + \frac{B_{pq}cos(\gamma z + \theta_{pq})}{R_b}$ with

$$B_{pq} = \sqrt{(\beta_p x_p - \beta_q x_q)^2 + (\beta_p y_p - \beta_q y_q)^2}, \tag{2.86}$$

$$\theta_{pq} = tan^{-1}\frac{\beta_p y_p - \beta_q y_q}{\beta_p x_p - \beta_q x_q}. \tag{2.87}$$

$S(\Delta\beta')$ is the Fourier transform of the auto-correlation function of $f(z)$. Herein it is assumed to be an exponential auto-correlation function.

$$h_{pq} = \frac{2K_{pq}^2 d}{1 + (\Delta\beta'_{pq} d)^2}, \tag{2.88}$$

where $K_{pq} = (\kappa_{pq} + \kappa_{qp})/2$ is the discrete mode-coupling coefficient between the two cores and d is the correlation length of the exponential auto-correlation function. The average power-coupling coefficient $\overline{h}_{pq}$ [31] over a twist pitch can be expressed as:

$$\overline{h}_{pq} = \frac{\gamma}{2\pi}\int_0^{2\pi/\gamma} h_{pq} dz \tag{2.89}$$

$$= \sqrt{2}K_{pq}^2 d\left[\frac{1}{\sqrt{a(b+\sqrt{ac})}} + \frac{1}{\sqrt{c(b+\sqrt{ac})}}\right] \tag{2.90}$$

with

$$a = 1 + \left(\Delta\beta_{pq} d - \frac{B_{pq} d}{R_b}\right)^2, \tag{2.91}$$

$$b = 1 + (\Delta\beta_{pq} d)^2 - \left(\frac{B_{pq} d}{R_b}\right)^2, \tag{2.92}$$

$$c = 1 + \left(\Delta\beta_{pq} d + \frac{B_{pq} d}{R_b}\right)^2, \tag{2.93}$$

$$B_{pq} = \sqrt{(\beta_p x_p - \beta_q x_q)^2 + (\beta_p y_p - \beta_q y_q)^2}, \tag{2.94}$$

d is set as 50 mm because it provides the simulation results that agree well with the experiments in [31, 32]. When the bending radius exceeds the critical bending radius R_{pk}, the inter-core XT decreases and becomes independent of the bending radius.

2.3.1.4 Intercore Crosstalk Formulation for Heterogeneous Trench-assisted Multicore Fiber

inter-core XT in MCF is the power leakage from the adjacent cores to the target core, which can be affected by the mode-coupling coefficient [30]. Core-to-core XT can be calculated as:

$$XT = hL \tag{2.95}$$

where L is fibre length. According to the coupled-power theory [32], the mean inter-core XT of one Homo-MCF core from neighbouring cores can be expressed as [3]:

$$inter - coreXT = \frac{n - ne^{-(n+1)hL}}{1 + ne^{-(n+1)hL}}. \tag{2.96}$$

In this equation, the numerator is the sum of the power in a certain core originating from the other cores while the denominator is the power in a certain core. And n denotes the adjacent core number of the target core.

When assuming that every core in Hete-MCF has a unique index profile, the power-coupling coefficient between each pair of cores is different from the other. Eq. (2.96) is developed to suit this variation as following:

$$inter - coreXT_p = \frac{n - \sum_{i=1}^{n} e^{-(n+1)h_{pq}L}}{1 + \sum_{i=1}^{n} e^{-(n+1)h_{pq}L}}, \tag{2.97}$$

in which, h_{pq} is the average power-coupling coefficient between the cores p and q, where core p is the target core and q can be the core ID of any of its n neighboring cores. In this work, overall inter-core XT indicates the average over the mean inter-core XT of each core, which is considered to be the indicator in fibre optimization.

2.3.2 Coating loss

As illustrated in Fig. 2.6, the cores in MCF in much closer to the edge of the cladding compared to the standard fibre. In the standard fibre, the core centre is 62.5 μm far away from the fibre coat. In MCF, the Outer Cladding Thickness (OCT) is from 22 μm [33] to 40 μm [34]. Thus, the cores in MCF are influenced by the coat of which the refractive index, 1.465$\sim$1.485 [30], is higher than the core. This effect is first noticed in 2010 [35] when the attenuation is measured for different cladding diameters. It is found that the

attenuation is degraded when the cladding diameter is small, in other words, the core is close to the coat. With further exploration [36, 37, 38, 34], the excess loss [36] which is the attenuation difference between the outer core and the centre core is proposed to estimate how much the cores are influenced. The other metrics [30] is the coupling loss to the coating for $R_b = 140$ mm and $\lambda = 1625$ nm. For long-haul transmission, the requirement of coating loss is less than 0.001 dB/km. The coating loss does not change

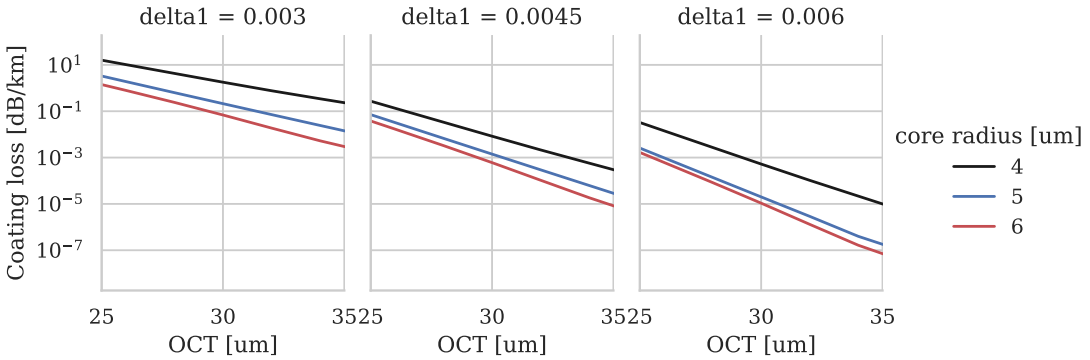

Fig. 2.7: Coating loss changes with fibre index profile. Here is the TA core with $w_{cl} = w_{tr}$= 4 μm and $\Delta_2 = -0.5\%$.

much with the coating index [30] and follows an approximately exponential decrease with an increasing OCT. However, the coating loss depends on not only the OCT but also the refractive index profile of the fibre core itself. Some examples of coating loss are shown in Fig. 2.7. The coating loss is higher in fibre with a smaller core radius and smaller Δ_1. In this work, a classifier and a regressor of the coating loss are developed to check and estimate it during the optimisation in which the refractive index of the fibre core is changing.

2.4 Multi-core fibre performance metrics

Many parameters and properties are important in MCF, such as core number, cladding diameter and A_{eff}. None of them can represent MCF performance alone. There are several ways of evaluating the performance of MCF which include multiple facets of MCF. In this section, two methods are explained. One is based on the fibre optical property while the other is focused on the transmission performance.

2.4.1 Core multiplicity factor

The A_{eff} is used in the Core Multiplicity Factor (CMF) [34, 39].

$$CMF = \frac{N \sum_{m=1}^{lp} A_{\text{eff}}}{(\pi/4) D_c^2}, \tag{2.98}$$

where N is the core number, lp is the mode number and D_c is the cladding diameter of the fibre. Here it is assumed that each fibre core has the same number of modes.

MCF is always compared to the SSMF and therefore the RCMF is defined as:

$$RCMF = \frac{CMF_{\text{mcf}}}{CMF_{\text{ssmf}}}. \tag{2.99}$$

RCMF can roughly show how many times the MCF is better than standard SMF with more spatial channels.

2.4.2 Capacity estimation

The other closely watched metric is the capacity of MCF since one of the most important anticipations on MCF is the solution to the capacity crunch. In long-haul transmission systems, some phenomena degrade the signal: ASE noise, NLI due to the Kerr effect and ISRS. The quality of the signal is always evaluated by the SNR which is the ratio of the signal to the noise.

$$SNR = \frac{P_s}{N^{1+\epsilon}\eta P_s + NP_{ASE} + P_{TRX}}, \tag{2.100}$$

in which P_s is the signal power. The three denominators are NLI, ASE and transceiver noise respectively. N is the number of spans. ϵ and η are the coherent factors and the NLI coefficient.

In MCF, one more phenomenon—XT—needs to be taken into the SNR calculation. Under the assumption that the channels have uniform launch power, SNR in the presence of XT is approximated by [40]:

$$SNR_{XT} = (SNR^{-1} + XT)^{-1}, \tag{2.101}$$

where XT refers to the crosstalk with neighbouring cores.

The capacity of an MCF is calculated as

$$Capacity = \sum_{j}^{N_c} \sum_{i}^{N} B_{ch} \cdot log_2(1 + SNR_{XT}^{i}), \tag{2.102}$$

in which N_c is the number of cores in the MCF, B_{ch} is the bandwidth of each channel and N is the total number of wavelength channels in each core.

2.4.2.1 Closed-form Gaussian noise model with inter-channel stimulated Raman scattering

In transmission, the signals' statistical distribution appears to be Gaussian due to the large values of accumulated dispersion as proved in [41] and [42] in both simulation and experiment. The follow-up papers [43, 44] tested its high accuracy in different system scenarios. This becomes one of the key assumptions of the GN model derived in [45, 46, 47, 48, 49]. The other is the assumption of high cardinality of the signal [50]. Both are satisfied in most cases in modern fibre communication systems. The conventional model GN has also been validated for the ultra-wideband system [51]. In recent years, another nonlinear process—the ISRS was introduced into the GN model [52, 53]. Furthermore, the GN model in the presence of ISRS is developed to be closed-form [54] and to cover ultra wideband [55]. In this work, to model the MCF capacity, the close-form GN model in the presence of ISRS [55] for an ultra-wideband system is utilised. Therefore, the fundamentals of it are presented as follows.

- **Inter-channel Stimulated Raman scattering**

  Stimulated Raman scattering is a nonlinear process that is used in the design of Raman amplifiers and Raman lasers. However, the optical fibre transmission system limits the performance since it transfers energy from high frequency to low frequency, resulting in a continuous frequency shift. The influence becomes obvious when the transmission reaches the ultra-wideband regime.

  Raman gain coefficient g_R [56] is utilised to describe the influence numerically. It depends on the relative change in frequency to the pump frequency, as illustrated in Fig. 2.8. In most relative research, the Raman gain coefficient is approximated by a triangle with a gain slope C_r. For the Raman gain curve in Fig. 2.8, $C_r = 0.028\ \frac{1}{W \cdot km \cdot THz}$. The impact of ISRS will be taken into account in the following ISRS-present GN model discussion.

- **Amplified spontaneous emission noise**

  The ASE noise is generated with the amplification. It is well-modelled by the additive white Gaussian noise. The noise power can be calculated as:

$$P_{ASE} = 2hn_{sp}(f + f_c)B_{ref}(G - 1), \tag{2.103}$$

  where h is Planck's factor and the n_{sp} is the spontaneous emission factor. f is the relative frequency and f_c is the reference frequency. B_{ref} is the reference bandwidth and G is the gain of the amplifier. When $G \gg 1$, the noise figure F_n that is typically used to measure the noise characteristic of an amplifier can

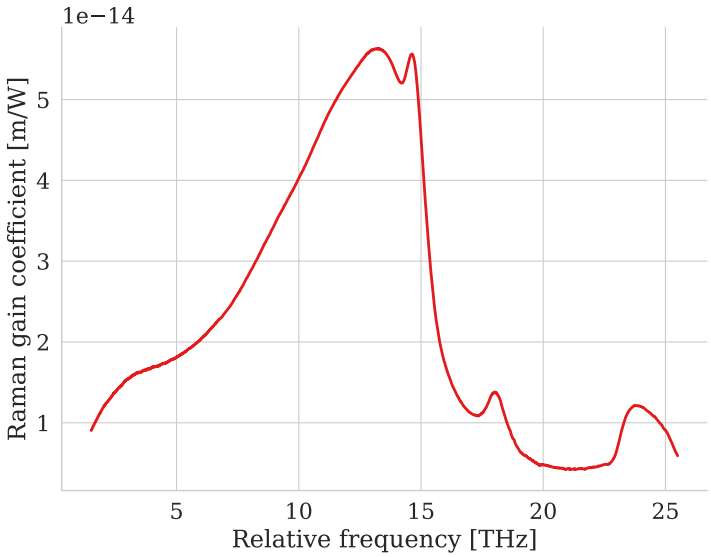

Fig. 2.8: Raman gain coefficient [55] at 1550 nm for a standard single-mode fibre.

approximate $2n_{sp}$.

When considering the impact of ISRS, Gain Flattening Filter (GFF) can be used to compensate for wavelength-dependent fibre loss and the power transfer induced by ISRS. The GFF loss, l_{GFF} attenuate the ASE contribution yielding:

$$P_{ASE}(f_i) = 2hn_{sp}f_iB_{ref}[G(f_i) - 1]l_{GFF}(f_i), \tag{2.104}$$

$$\approx 2hn_{sp}f_iB_{ref}\frac{P_i(0)}{P_i(L)}, \tag{2.105}$$

where P is the power profile. For the wideband transmission, the delayed nonlinear fibre response needs to be taken into account when calculating the power profile by solving the Raman gain equations [57] along the transmission.

$$\frac{\partial P_i}{\partial z} = -\sum_{j=i+1}^{M}\frac{f_j}{2f_i}g_R(\Delta f)P_jP_i + \sum_{j=1}^{i-1}\frac{1}{2}g_R(\Delta f)P_jP_i - \alpha P_i, \tag{2.106}$$

in which the first item is the ISRS loss and the second is the ISRS gain while the last item is the fibre attenuation α. P_i represents the optical power of channel i. The factor $\frac{1}{2}$ comes from the polarisation averaging and $\frac{f_j}{f_i}$ conserves the number of photons. $\Delta f = f_j - f_i$ is the relative frequency shift between channels.

For ultra-wideband $> 15\ THz$, after obtaining the actual power profile by numerically solving Eq. 2.106, it is matched to the first-order power profile [55].

$$P_i^{(i)}(z) = (1 + \tilde{T}_i)e^{-\alpha_i z} - \tilde{T}_i e^{-(\alpha_i + \bar{\alpha_i})z}, \tag{2.107}$$

where $\tilde{T}_i = -\frac{P_{tot}C_{r,i}}{\bar{\alpha_i}}f_i$. P_{tot} is the total optical power.

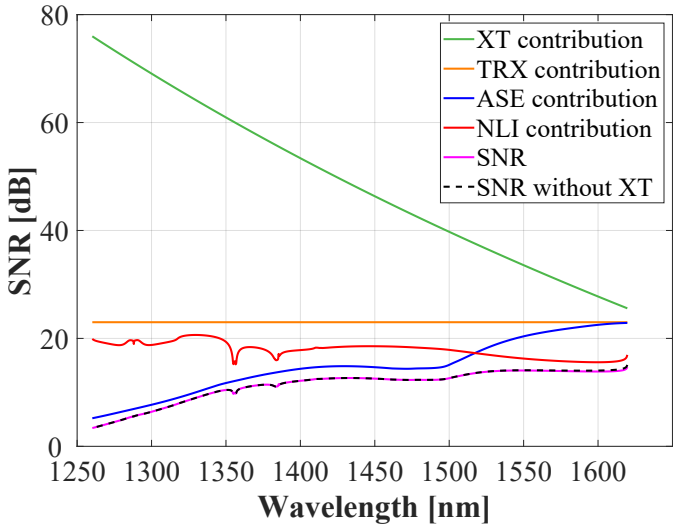

Fig. 2.9: An example of SNR and its contributions in a full-band fibre core after 1200 km transmission.

- **Nonlinear interference noise**

  In the WDM system, the interactions of each channel with itself or with other channels will limit the increase in capacity. As shown in Eq. 2.100, η, the NLI coefficient, represents the noise level brought by the NLI.

  In the GN model, η is obtained by integrating the NLI power spectral density (PSD) $G(f)$ with the channel bandwidth.

$$\eta = \frac{1}{P^3} \int_{-\frac{B_{ch}}{2}}^{\frac{B_{ch}}{2}} \left|H(f)^2\right| G(f) df, \tag{2.108}$$

  When the NLI strongly depends on the frequency of the channel, the GN model is approximated to only consider Self-phase Modulation (SPM) and Cross-phase Modulation (XPM). Both of them are due to the intensity dependence of the refractive index in fibre. SPM is the effect that the refractive index change influences the channel under test while XPM is that this change influences the neighbouring channels.

$$\eta(f_i) \approx \eta_{SPM}(f_i) + \sum_{j=1, j\neq i}^{N_{ch}} \eta_{XPM}^{(j)}(f_i). \tag{2.109}$$

  In the closed-form ISRS GN model, the SPM contribution and the XPM contribution are proposed as follows [54]:

$$\eta_{SPM} \approx \frac{4}{9} \frac{\gamma^2}{B_i^2} \frac{\pi}{\phi_i \bar{\alpha}(2\alpha + \bar{\alpha})} \left[\frac{T_i - \alpha^2}{\alpha} asinh\left(\frac{\phi_i B_i^2}{\pi\alpha}\right) + \frac{A^2 - T_i}{A} asinh\left(\frac{\phi_i B_i}{A}\right) \right], \tag{2.110}$$

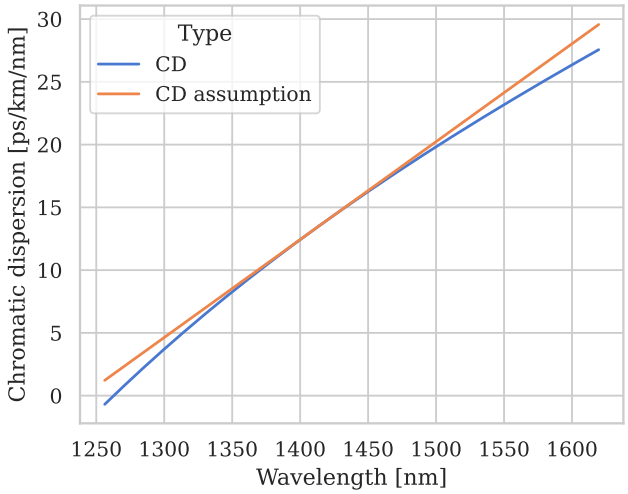

Fig. 2.10: Assumption of chromatic dispersion in transmission performance evaluation.

$$\eta_{XPM}(f_i) \approx \frac{32}{27} \sum_{j=1, j\neq i}^{N_{ch}} \left(\frac{P_j}{P_i}\right)^2 \frac{\gamma^2}{B_j \phi_{i,j} \bar{\alpha}(2\alpha + \bar{\alpha})} \cdot \left[\frac{T_j - \alpha^2}{\alpha} atan\left(\frac{\phi_{i,j} B_i}{\alpha}\right) + \frac{A^2 - T_j}{A} atan\left(\frac{\phi_{i,j} B_i}{A}\right)\right], \tag{2.111}$$

in which $\phi_i = \frac{3}{2}\pi^2(\beta_2 + 2\pi\beta_3 f_i), A = \alpha + \bar{\alpha}$. $T_i = (A - P_{tot} C_r f_i)^2$ and $\phi_{i,j} = 2\pi^2(f_j - f_i)[\beta_2 + \pi\beta_3(f_i + f_j)]$. β_2 is the group velocity dispersion parameter: $\beta_2 = -D\lambda^2/2\pi c$ and β_3 is its linear slope. Here, the chromatic dispersion D and the dispersion slope S are assumed based on the values at the centre frequency. B_i is the bandwidth of channel i.

The impact of ISRS is included in both ASE noise and NLI noise. By considering the parameters of the fibre as wavelength-dependent, the SNR of each core of the fibre can be obtained with the ISRS GN model. An example is shown in Fig. 2.9. For this example, the CD is approximated as a linear function of the CD at 1415 nm and its slope there, as illustrated in Fig. 2.10.

The Tranceiver Noise (TRX) is considered as 23 dB over the whole band. The ISRS affects the power profile leading to a relatively low energy at short wavelengths and a relatively high energy at long wavelengths, which is obvious in the contribution of ASE. The degraded ASE performance dominates the SNR at short wavelengths resulting in low SNR there. Meanwhile, at long wavelengths, NLI is strong because of higher optical power.

Chapter 3

Literature review of multi-core fibre design and fabrication

In 1977, for the very first time, signals were sent through a fibre field test system, which represents the beginning of the era of optical fibre telecommunication. The first decade of history is about the span-by-span opto-electrically regenerated optical fibre transmission system with slow capacity increase. In the early 1990s, the emergence of the Erbium-doped Fibre Amplifier (EDFA) and the corresponding non-linearity management techniques together improved the capacity and eliminated the opto-electrical-opto regeneration. Afterwards, coherent detection further pushed the development of the optical fibre system. Its high receiver sensitivity provides the fibre with the ability to transport more information. However, the capacity of the fibre system is approaching the non-linear Shannon limit. Meanwhile, the standard single-mode fibre is limited by the power threshold brought by the fibre fuse effect. Solutions to the capacity crunch are proposed mainly from two aspects: wider bandwidth and more space channels. To increase the spatial channels, SDM has been actively researched. Several branches of SDM are developed: fibre bundle generally with thin-coating/cladding fibre, multi-core fibre, Multi-mode fibre or the combination of these two.

In 1979, S. Inao et al. proposed MCF for the very first time [58]. After 15 years, single-mode MCF fibre was designed and fabricated to be utilised in fibre-to-the-home (FTTH) network [59]. Until 2008, Extremely Advanced Transmission (EXAT) [60] was proposed for the next generation of optical infrastructure: Multi-level modulation, Multi-core fibre and Multi-mode control. In the following years, Multi-core fibre, Multi-mode fibre and Multi-core Multi-mode fibre sprung up.

Multi-mode fibre is relatively easier to fabricate and align with standard single-mode fibre because of its large core radius. But, Multi-mode fibre design is supposed to minimise inter-mode XT, Mode Dispersion (MD) and Mode Dependent Loss (MDL) [61]. As a result of these degradations, Multi-mode control and receiver always require complex digital signal processing.

The fibre bundle can be claimed as a special multi-core fibre. The spatial density of the fibre bundle is increased by reducing the coating and/or cladding diameter of each fibre inside. In [62], 200 μm cladding fibre was proposed to be used in Wrapping

Tube Cable, which reduces the cable's outer diameter by 16%. Furthermore, Matsuo Shoichiro et al. [63] designed fibre with 80 μm cladding diameter and 160 μm coating diameter that leads to 26% reduction in cable diameter. Although the reduced-clad fibres can realize spatial density increase, the increment is limited and much smaller than that brought by Multi-mode and/or Multi-core.

Among Multi-core fibre, there are two main categories based on the coupling level: weakly-coupled and strongly-coupled. In strongly-coupled MCF, the XT is not negligible, and it can be further divided into systematically-coupled fibre and randomly-coupled fibre. Both of them need Multi-input Multi-output (MIMO) Digital Signal Processing (DSP). Systematically-coupled fibres generally have multiple supermodes which are the combination of the eigenmode of each core. They can be treated as part of mode-distribution multiplexing. Supermodes are orthogonal and weakly coupled. On the other hand, the mode coupling in randomly-coupled fibres [64] is strong and random. However, the MD and MDL in randomly-coupled fibre are close to square-root proportional to the transmission distance, which can suppress the DSP complexity. In weakly-coupled MCF [65], each spatial channel can work independently with negligible XT. Meanwhile, the related technologies, such as connectors between weakly-coupled MCFs are more mature. Hence, they are most promising to be used instead of the standard SMF in existing systems.

In the past decades, a variety of MCFs designs and demonstrations have been proposed and reported. In order to minimise the XT, maximise the spatial efficiency and maximise the spatial channel number, various index profiles, core arrangements and core numbers are introduced. One of the ways is to increase the core number while decreasing the XT or maintaining the XT to an acceptable level. The core number is increased from 7 [30, 35, 66, 67, 68] up to 1000 [69]. While the spatial density increases, the XT and the cladding diameter increase fast. Meanwhile, the fabrication becomes more difficult. In the cross-section of some large core number fibre, it can be seen that the cores are not uniform, the shape is not maintained properly and some cracks exist. Therefore, in 2013, researchers began to pave the way to maintain the diameter of the cladding as standard while reducing the XT with a smaller core number [70, 71] and a heterogeneous structure [72].

3.1 Multi-core fibre design

In this section, the existing designs of MCF core distribution and core index profile are summarised and compared. Then, the methods used to design the MCFs are reviewed and discussed.

3.1.1 Fibre core distributions

Core pitch (Λ) is an important parameter in MCFs. In strongly-coupled fibres, the cores are very close to each other to create the supermodes. As for randomly-coupled fibres, Λ is larger for weakly-coupled fibres but with no strict criteria.

In weakly-coupled fibre, it is vital because the XT is highly dependent on Λ. A slight difference in Λ will lead to a large inter-core XT performance variation. As for multi-mode fibre, it will influence the inter-mode coupling and result in different MD/MDL. Furthermore, Λ is related to the OCT as illustrated in Fig. 2.6. Wider Λ is beneficial for low XT but leads to smaller OCT which puts more pressure on the excess loss of the outermost core, as mentioned in section 2.4.2. Thus, it needs a trade-off between Λ and OCT. Moreover, with a limited cladding diameter, it is important to make efficient use of the space and therefore improve spatial efficiency.

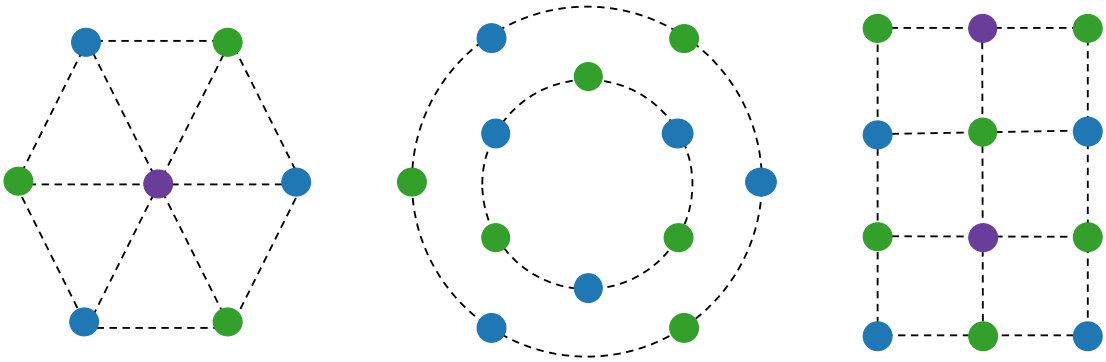

Fig. 3.1: Common core arrangements: hexagonal lattice [left], ring structure [centre], rectangular lattice [right].

Many kinds of core distribution are proposed [73, 74]. The schematic diagram is illustrated in Fig. 3.1. The most common one is the hexagonal lattice. It is like a honeycomb with one core at each vertex. All the cores hold the same distance from the neighbouring cores and all the outer cores have the same distance to the coating. Hexagonal structure has good scalability. When adding more layers, the number of cores increases from 7-core [30, 67, 68, 75, 76], 19-core [77, 78, 79], to 37-core [80, 81, 82]. In [81], one outermost core is replaced with a marker. The spatial channel number increases with both the core number and mode number in each core. The main limitation of further increase is the cladding diameter because the larger cladding rod has lower mechanical reliability [83].

One drawback of this core arrangement is that the cores have different XTs. Thus, on the receiver side, signals through different cores will have different performances. For example, in 7-core fibres, the centre core has double neighbouring cores compared to the outer cores. Thus, generally, the centre core suffers more XT. In other words, the centre core would have worse transmission performance if the MCF is homogeneous.

Moreover, in 7-core hexagonal fibres [30, 68], two important issues are found and influenced the following fibre core allocation design. These two issues also affect other core arrangements. First, in [30], the excess loss of the outermost cores is addressed as attenuation degradation. Its relationship to the coating index and the OCT is simulated. The coating index change does not influence the excess loss significantly but the OCT does. The order of excess loss almost increases linearly with decreasing OCT. Picking 0.001 dB/km as the threshold of excess loss, this fibre design chose 30 μm as the OCT. Among the following papers, the majority directly chooses 30 μm to be the OCT. Even though in most cases the fabricated fibres do not have the excess loss trouble, the design process is not reliable. Because the excess loss depends on both OCT and the outer-layer fibre core index profile. On the other hand, as for [68], this paper noticed the phenomenon of cutoff elongation of the central core. When the Λ decreases, which means that the outer cores get closer to the centre core, the cutoff wavelength of the centre core moves to the longer wavelength side while that of the outer core remains the same. Thus, other papers use different design strategies to compensate for or overcome this trouble: to remove the central core or to use a core with a shorter cutoff wavelength to be the centre core [80].

If the centre core is in a hexagonal 7-core fibre, it results in the ring structure. The cores are usually located uniformly on each ring in the ring structure. When there is only one ring [28, 33, 84], there is only one Λ. Each core has two neighbouring cores and thus every core has the same XT performance. In [85], the cores are located on a hexagonal ring. The outer layer in a 19-core hexagonal structure is kept to form a 12-core fibre so that each core has fewer neighbours, which removes excessive XT. From this structure, it is developed to be a two-ring 12-core fibre [86] so that it can offer larger Λ and lower XT.

Some of them keep the centre core and let the outer layers as a ring structure, which results in two core pitches. In the 10-core fibre [83], because the core pitch between the centre core to the outer cores is much larger than that between the outer cores, the XT of the centre core is 30 dB lower than the XT between outer cores. The 19-core fibre [87] rotated the outer ring for a 15-degree offset to increase the core pitch between the cores on the outer ring and inner ring. Moreover, they carefully designed the inner ring radius to compensate for the neighbouring core difference between the inner-ring cores and the centre core and make them have the same XT. In [88], the Λ is larger than [87] and thus the central core only has a slightly longer cutoff wavelength.

The other core lattice is rectangular or square for high spatial density. 8-core [89, 90] fibres allocate core in two arrays for short-reach applications. [91] changed the 12-core allocation to square lattice because compared to the one-ring structure, it has a higher upper limit of Λ. 16 cores are set as 4x4 matrix for bidirectional signal assignment [92]. In [93], two types of cores are used to create heterogeneous 32-core fibre. It relaxed

the cutoff wavelength condition from 22 m to 1 km for covering C-band. The cutoff wavelengths of the cores surrounded by others are longer than those in the outer layer. [94] has the same core allocation but with different core index profiles. In this lattice, the cores distribute generally with a uniform core pitch to the nearest neighbours. In the high core number case, it can realize the heterogeneous MCF with two types of cores. Other core arrangements need at least three. This can help reduce the complexity of fabrication. However, the outer-layer cores have different OCTs and different distances to the fibre centre. Therefore, when considering the excess loss, the worst-case OCT needs to be checked. On the other hand, it is also found that the fan-out XT from the far-off core is still a limiting factor [92].

3.1.2 Fibre core index profiles

The index profile includes the material and geometric information of the fibre core. The index profile will determine the optical properties of each fibre core and also the interaction between cores or between the core and outer environment. Several index profile diagrams are shown in Fig. 3.2.

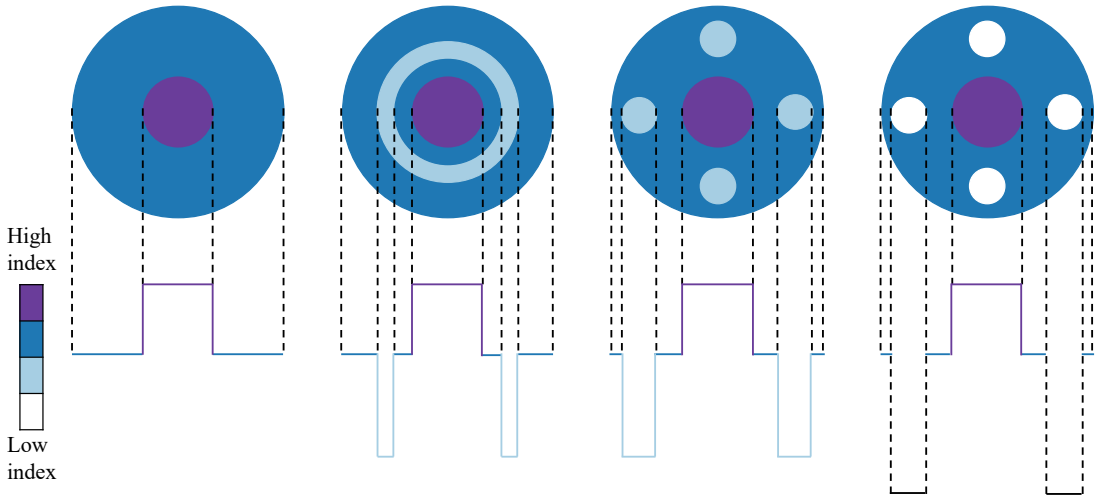

Fig. 3.2: Common core index profile [from left to right]: step-index core, TA core, rod-assisted core, hole-assisted core.

Step index is a common index profile that is widely used in all types of fibre. Meanwhile, the technology of step-index fibre fabrication has come of age. Hence, at the beginning of MCF development, the most utilised index profile is step-index [35, 36, 67]. Step-index MCF is relatively easy to design and fabricate because there are fewer parameters to optimise compared to others. However, with the increasing spatial density, the light confinement ability of the step-index is not sufficient for meeting the XT requirement. Thus, more index profiles have been proposed.

In 2010, [95] proposed the hole-assisted structure and found that the holes help to reduce the XT while keeping the A_{eff} and cutoff wavelength. But at this moment, the problem of excess loss and cutoff elongation is not yet noticed. The holes are not only allocated around the cores but also put as walls [96] in 6-core fibre to reduce the XT. However, the scalability of the hole-wall structure is not good. Afterwards, several hole-assisted fibres are designed and fabricated for both single-mode [70, 97] and few-mode operation [76]. In [70], a 6-core hole-assisted fibre in standard cladding diameter is proposed. While keeping excess loss smaller than 0.01 dB/km, the XT is suppressed to be lower than -30 dB/100km and the core multiplicity factor is around 6.0. The impact of the hole on MCF [98] is investigated and it is clarified that the XT suppression brought by XT increases with the hole diameter. One hole between two cores results in around 20 dB XT reduction.

Then, the TA index profile [30, 68] was proposed in 7-core fibres in 2011. Both of them obtained low XT smaller than -50 dB/km and proved the strong light confinement ability of TA structures. Besides, the paper [30] uses a pure-silica core for the purpose of reducing the attenuation loss and 0.18 dB/km at 1550 nm is obtained. Then TA profile has become a popular choice. Some devoted to making benefit of the strong light confinement brought by a trench for increasing spatial density and/or mode number [77, 81, 82, 84, 85, 88, 89, 99]. The fibre core number is up to 37 [82] and the spatial channel is up to 108 [81]. Some focus more on the band at which the TA MCFs are used. The exploration of using TA fibre core of 8-core fibre in standard cladding diameter [33] is also conducted for the application in the O band. The wide-band utilisation also attracted attention [75]. However, in this paper, the excess loss is not considered. The W-type fibre [71] is similar to the TA profile. The 4-core W-type fibre in standard cladding diameter has ultra-low XT and is suitable for long-haul transmission.

In [94], the low-index rod is adopted instead of the hole and trench to suppress XT while shortening the cutoff wavelength. However, they found that as the outer-layer core, the rod-assisted core can not confine light as expected. Therefore, the TA core replaced them at the outer layer. The rod-assisted index profile can relatively reduce the XT but is not as efficient as hole-assisted and TA profiles.

In multi-mode MCF, the graded-index profile also is used for reducing the Differential mode dispersion (DMD). [91] reduces the absolute DMD to less than 100 ps/km over C + L bands for lower requirement of DSP. GI profile in [78] was adopted to tighten the mode spread and then to reduce DMD, resulting in RCMF $\sim$30. In recent years, the index profile has become more complex. For example, two more layers of trench [100] are added to ensure a smooth transition between highly doped layers.

These index profiles are utilised alone or mixed together [72, 80, 94, 101]. In the latter case, the MCF can benefit from the heterogeneous structure or prevent the cutoff

wavelength elongation of the central core. If the cores of the MCF have identical index profiles, the MCF is homogeneous. Otherwise, it is a heterogeneous MCF. These two terms are proposed in 2009 [73, 102]. Homogeneous fibres are easier to fabricate and implement without the need for alignment to a certain core. As for the heterogeneous fibres, the main benefit is the low XT. Between the non-identical cores, there is the effective refractive index difference (Δn_{eff}) which leads the neighbouring cores into the non-phase matching regime. Without phase-matching points, the XT between fibre cores reduces. In section. 2.3.1, Eq. 2.89 shows how the power coupling coefficient changes with $\Delta\beta_{pq}$ and R_b. When the R_b surpasses the critical bending radius (R_{pk}), the XT decreases sharply to a low level.

$$R_{pk} = \frac{B_{pq}}{\Delta\beta_{pq}} \tag{3.1}$$

With the large $\Delta\beta_{pq}$, the R_{pk} is smaller so that it is easier to render MCF in the non-phase-matching regime in practical use. As for the homogeneous MCF, the $\Delta\beta_{pq}$ equals zero and the PCC increases with the R_b linearly as illustrated in Fig. 3.3.

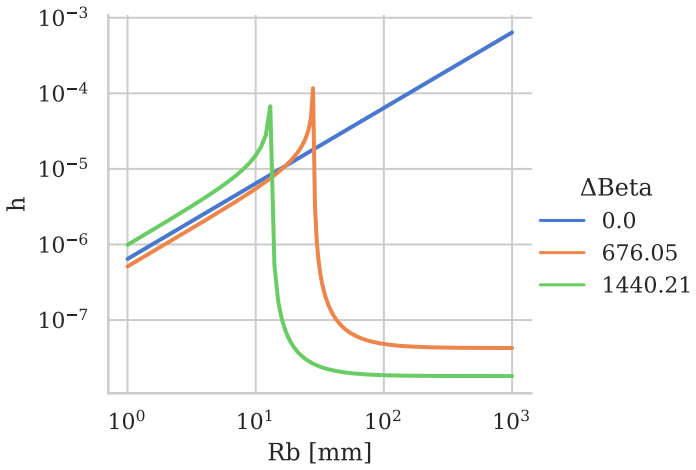

Fig. 3.3: The power coupling coefficient changes with bending radius under different Δn_{eff}.

The dependence of the XT on the bending radius can also be described with the equivalent index model [103, 30].

$$n_{\text{eq}} \approx n\left(1 + \frac{rcos\theta}{R_b}\right), \ \frac{rcos\theta}{R_b} << 1 \tag{3.2}$$

(r, θ) is the local polar coordinates of the fibre cores in the MCF cross-section. When the R_b increases, the difference between the n_{eq} and n becomes large. To compare the index difference within the fibre, the fibre centre is picked as the coordinate centre. Thus, the equivalent effective index of each core can be expressed as:

$$n^{p}_{\text{eq,eff}} \approx n^{p}_{\text{eff}}\left(1 + \frac{D_p cos\theta_p}{R_b}\right) \tag{3.3}$$

and the corresponding R_{pk} is

$$R_{pk} = \frac{n^{p}_{\text{eq,eff}}}{\Delta n^{pq}_{\text{eq,eff}}} D_p \tag{3.4}$$

where D_p is the distance of the fibre core to the fibre centre.

The above two theories showed how the XT depends on the $\Delta n^{pq}_{\text{eff}}$ and the R_b. The heterogeneous MCF attracted vast interest in the past years along with the homogeneous ones. In 2010 and 2011, the hot points were still homogeneous MCFs, but the TA index profile started to gain ground. With the development of fabrication technology, heterogeneous structures, more cores and complex index profiles became the mainstream of the research. However, in recent years, more attention has been paid to the research of the MCF in standard cladding diameter because the crunch of the MCF development comes to the cost and the implementation. MCF in standard cladding diameter is easier to fabricate and utilise which can help MCF become more prevalent in a practical situation.

3.1.3 Fibre design methods

In the foregoing sections, the various index profiles and lattices are introduced. When designing the MCF, these two factors are considered for satisfying the application requirements on mechanical and optical properties. The trade-off among the OCT, core pitch, core allocation and core profiles needs to be conducted. In many papers, MCF manufacturers directly propose fibre structures and then fabricate and characterise the MCF without an explanation of the design process. In those papers which report the design process, there are a few common points. Thus, in this section, the common ways of considering the design trade-off are described and discussed.

The existing MCFs' cladding diameter is from 125 μm up to 320 μm [104]. Mechanical reliability is the main limiting factor. When the cladding diameter becomes large, the fibre has a higher failure probability. In 2011, the upper limit of cladding diameter was 225 μm [83]. It increased to 350 μm [104] in 2019. In standard cladding diameter fibre, since the cladding diameter is fixed, the core arrangement is usually chosen first and then the majority of core index profile parameters are picked. The trade-off between the OCT and core pitch is conducted by checking the XT requirement and excess loss threshold via changing some of the profile parameters. When the cladding diameter becomes variable to some extent, generally the core index profile is designed first. Then, the relationship between the inter-core XT and the core pitch and pick the core pitch first. The relationship between the excess loss and the OCT is investigated and the OCT with which the excess loss satisfies the requirement

is chosen. Finally, the cladding diameter is obtained with these two fixed parameters.

As for the OCT, in [30, 34], the relationship between the excess loss and the OCT is explored. For the same fibre core structure, its excess loss decreases exponentially with the increasing OCT. In [30], the design of the fibre core allows 30 μm OCT while 40 μm OCT in [34], for coating loss smaller than 0.001 dB/km. Another is to fix the OCT first. Most of the fibre designs fix the OCT as 30 μm for reducing the coating loss. Subsequently, the relationship between the core arrangement and the core pitch is investigated and one of the core arrangements is chosen for the following core profile design.

With the same cladding diameter and OCT, different lattices result in various core pitches [74] which follows Square lattice>Hexagonal lattice>Ring lattice. The core-to-core XT decreases rapidly with the core pitch. However, as mentioned in section 3.1.1, the neighbouring core number is different for core lattices while different lattices have their own merits. Thus, the XT needs to be checked in MCF designs for various applications.

The other part of the MCF design is the core index profile since the corresponding optical properties such as A_{eff}, chromatic dispersion and XT need to match the application requirements. The general method is to fix most of the parameters and to check the interesting properties' relationship between 2 parameters or among 3 parameters, then pick one fibre structure from the region where the properties satisfy the demands. In [70], to design a hole-assisted fibre the core radius, core index and hole pitch are fixed. The XT and leakage loss are first checked to see how they change with the ratio between the hole diameter d and the hole pitch Λ at three core pitch choices. After picking one of the core pitches, A_{eff} and the XT are calculated depending on Λ and $\frac{d}{\Lambda}$. To meet the design target—XT less than -30 dB/100km, leakage loss less than 0.01 dB/km and relatively higher A_{eff}, one combination of Λ and $\frac{d}{\Lambda}$ is chosen to be the final design. In this fibre design, 3 of the 5 parameters are roughly considered in three properties changes. The cutoff wavelength is maintained below 1.46 μm. As for TA core fibres [71, 75, 82, 94], the commonly checked parameters are the core pitch, the core index and the core radius while for RA core fibre [84, 94], the general checked parameters include the rod diameter and rod pitch.

It is easier to design homogeneous fibre since only one index profile needs to be designed. It becomes difficult when designing heterogeneous MCFs. Not only the optical properties of two or more types of cores are required to be checked, but the difference among the cores also needs to be calculated. Thus, a few heterogeneous MCF design methods [105, 106] are proposed. The Δn_{eff} is generally used to be the criterion of the heterogeneous level. In some fibre designs, it is transferred to be the difference of cutoff wavelength [82]. In [105], the hexagonal 7-core fibres are designed. The outer cores are selected at first and then the centre core is picked based on both

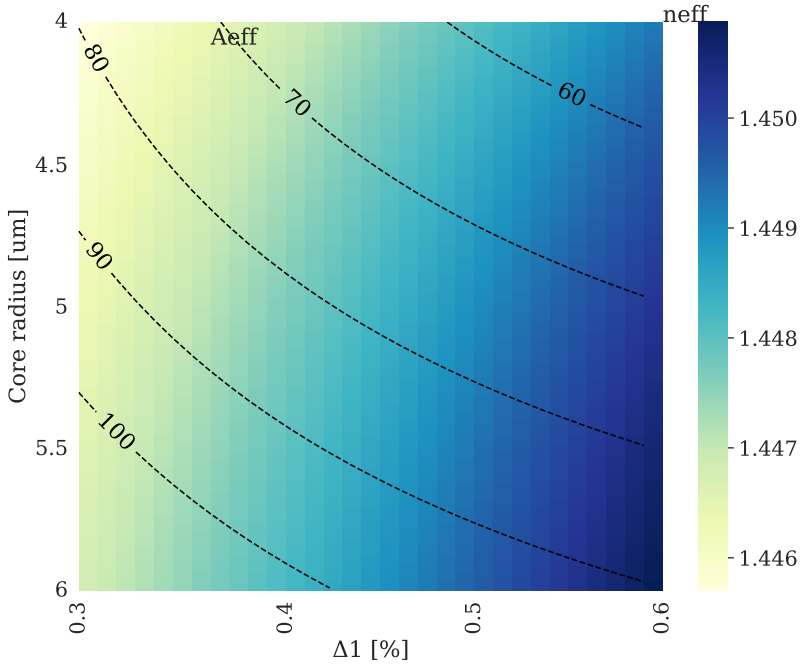

Fig. 3.4: Effective refractive index (n_{eff} and effective mode area (A_{eff}) distribution with core radius and Δ_1 of TA fibre core. Other index profile parameters are $w_{\text{cl}} = 5\mu\text{m}; w_{\text{tr}} = 5\mu\text{m}; \Delta_2 = -0.5\%$.

the optical properties and the XT between the centre core and one of the outer cores. Generally, the centre core has the largest possible Δn_{eff} to the outer cores. In 2021, the core selection method is proposed [106] for ring-structure fibre with two types of fibre cores. It added the core pitch selection for non-identical cores which lets non-identical cores have different OCTs.

3.2 Multi-core fibre fabrication and applications

After designing various MCFs, the next step is to fabricate and evaluate them. The fabrication methods are described and the comparison between the fabricated fibre and the original design is conducted. Then, the MCF evaluation and deployment are reviewed.

3.2.1 Multi-core fibre fabrication

As for both SMF and MCF, the fabrication includes the preform fabrication and fuse and drawing. However, the preform preparation of MCF is different from that of the SMF because the multiple cores may have various index profiles in heterogeneous MCF and the position of the cores need to be fixed in the preform before the fuse and draw.

There are two common methods of MCF preform fabrication. One is the drilling

method. The glass rod of the whole cladding is prepared first. Then it is drilled at the position where the fibre cores are designed to be. The glass rod of each core is inserted into the drilled hole and welded to the cladding. Since the preform needs to be drilled, the length of the preform is limited in this method. The other one is the stack-and-draw method [107]. The rods of the cores are bundled together first according to the core arrangement. The cladding part is prepared as a glass capillary and then the bundled cores are inserted into it. The previous method has relatively higher accuracy and flexibility on the core position. Meanwhile, it can use a larger cladding rod. The latter one is suitable for uniform core arrangements, especially hexagonal distribution.

Recently, some new methods were proposed. The silica sand can be inserted around the cores as cladding [108]. This method improves the flexibility of core allocation. The cladding preform and core rods in [109] are also fabricated separately and then sinter together but the cladding preform is made by the slurry casting method which provides high reproducibility and lowers environmental requirements. To introduce air hole [110], the over-cladding-bundled rods (OBR) method is proposed. The core rods are bundled with spacers which are made of cladding material and used to allocate the cores. Subsequently, the outside vapour deposition method [111] is utilised to add cladding and then make the preform. Theoretically, this method can offer control of the core and hole by changing the space size and position. According to the fabricated SM- and FM- fibres, the layer widths deviate from the design. The deviation is up to 89% in the few mode-MCF. In 2020, the modified cylinder method [112] is reported because of its potential to enlarge preform. Using a modified cross-shape cylinder, the void ratio and the number of rods required are reduced but precise control of hole shape is needed.

People have devoted themselves to the development of MCF fabrication methods. In the past decade, many MCFs have been fabricated and evaluated. In some papers, fabrication error is reported. A homogeneous 4-core fibre [71] is fabricated in standard cladding diameter. The core pitch is designed to be 45 μm but the fabrication result is 44.7$\pm$0.2 μm, which drifts up to 0.5 μm from the design. Meanwhile, the layer width shifts according to a 0.1 change in the depressing layer ratio. The deviation of the core pitch is reported to be $\pm$0.3 μm in [33]. Using the new method proposed in [110], fibres with 4 TA cores with 4 holes are fabricated. The trench width and the cladding width vary up to 65% for the SM-MCF and 89% for the FM-MCF from the designs.

Comparing the fabricated MCFs to the corresponding designs, it is found that the performance of the fabricated MCFs deviates from the design. The 7-core fibre in [30] has a good agreement between the design and fabrication. The cores have circularity according to the cross-section. The 7 cores are designed to be identical but in the fabrication, the fibre is not homogeneous. The fabrication error leads to the core structure deviating from the design. As a result, the MFD deviates from the design up to 0.14 μm and the cutoff wavelength is designed to be 1496 nm but the longest cutoff

wavelength of the fabricated core is 1550 nm. In the fabricated hole-assisted MCF, the sizes of holes are not identical as seen in the cross-section figure. The corresponding optical properties also diverge. For example, in [70], the deviation of A_{eff} is 9.7 μm^2 while that of cutoff wavelength is 30 nm from the mean value. In heterogeneous fibre, a 30-core fibre with four types of core is fabricated with the stack-and-draw method. The A_{eff} of the four types of cores are all designed to be around 80 μm^2 but the fabricated fibre only has an average A_{eff} of 77.3 μm^2. When fibres are fabricated with the same design, the difference between the two fabrications is also represented. 32-core heterogeneous fibres [93] are fabricated twice with the same design. However, the trench width in Fibre A is wider than in Fibre B. Fibre B has around 1 μm^2 smaller A_{eff} and a shorter cutoff wavelength.

Even though the fabrication methods of MCF are improving, the fabrication error is still ineluctable for both homogeneous fibre cores and for mass production of one fibre design. The fabrication error leads to the deviation of the optical performance from the expectation. In characterisation, this will increase the failure ratio and require more fabrication tests, which is time and cost consumption. In mass production, this will result in the fabrication yield drop.

3.2.2 Multi-core fibre performance evaluation

In section 2.4, two performance metrics are mentioned for MCF: core multiplicity factor and capacity. Here the performance of the existing MCFs is described and discussed.

As mentioned, RCMF takes the spatial channel number, cladding diameter and A_{eff} of MCF into account. Thus, people have worked on these three aspects for improving the RCMF while reducing XT: putting more cores into one fibre and/or increasing the mode number in each core, reducing the cladding diameter, and increasing the A_{eff} of cores. Among the 7-core single-mode fibres, large A_{eff}, 110 μm^2 is used to improve the RCMF to 7.28 [34] which is higher than the core number. However, large A_{eff} relates to high XT and high excess loss. Thus, in the following MCF designs, the research interest in large A_{eff} reduces. The core number has been increased to 37 for single-mode MCF and to 38 for few-mode MCF. Among the single-mode MCFs, the highest RCMF is 9.45 [82]. Even though there are 37 cores in one fibre, the large cladding diameter limits the RCMF. In the few-mode case, the RCMF increases up to 75.17 in a 5-LP 13-core fibre [100] although most few-mode MCFs reported are just designed but not fabricated.

The other metric which is concerned about MCF is the capacity it can provide and the transmission length it can support. Single-mode single-core fibre reaches the upper limit around 100 Tbit/s [113]. MCFs have a much higher capacity with the help of multiple spatial channels. However, the capacity performance is limited by the fibre

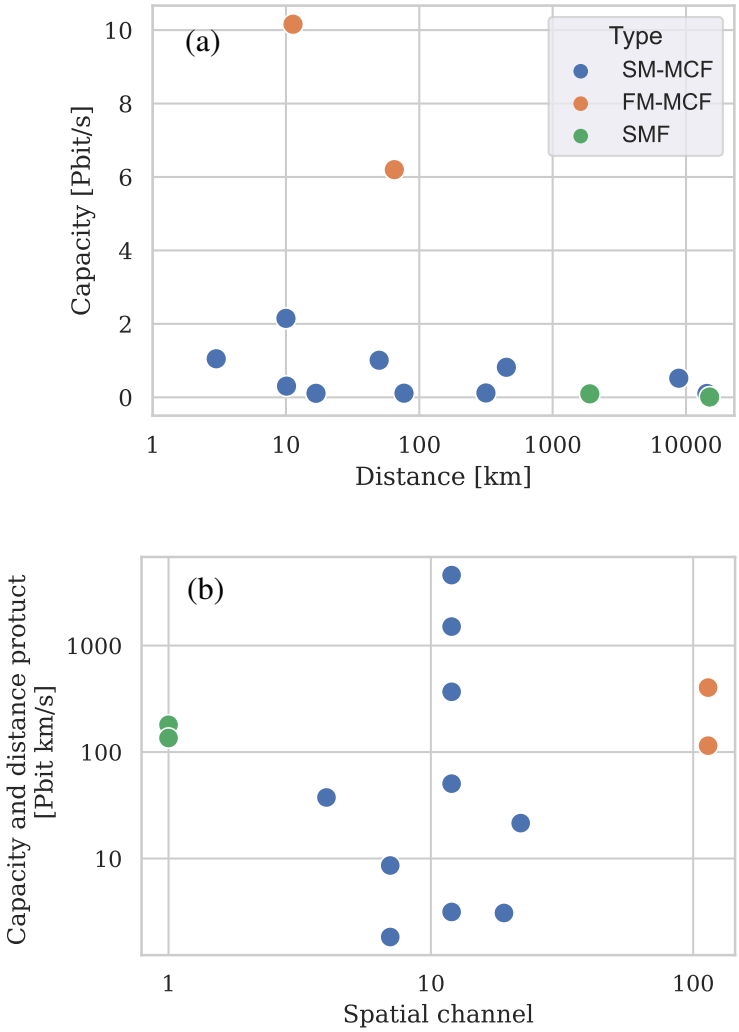

Fig. 3.5: Capacity performance of different fibres.
(a) Capacity vs distance; (b) Capacity and distance product vs spatial channel.

loss, XT between cores or modes and the complexity of MIMO DSP. From 2012 to 2015, transmission experiments were conducted mainly with single-mode MCF. The capacity of MCF increases with the core number from 109 Tbit/s [114] with 7-core fibre up to 2.15 Pbit/s [88] with 22-core fibre. In 2017, a single-mode MCF in standard cladding diameter successfully provided a world record capacity of 118.5 Tbit/s which exceeds the capacity crunch of SSMF [115]. Moreover, it is worth noting that this capacity is reached with a full MCF link which includes multiple spans of three kinds of 4-core fibres, multi-core EDFA and MCF connectors. As for few-mode MCFs, 6.2 Pbit/s over 65km and 10.16 Pbit/s over 11.3 km are both achieved with 114 spatial channels: 38-core 3-mode [116] and 19-core 6-mode [117] respectively. One of the reasons that they both achieved such large capacities is the use of the C+L band.

MCFs have a much higher capacity for short distances or hundreds of km of transmission. Considering the long-haul transmission, the capacity and distance

product of an ultra-low-loss fibre is 135.45 Pbit·km/s with 9 Tbit/s over 15050 km. SMF s have higher or similar capacity and distance products compared to the MCFs as illustrated in Fig. 3.5 because XT accumulates along the transmission and then degrades the SNR [40]. Moreover, the other parts of SMF-based systems, such as amplifiers and connectors, have been optimised and perform better than those in MCF systems, which influences the MCF capacity of long-haul transmission as well. However, with a power-efficient modulation format and power-efficient optical transmission design, 12-core fibre can provide 105.1 Tbit/s over 14350 km [118] while 0.52 Pbit/s over 8830 km [119]. It results in a capacity and distance product of more than 1 Ebit·km/s which is around ten times that of SSMF.

Chapter 4

Multi-core fibre design Artificial-intelligence tool kit

AI is the study of artificial agents or machines which mimic the behaviour of humans or animals to perceive the environment, understand the problem and take actions to maximize the probability of solving the problem with the optimal solution. It was found to be an academic discipline in 1956. After experiencing the AI winter, it started to revive in the early 1980s and became one of the hottest topics in the 20th and 21st centuries.

AI comprises several classes, such as supervised learning, Reinforcement learning, and swarm intelligence. They are used for different purposes, such as search and optimisation, classification, and regression. AI has been applied to various aspects of optical transmission and networking [120].

In the physical layer, AI has been used to optimise the device designs. For example, few-mode fibre [121] and holey fibre [122] have been optimised by Inverse design. As for the few-mode fibre, the neural network is trained to predict the mode effective refractive index with fibre layer widths and refractive index differences as inputs. Then, few-mode fibre is inversely designed to support multiple modes and maintain a low effective refractive index difference between modes. Similarly, Genetic Algorithm (GA) minimises the fitness function, the sum of the dispersion from 1500 nm to 1600 nm, for the individuals which comprise the structural parameters of the holey fibre. Subsequently, after iterative optimisation, the optimised holey fibre is designed.

AI helps improve the configuration and operation of devices. Meta-heuristic algorithms have been tested to optimise the SOA switching [123] and it is proven that PSO has achieved a faster settling time with a lower cost spread compared to Ant Colony Optimisation (ACO) and GA. PSO has also been used to optimise the launch power for maximising the throughput [124, 125]. By optimising the launch power profile, the impairment brought by loss or noise and Raman scattering over the bandwidth are compensated and the SNR of channels is improved.

Optical performance monitoring and optimisation also have been conducted with AI techniques, for example, training Neural networks with raw data from the coherent receiver to monitor optical SNR [126, 127]. Impairment mitigation such as phase noise

has been realised using Maximum likelihood detection [128] or using Machine learning [129]. Moreover, deep learning has been used for optical fibre communication system optimisation by implementing the system as an end-to-end deep neural network [130].

Similarly, networking planning, resource allocation and self-configuration, self-optimisation are conducted with AI methods. The routing and wavelength assignment (RWA) problem has been solved with various AI algorithms, such as GA [131], swarm intelligence [132] or simulated annealing [133]. Network topology design and reconfiguration can be conducted with GA [134] or Artificial Neural Network (ANN) [135] and make the network aware of the impairment or traffic.

In the past years, AI techniques have proved their ability to tackle problems in the various aspects of telecommunication and networks. As illustrated in Fig.4.1, compared to the traditional MCF design method, ML methods and particle swarm optimisation algorithm are used to learn properties in MCF and optimise MCF for different objectives. This chapter introduces and elaborates on the AI techniques used in this work.

According to the application requirements, the ML tools of optical properties are picked for prediction. The training data for ML tools of optical properties are collected with Matlab and Lumerical. Then, the data are pre-processed with Python. The pre-processing of standardization is based on the Sklearn library. Most regressors and classifiers are based on fully connected Neural Network (NN) from the Tensorflow Keras model. The cutoff-wavelength and the coating-loss tools are based on the XGBoost which is an open-source software library providing a regularizing gradient boosting framework. All the training is conducted with Python.

Then the optical properties values are input into the objective function of PSO. After optimisation, the MCF design is obtained and analysed on optical properties and transmission performance.

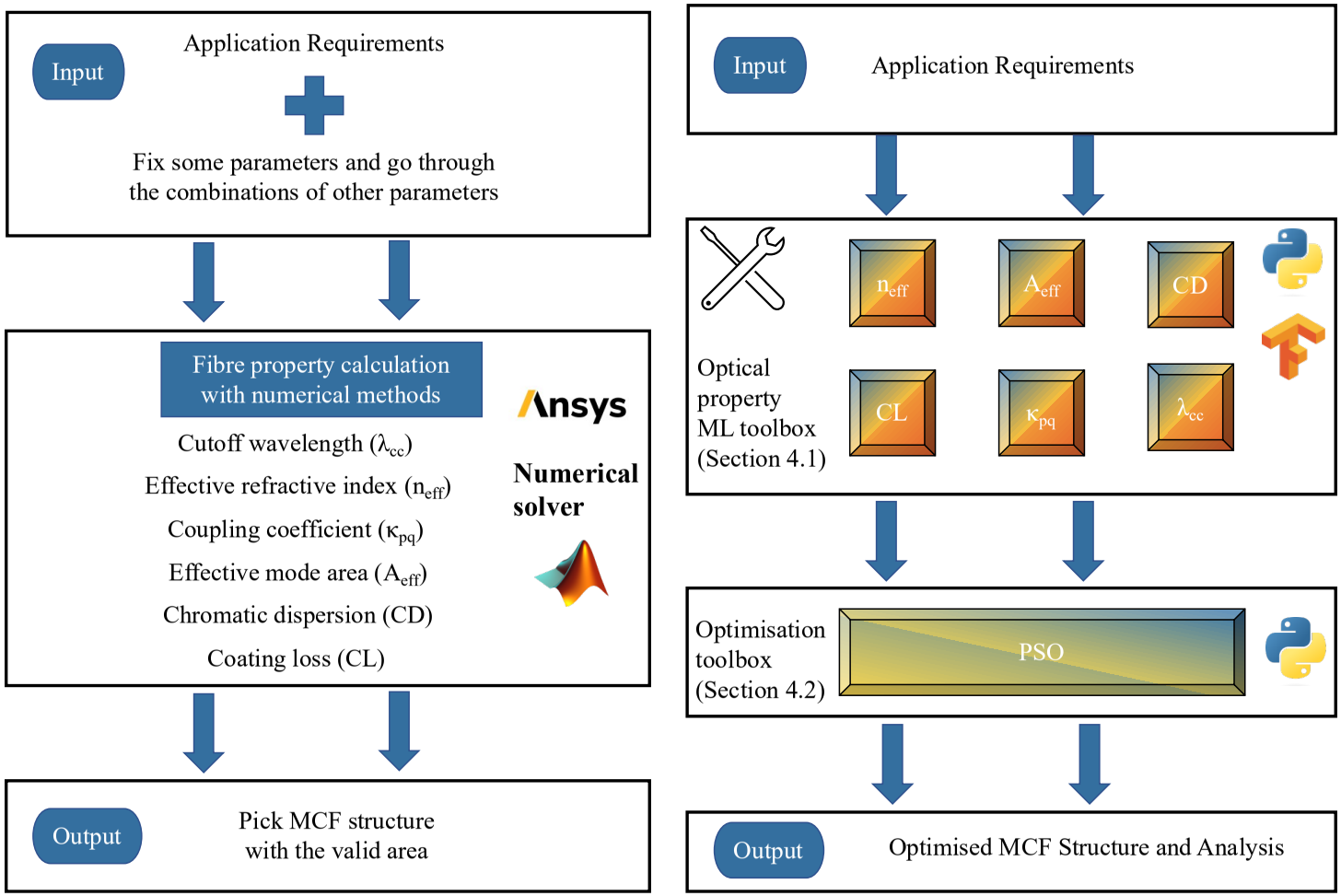

Fig. 4.1: (a) Traditional MCF design process; (b) AI-based MCF optimisation tool kit.

4.1 Machine learning for modelling multi-core fibre properties

Machine learning methods are utilised to model the optical properties. Even though the PSO will reduce the permutation number compared to the brute force method, the particles will calculate the optical properties for each MCF structure especially when the fabrication samples need to be evaluated in the optimisation process. Hence, using ML to speed up the calculation is necessary. Meanwhile, the trained ML model can be used in other MCF calculations. At first, the data sets of the optical properties data were collected via numerical methods as depicted in Fig. 4.2. The definition and calculation methods have been described in Chapter. 2. In this part, the ML methods used to build up the toolbox will be reviewed first as Section. 4.1.1. Then, the training process and the toolbox evaluation will be elaborated on in the Section. 4.1.2,

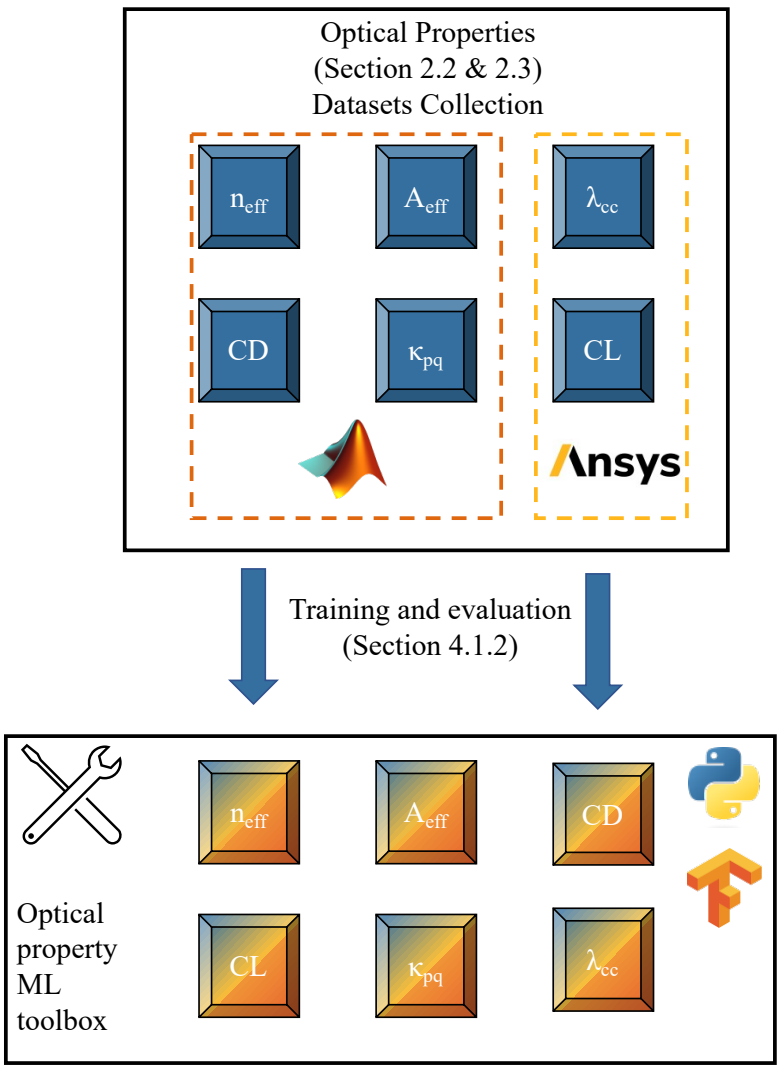

Fig. 4.2: Data collection of optical properties for ML toolbox training.

4.1.1 Machine learning methods review

4.1.1.1 Neural Network

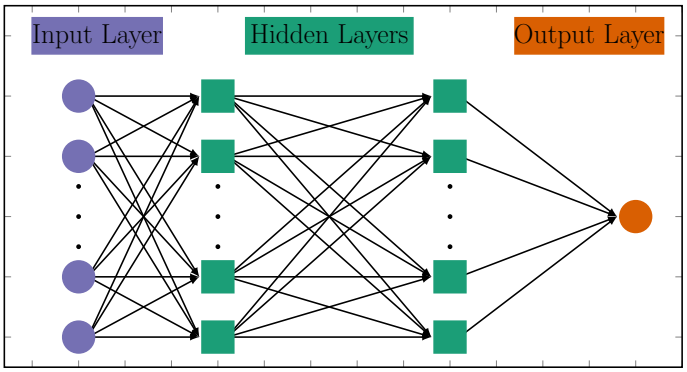

Fig. 4.3: Diagram of neural network

In 1943, W. S. McCulloch and W. Pitts [136] simplified the behaviour of neurons and indicated the similarity to the logical functions. Meanwhile, they proposed the concept of mimicking the brain which inspired the neural network. In 1951, the very first ANN—SNARC (Stochastic Neural Analog Reinforcement Calculator)—was built with 40 neurons. Subsequently, Perceptron was developed by Frank Rosenblatt. It is a two-layer neural network that enables pattern recognition. With further development of neural networks, various types of neural networks are proposed, for example, feed-forward ANN and recurrent ANN. They are always trained with labelled data, which is termed supervised learning. The labelled data are pairs of inputs and output. The neural network which includes multiple hidden layers between the input layer and output layer, as in Fig. 4.3, learns the relationship between the data pairs and at the end of the training, it is supposed to predict the output with arbitrary inputs. The following paragraphs will introduce the mathematics of the basic neural network components.

- **Neurons**: Each point in hidden layers is a neuron. The mathematical operation in a neuron is illustrated in Fig. 4.4. The inputs x_i, $i = 1, 2, ..., n$ to each neuron first multiply with the corresponding weights ω_i and then added with a bias b. Then the result u is sent to the activation function for obtaining the output y. y will be sent to the neurons of the next layer and become their inputs. The relationship between the inputs and output of a neuron is given by Eq. 4.1.

$$y = f(u) = f(\sum_{i=1}^{n} x_i \omega_i + b). \tag{4.1}$$

- **Activation function**: The activation function plays an important role in neurons because it introduces the nonlinear relationship. Then the neurons can

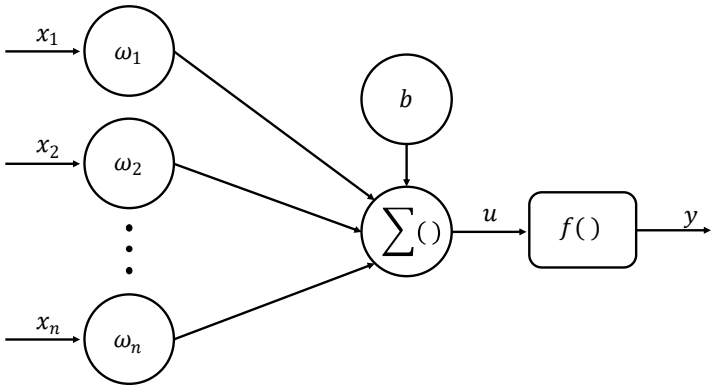

Fig. 4.4: Schematic representation of neuron.

approximate the nonlinear part of the relationship between data pairs. In this work, the Gaussian Error Linear Unit (GeLU) is used as the activation function. GeLU is very similar to the Rectified Linear Unit (ReLU) [137]. ReLU makes the negative values 0 while keeping the positive values as follows:

$$y = max(0, u) \tag{4.2}$$

GeLU function in Eq 4.4 is $x\Phi(x)$ and $\Phi(x)$ is the standard Gaussian cumulative distribution function. The approximation of GeLU function is used here.

$$y = x\Phi(x) = x \cdot \frac{1}{2}\sqrt{1 + erf(\frac{x}{\sqrt{2}})} \tag{4.3}$$

$$\approx \frac{x}{2}\Big(1 + tanh\Big[\sqrt{\frac{2}{\pi}}(x + 0.044715x^3)\Big]\Big) \tag{4.4}$$

When the neurons form the layers and the layers connect one by one, the network is initialised. As mentioned, training neural networks generally aim to approximate the complex function between inputs and output. In other words, the loss function needs to be minimised by adjusting the parameters in each neuron: weights and bias. **w** includes all the weight parameters while **b** includes all the bias parameters.

$$L(\mathbf{w}, \mathbf{b}) = \frac{1}{|P|}\sum_{k=1} l(y^k, f^k_{NN}(x_1, x_2, ..., x_n)), \tag{4.5}$$

where k is the number of outputs and $|P|$ is the cardinality of the training set, usually as a mini-batch. For example, the common loss function used for regression is the mean-squared error while cross-entropy is for classification.

- **Adam optimiser**: Adam optimiser [138] is one of the common and important

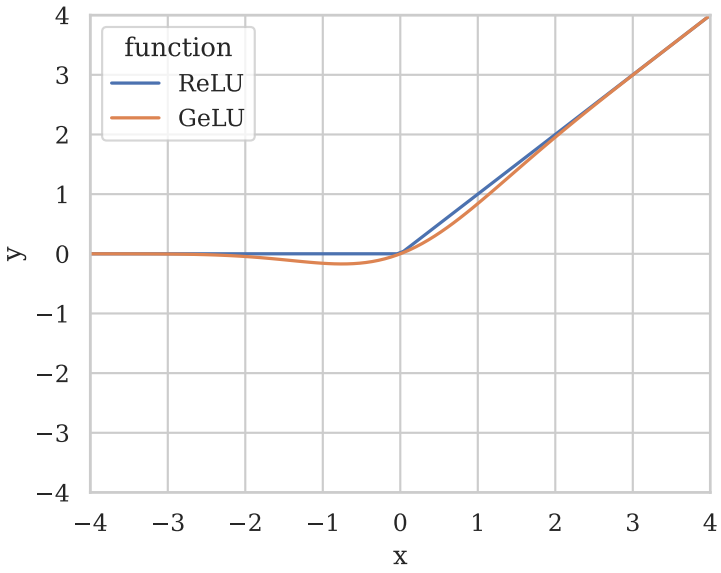

Fig. 4.5: ReLU and GeLU.

optimisation methods to minimise $L(\mathbf{w}, \mathbf{b})$ and it is used in the neural network training following. It is an efficient Stochastic Gradient Descent (SGD) method. Different from the gradient descent, the gradient in SGD is approximated with that calculated with a randomly chosen subset of data. Then the gradient is used to choose the optimisation direction which is the opposite direction of the gradient. In Adam, learning rates are computed dynamically for each parameter by estimating the first-order and second-order moment of gradients and then improving the convergence. To obtain the learning rates, first, the biased first moment u_t and the second moment v_t are estimated with the gradient g_t:

$$u_t = \beta_1 \cdot u_{t-1} + (1 - \beta_1) \cdot g_t, \tag{4.6}$$

$$v_t = \beta_2 \cdot v_{t-1} + (1 - \beta_2) \cdot g_t^2. \tag{4.7}$$

Then they are bias-corrected and used to update the parameters.

$$\hat{u}_t = \frac{u_t}{1 - \beta_1^t}, \tag{4.8}$$

$$\hat{v}_t = \frac{v_t}{1 - \beta_2^t}, \tag{4.9}$$

$$\mathbf{w}_t, \mathbf{b}_t = (\mathbf{w}_{t-1}, \mathbf{b}_{t-1}) - \frac{\alpha \cdot \hat{u}_t}{\sqrt{\hat{v}_t} + \epsilon}, \tag{4.10}$$

in which $\beta_1 = 0.9$, $\beta_2 = 0.999$, ϵ is 10^{-8} typically for maintain numerical stability and α is step size.

4.1.1.2 Gradient boosted trees

Coating loss and cutoff wavelength data are collected using the FDE solver in Lumerical. Each set of parameters yields one data point, taking approximately one to two minutes per data point. Due to the time-intensive nature of data collection, we've gathered only around 10k data points. When training the regressors, we opted for eXtreme Gradient Boosting (XGBoost), a gradient-boosted tree model, as it requires less training data.

Gradient boosting [139] is a method that does regression or classification using an ensemble of weak models f_m. The estimation or approximation of the function between the input parameters and the output, $F(x_1, x_2, ..., x_n)$, is the sum of f_m. The weights for the weak models, σ_m, are which can minimize the loss function $l()$ between $F(x_1, x_2, ..., x_n)$ and the output data.

$$F(x_1, x_2, ..., x_n) = \sum_{m=1}^{M} \sigma_m f_m(x_1, x_2, ..., x_n), \tag{4.11}$$

$$\sigma = argmin \sum_{k=1} l(y^k, F^k(x_1, x_2, ..., x_n)). \tag{4.12}$$

These weak models are trained iteratively to learn the residual that is left from the previous model and then the sum of the weighted models gives the minimal loss.

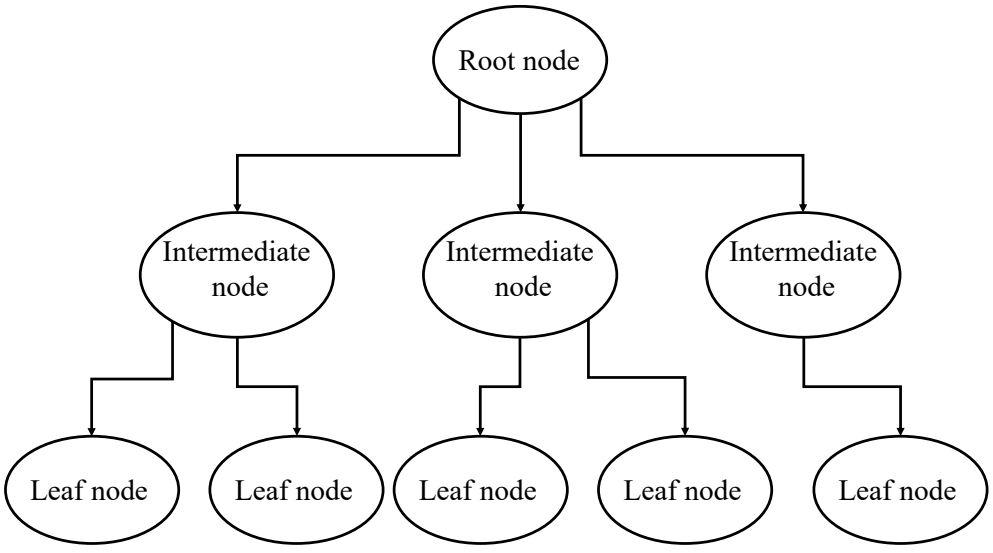

Fig. 4.6: Decision tree diagram.

The decision tree is popular to be picked as the weak model because it is relatively simple and suitable to integrate. Each tree encompasses nodes including the root node, intermediate node and leaf node, and branches. The root node is the topmost node and all the branches start from it. Data is recursively split and goes to intermediate nodes at which the data is evaluated according to the loss function but no decision is made. The

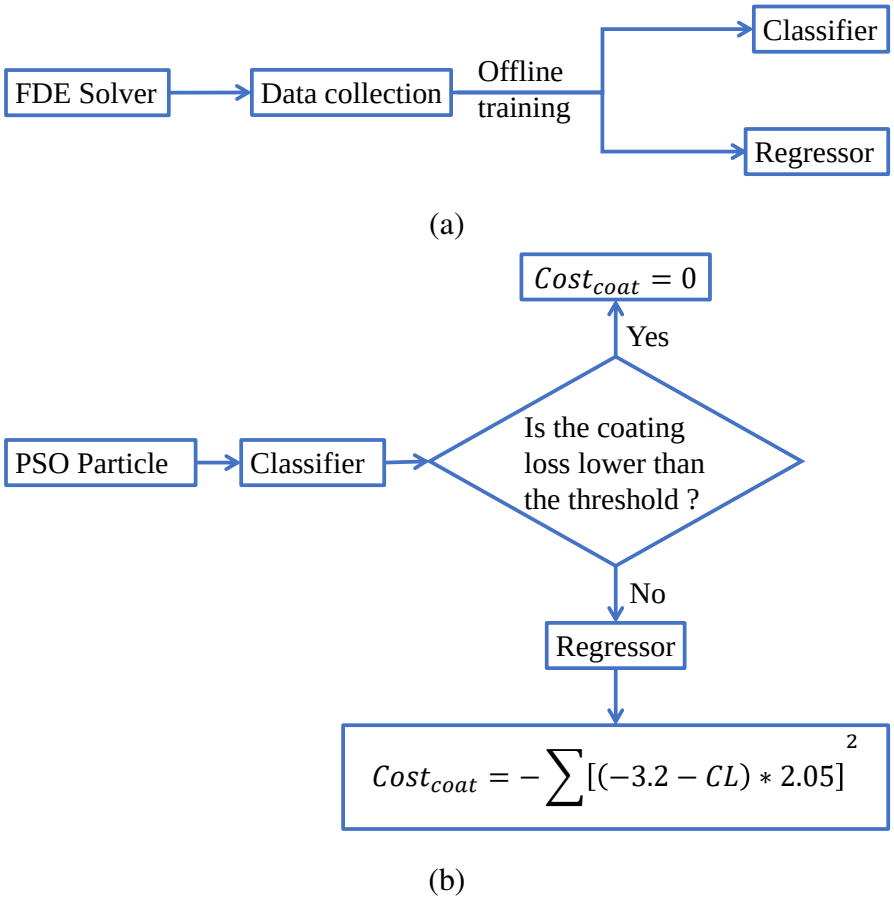

Fig. 4.7: (a) FDE solver is used to collect coating loss data. The data are used to offline train the classifier and regressor; (b) Coating loss estimation process: the $Cost_{coat}$ is used in Eq. 5.1 in section. 5.5.

branching continues until the leaf node where the final decision is made.

4.1.2 Optical properties regressors training and evaluation

4.1.2.1 Coating loss classifier and regressor

The coating loss is defined as the outermost core's bending loss of LP01 at 1625 nm with R_b=140 mm with coating index as 1.475 [30]. Using the FDE solver in Lumerical [140] to calculate coating loss, each calculation would take around 100 s. FDE solver can solve the mode and calculate the loss by comparing n_{eff} with or without the bending. To speed up the coating loss computation, we trained a statistical classifier and a regressor to replace FDE solver in the design process. The regressor and classifier of the coating loss are used in Chapter 5 and Chapter 6.

7000 coating loss data are collected with FDE solver for training the neural networks (both classifier and regressor) as illustrated in Fig. 4.7(a). The inputs of the data are shown in Table. 4.1. The data are split into three parts: 50% for training, 25% for validation, and 25% for testing. Both the classifier and the regressor were implemented

Table 4.1: Index profile parameters range for coating loss and cutoff wavelength dataset.

Parameters	Range	Step	Choices
a_1 [μm]	$4 \sim 6$	0.1	21
w_{cl} [μm]	$2.5 \sim 7.5$	0.1	51
w_{tr} [μm]	$2.5 \sim 7.5$	0.1	51
Δ_1	$0.3\% \sim 0.6\%$	0.01%	31
Δ_2	-0.7% $\sim$ -0.35%	0.01%	36

using a 4-layer fully-connected neural network with the ReLU activation function [137] and the Adam optimizer [138]. The four layers of the classifier have 20, 10, 5 and 1 neurons respectively. The green part illustrates the region where the coating loss is lower than the acceptable threshold and the core structure should be classified as 0. The orange represents where the coating loss is above the threshold and the core structure should be classified as 1 in Fig. 4.8(a). The classifier demonstrated a 99.92% accuracy for the whole dataset. All 0.08% errors merely appear in the green region as illustrated in Fig. 4.8 (b) translating to a few false negative results. Two red dashed lines indicate the error interval [-3.08 -3.03]. And there is no error in the orange region meaning 0% false positives. Thus, there is no output from the classifier that appears to be valid (below the acceptable coating loss) but is actually above it. The four layers of the regressor have 64, 32, 16 and 1 neurons respectively. The regressor resulted in a mean square error of 2.66e-04.

The coating loss of the PSO-designed fibres is also cross-verified with Lumerical. All cores hold the coating loss smaller than the threshold. Classifier inference time is 14 μs and regressor inference time is 32 μs on Nvidia V100 Graphics processing unit (GPU) for a single calculation. Compared to the estimation time using the FDE solver, the classifier and regressor are 10^6 times faster.

In the coating loss estimation in Fig. 4.7(b), the classifier checks whether or not the coating loss of the core is higher than 0.001 dB/km. If it is higher than the threshold (being classified as 1 (negative) by the classifier), the regressor is utilized to calculate the magnitude of the coating loss and the output of the regressor is used in the fitness value calculation to make the coating loss penalty $Cost_{coat}$ in the objective function continuous. The $Cost_{coat}$ is only used in the fitness value calculation for the invalid particles in Eq. 5.1 that appears in the following section. For the valid particles, since the $Cost_{coat} = 0$, the fitness value is not influenced by the coating loss.

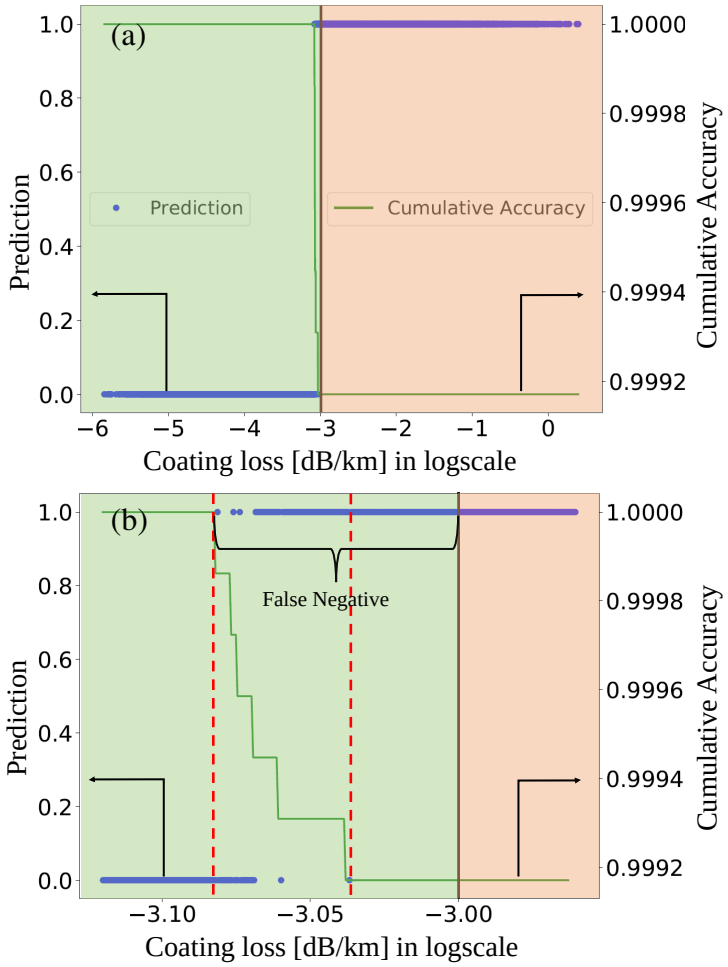

Fig. 4.8: (a) The prediction performance and the cumulative accuracy of the coating loss classifier; (b) Zoom-in of (a) around the threshold.

4.1.2.2 Cutoff wavelength regression

The TA fibre core has a different loss mechanism compared to the step-index cores [22]. Since TA fibre core is insensitive to bending, its bending loss is not significant around the cutoff wavelength. Instead, the leakage loss of LP11 mode determines the cutoff wavelength. Thus, in this work, a regressor of cutoff wavelength is trained based on the loss of the LP11 mode when the fibre is in straight condition. The cutoff-wavelength regressor is used in the Chapter. 6, which is also one of the innovation points of Chapter. 6. Because in the previous work, the unique loss behaviour of the trench-assisted fibre core is not considered in the cutoff wavelength calculation or prediction. Thus, the cutoff-wavelength regressor provides an accurate and time-efficient estimation of the cutoff wavelength in the trench-assisted fibre core.

The five core-index parameters in Table 4.1 are the inputs of the regressor. The data is collected with the FDE solver in Lumerical. A dataset of 10k core profiles and their associated cutoff wavelengths is utilised in the regressor training as shown in Fig. 4.10(a). In data pre-processing, it is found that there is a high correlation between

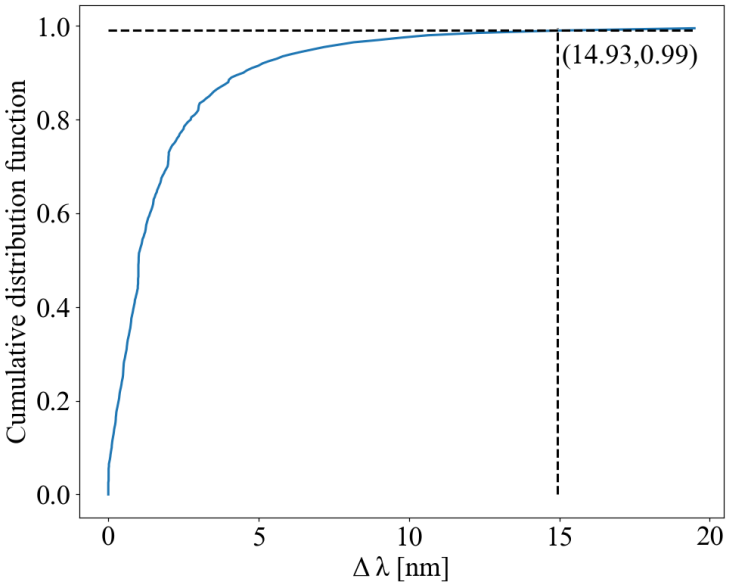

Fig. 4.9: Cumulative density function of cutoff wavelength regressors increases with absolute error range.

each input (each and every parameter of a core profile) and output (cutoff wavelength). Hence, one multivariate linear regressor is trained for presenting the linear relationships between inputs and output. Then, the other multivariate linear regressor is trained for the linear relationships between any of the multiplications of feature pairs and the first-order residual. In the end, the second-order residual of the data is used to train an XGBoost regressor. The workflows used to create cutoff wavelength regressors and to predict the cutoff wavelength are illustrated in Fig. 4.10. After the hyper-parameter optimisation, the regressors are proven to predict the cutoff wavelength with an absolute error of 14.93 nm to be the 99% cumulative density function (cdf) in Fig. 4.9. Therefore, in the MCF optimisation, the cutoff wavelength criterion is set to be $(1530 - 14.93)$ nm for CL-band fibre and $(1460 - 14.93)$ nm for SCL-band fibre. The regressors inference time on Nvidia A100 GPU is 2.45 μs for a single calculation. The regressors are 10^7 times faster compared to estimation time using Lumerical FDE solver.

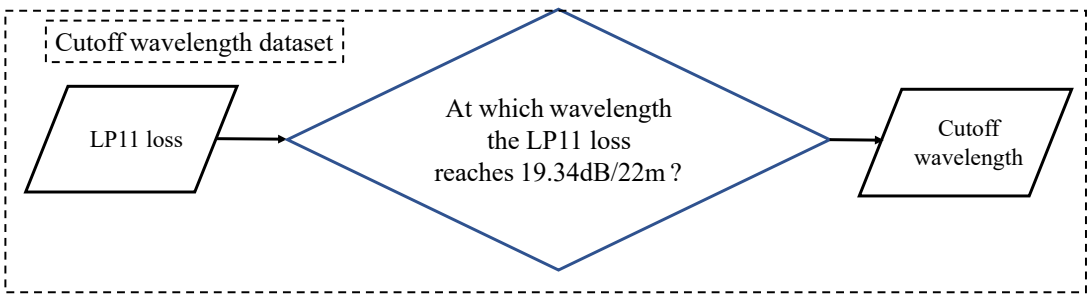

(a)

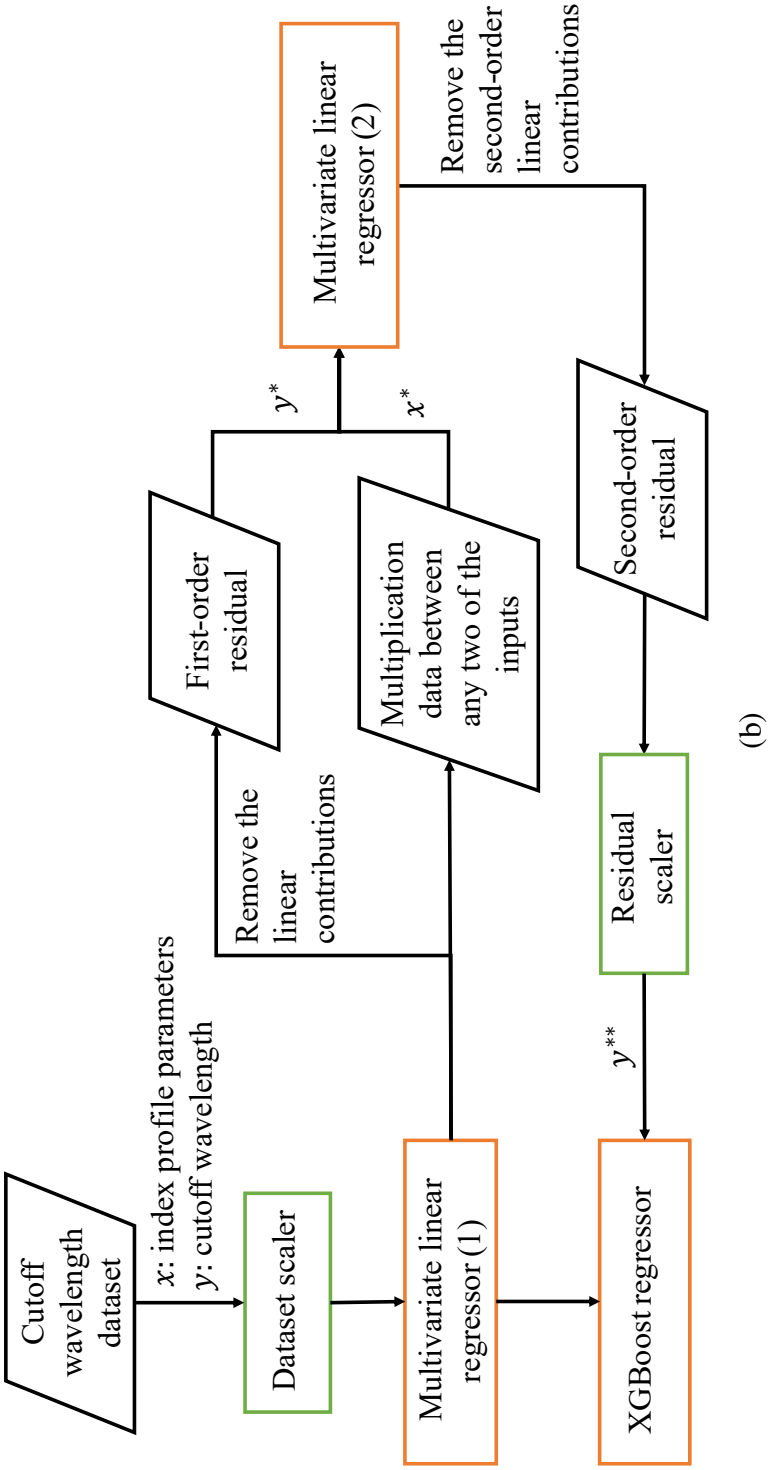
Cutoff wavelength dataset
x: index profile parameters
y: cutoff wavelength
Dataset scaler
Multivariate linear regressor (1)
XGBoost regressor
y**
Residual scaler
Second-order residual
Remove the second-order linear contributions
Multivariate linear regressor (2)
y*
First-order residual
Remove the linear contributions
x*
Multiplication data between any two of the inputs

(b)

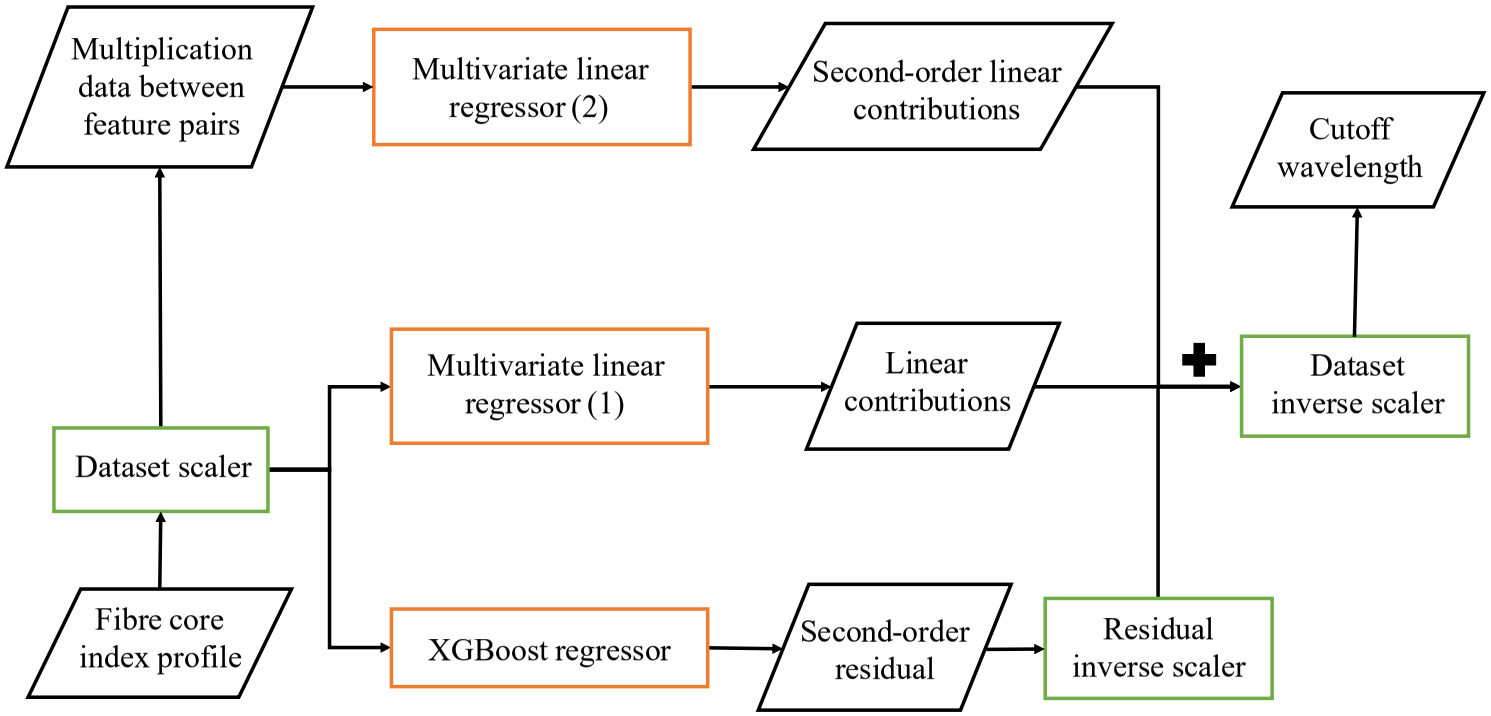

(c)

Fig. 4.10: (a) workflow to create cutoff wavelength dataset; (b) workflow to train cutoff wavelength regressors; (c) workflow to predict cutoff wavelength for one fibre structure.

4.1.2.3 Regressors and classifier for fabrication yield optimisation

In this section, the regressors and classifiers used in Chapter. 7 are elaborated. For each optical property, the data samples are collected while the input variable is Sobol sequence within the parameters' range and deviation shown in Table. 4.2, which makes the data cover the search space more evenly. As for the core position, r is the distance of the core center to the fibre center, θ is the angular coordinate in which the N is the core ID number.

Table 4.2: Index parameters per core for datasets including fabrication error.

Parameters	Range	3σ	deviation
a_1 [μm]	$4 \sim 6$	$\pm$ 0.1	$\sim \pm$ 0.15
w_{cl} [μm]	$2.5 \sim 7.5$	$\pm$0.1	$\sim \pm$ 0.15
w_{tr} [μm]	$2.5 \sim 7.5$	$\pm$0.1	$\sim \pm$ 0.15
Δ_1	$0.3\% \sim 0.6\%$	$\pm$0.01%	$\sim \pm$ 0.15%
Δ_2	-0.7% $\sim$ -0.35%	$\pm$0.01%	$\sim \pm$ 0.15%
Position	r = 32.5[μm] $\theta = \frac{(N-1)\pi}{3}$ $N = 1, 2, .., 6$	x,y$\pm$0.1[μm]	CP $\pm$ 0.25[μm] OCT $\pm$ 0.15[μm]

The 10^5 data of n_{eff}, A_{eff}, CD are calculated with mode solver [17]. With the mode obtained with the mode solver, the coupling coefficient between heterogeneous cores is calculated according to Eq. 2.78 [28]. The 10^4 data of cutoff wavelength [2] and coating loss data are collected with FDE solver in Lumerical. They are based on the LP11 mode loss in straight and bending conditions respectively. As for coating loss, the classifier and regressor work together to make sure that none of the MCF which has coating loss exceeds the threshold and the cost of coating loss can be continuous [1]. Because of the deviation of core position, the data of coupling coefficient has one more dimension of the core pitch while that of coating loss has the distance of the core centre to the fibre centre.

The data set goes through standardization as pre-processing and then is divided into three parts: 60% training, 20% validation and 20% test. Then another new preprocessing is introduced before the training. For each optical property, the correlation between the features and the property is checked at the beginning. If there is a high correlation, one multivariate linear regressor is trained to present the linear relationships between inputs and output. Then, the correlation is checked among any of the multiplications of feature pairs and the first-order residual. If there is a high correlation, another multivariate linear regressor is trained to present this second-order

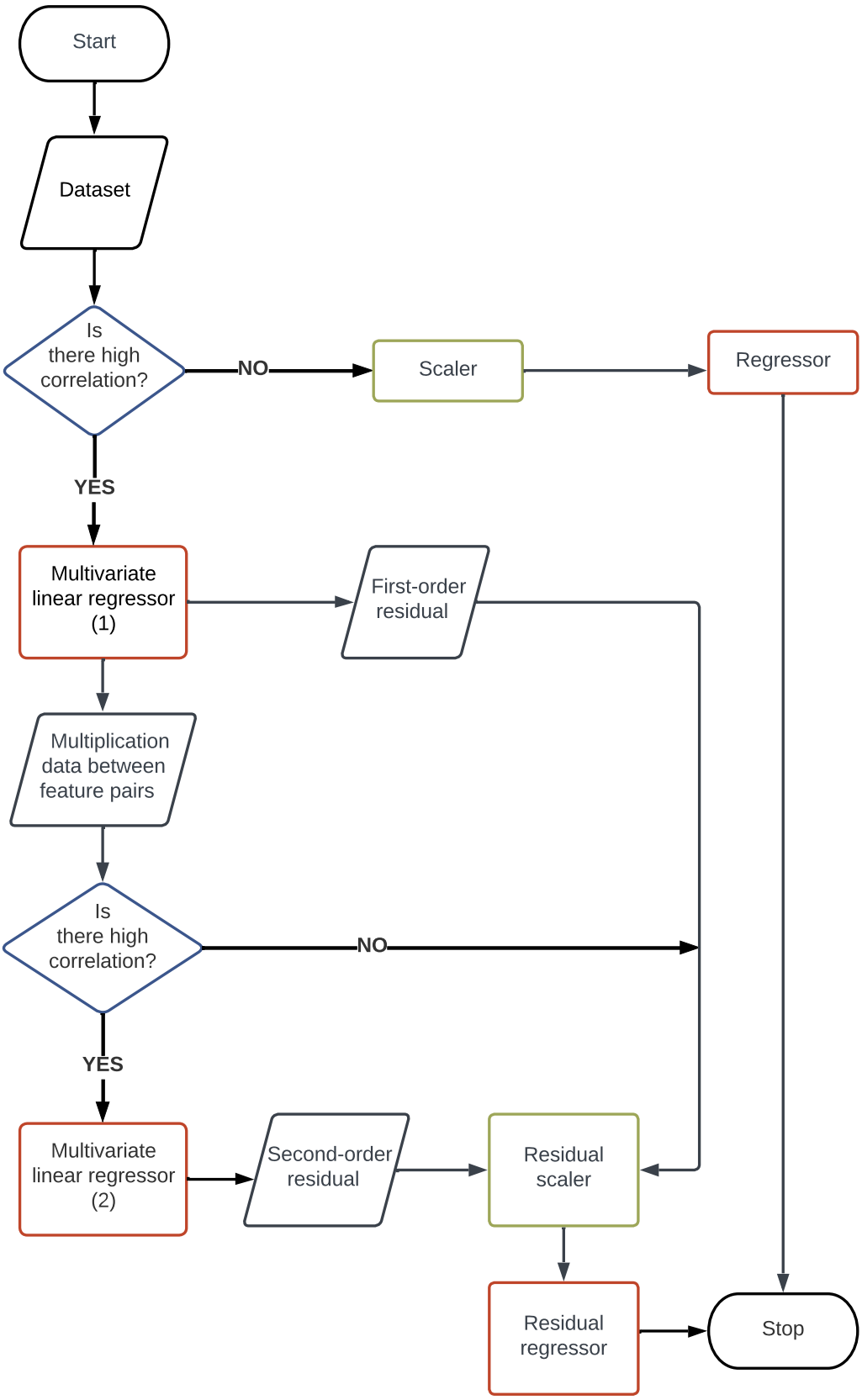

Fig. 4.11: The flowchart of regressors training for each optical property.

linear relationship. After removing all the existing linear relationships, one regressor of the residual is trained. The flowchart of the regressor training is illustrated in Fig. 4.11. As a result, the regressors can focus on the residual learning which leads to regression error with small Standard deviation (STD) and average relative error.

The summary of regressors and the comparison to the numerical methods are included in Table. 4.3. In this table, firstly the residual level (first or second) is shown. 'first' represents the regressor of the linear relationship between the inputs and output, and the regressor of the first residual is trained. 'second' means that apart from the linear relationship between the inputs and outputs, the regressor of the linear relationship between any of the multiplications of feature pairs and the first-order residual and the regressor of the second-order residual are trained. As for the regressor type, the NN is reviewed in section 4.1.1.1 and XGBoost is reviewed in section 4.1.1.2. The STD of the error (Error sd) and the average of the relative error are used to show how close the prediction of the regressor and the data are. The STDs of the error are below 0.01 in most cases. The STDs of the error for the cutoff wavelength regressor is around 5. Because the cutoff data has a wider range of around 1000 nm. The relative error in percentage is the ratio of the average absolute error to the data value, which can show the relative position of the error away from the actual data. For example, although the STD of cutoff error is larger than other regressors, the relative error of the cutoff wavelength is 0.21$\%$. On the other hand, the magnitude regressor of the coating loss has the highest average relative error, 2.46$\%$, that's because the magnitude of the coating loss is single-digit. Furthermore, the comparison of the calculation time of 2500 sets of data is conducted between the regressors and the numerical methods. The ML method speeds up the calculation $5e4 \sim 5e6$ times.

	n_{eff}	A_{eff} $[\mu m^2]$	CD [ps/km/nm]	λ_{cc} [nm]	κ_{pq} (6-core fibre)	Coating loss classifier	Coating loss magnitude regressor
Residual level	first	first	first	first	second		first
Regressor type	NN	NN	NN	XGBoost	NN	NN	XGBoost
Parameter number	45k	45k	12k		47k	707k	
Error std	6.04e-8	9.06e-4	0.0017	5.27	5.84e-05	99.61% (accuracy)	0.024
Average relative error $[\%]$	4.69e-5	0.001	0.0047	0.21	0.011	NA	2.46
Interference time* $[ms]$	5.3	3.28	1.93	36.35	2.48	9.98	16.65
Numerical method Interference time* $[s]$	244.64	254.08	2113.70	∼2500 min	4728.89	∼2250 min	
Acceleration	4.62e4	7.75e4	1.10e6	4.13e6	1.91e6	5.07e6	

∗interference time is the computation time for 2500 fabrication samples

Table 4.3: Machine learning methods summary and comparison to the numerical methods.

4.2 Particle swarm optimisation algorithm for multi-core fibre optimisation

4.2.1 Particle swarm optimisation algorithm review

Global optimisation seeks to find the global minimum or maximum of a function or a set of functions. It includes deterministic methods, stochastic methods, heuristics, and meta-heuristics. Swarm intelligence, a heuristic method, relies on interactions among individuals within the swarm for problem-solving. In this work, a popular part of the swarm intelligence method, the PSO algorithm, is used. R. Eberhart and J. Kennedy [141] proposed PSO in 1995 for nonlinear function optimization.

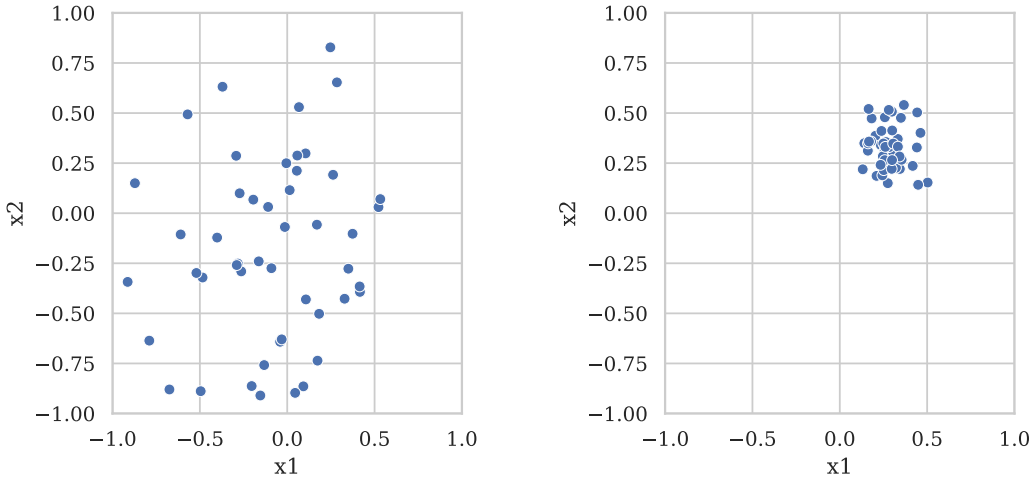

Fig. 4.12: Initialisation (left) and Convergence (right) of swarm of particles.

Each particle $\mathbf{x}_p = (x_{p1}, x_{p2}, ..., x_{pm})$ in the swarm can be regarded as one potential solution to the problem, which includes m variables. The boundary of $\mathbf{x}_p$ variables is set as $\mathbf{x}_{max}$ to limit particles inside the regime in which the problem solutions are valid. The optimization direction is described by the velocity $\mathbf{v}_p = (v_{p1}, v_{p2}, ..., v_{pm})$. $\mathbf{v}_{max}$ is used to constrain the velocity at a reasonable level preventing chaos.

$$\mathbf{v}_{max} = \tau \mathbf{x}_{max}, \tag{4.13}$$

$$\mathbf{v}_{min} = -\mathbf{v}_{max}. \tag{4.14}$$

The active region is usually 20% of $\mathbf{x}_{max}$, which means $\tau = 0.2$. At the beginning of the optimisation process, particles are initialised randomly within the boundary. As for velocity initialisation, it can start with zero velocity or in a similar way to the particle: random value with $\mathbf{v}_{max}$ and $\mathbf{v}_{min}$. The latter way will lead to more research initially.

The problem to be solved is described with an objective function. For each particle, the fitness value is calculated with the objective function. During the

optimization process, each particle adjusts its optimization direction appropriately according to its fitness value and other particles' fitness value at each iteration. Firstly, as an independent individual, the particle needs to think according to the best solution that the particle finds so far which is denoted as $\mathbf{p}_{best}$. Simultaneously, every particle is surrounded by its neighbouring particles. As a social group, they communicate with each other. The best solution obtained by the local neighboring group is called l_{best}. If considering the whole group, the global best solution obtained is called $\mathbf{g}_{best}$. Both self-thinking and social communication influence the final decision on how to update the optimization velocity and the potential solution. Otherwise, the particles will continue flying in the original direction. The updated equations of each particle and their corresponding velocity are as follows:

$$\mathbf{v}_p^i = \mathbf{v}_p^{i-1} + c_1 \cdot \mathbf{s} \cdot (\mathbf{p}_{best}^{i-1} - \mathbf{x}_p^{i-1}) + c_2 \cdot \mathbf{s} \cdot (\mathbf{g}_{best}^{i-1} - \mathbf{x}_p^{i-1}), \tag{4.15}$$

$$\mathbf{x}_p^i = \mathbf{x}_p^{i-1} + \mathbf{v}_p^i. \tag{4.16}$$

$\left(\mathbf{p}_{best}^{i-1} - \mathbf{x}_p^{i-1}\right)$ is considered as cognition component and $\left(\mathbf{g}_{best}^{i-1} - \mathbf{x}_p^{i-1}\right)$ is social component. Let $\mathbf{s}$ be a $1\times m$-dimension matrix of realisations of the positive random variable in [0 1]. The constants c_1 and c_2 determine the influence weight of the two components on the velocity and they are termed learning rates.

Several strategies have been proposed to control the update velocity. In [142], Y. Shi et al. introduced an inertia factor, ω.

$$\omega_i = \omega_{max} - \frac{i(\omega_{max} - \omega_{min})}{i_{max}}, \tag{4.17}$$

$$\mathbf{v}_p^i = \omega_i \mathbf{v}_p^{i-1} + c_1 \cdot \mathbf{s} \cdot (\mathbf{p}_{best}^{i-1} - \mathbf{x}_p^{i-1}) + c_2 \cdot \mathbf{s} \cdot (\mathbf{g}_{best}^{i-1} - \mathbf{x}_p^{i-1}), \tag{4.18}$$

$$\mathbf{x}_p^i = \mathbf{x}_p^{i-1} + \mathbf{v}_p^i. \tag{4.19}$$

On the other hand, M. Clerc et al. [143] proposed a new constriction factor K for preventing the explosion, especially when $\mathbf{v}_{max} = \mathbf{x}_{max}$.

$$\mathbf{v}_p^i = K(\mathbf{v}_p^{i-1} + c_1 \cdot \mathbf{s} \cdot (\mathbf{p}_{best}^{i-1} - \mathbf{x}_p^{i-1}) + c_2 \cdot \mathbf{s} \cdot (\mathbf{g}_{best}^{i-1} - \mathbf{x}_p^{i-1})), \tag{4.20}$$

$$K = \frac{2}{\left|2 - \varphi - \sqrt{\varphi^2 - 4\varphi}\right|}, \tag{4.21}$$

in which $\varphi = c_1 + c_2 > 4$. When $c_1 = c_2 = 2.05$, it corresponds to $K = 0.73$.

PSO as a meta-heuristic algorithm has the ability to handle problems with different backgrounds to some extent. However, the hyper-parameters still influence the optimisation process and results. Lots of research has been conducted on parameter selection. There are many hyper-parameters that can be tuned: population size,

neighbourhood size, update ways, c_1 and c_2, φ and $\mathbf{v}_{max}$. The selection of hyper-parameters depends on the problem nature. In this part, the common approaches used to choose or change hyper-parameters are reviewed.

- **population size**: To solve most benchmark functions, 30 particles can achieve 100% success with small computation cost [144]. When the problem to solve becomes more complex, more particles are needed but the rule of choosing particle number is to increase the success rate while maintaining a low computation cost.

- **neighbourhood**: When particles communicate with their neighbours, the number of neighbours they talk to and the neighbour topology will influence the optimisation process. The neighbour number can increase from 2 to the global group. Limiting the neighbours in the local group may enhance particles' search ability while choosing the global group can let particles converge. Compared with other hyper-parameters, the neighbourhood has relatively small effects. Thus, global communication is usually chosen to reduce the complexity.

- **update strategy**: PSO can be divided into two types: synchronous and asynchronous. In the synchronous case, the fitness value of particles is calculated before the velocity and particle update. That is to say that the best solutions are found first then the particles move to optimise together. In the asynchronous case, the particle is updated as soon as its corresponding best solutions are found. The asynchronous update strategy is generally applied when the local neighbourhood is chosen because the particles will have different communication components.

- **learning rates**: If $c_1 = 0$ only, the algorithm is social-only; if $c_2 = 0$ only, the algorithm is cognition-only. To control the learning rate of self-thinking and communication with others, generally, $c_1 = c_2 = 2$. The mean of $\mathbf{s}$ is 0.5 and the c_1 and c_2 can increase its mean to 1, which sets the mean of velocity to the cognition and social component themselves. The equalisation between c_1 and c_2 can keep the balance between cognition and communication.

  c_1 and c_2 can also be dynamic. A. Ratnaweera, et al [145] propose that c_1 decreases linearly from 2.5 to 0.5 while c_2 increases linearly from 0.5 to 2.5.

$$c_1 = (c_{max} - c_{min})\frac{t}{T} + c_{min}, \tag{4.22}$$

$$c_2 = (c_{min} - c_{max})\frac{t}{T} + c_{max}, \tag{4.23}$$

  where T is the maximal iteration number while t is the iteration number. Therefore, the particles place a higher value on self-thinking to search and

gradually close to the global best solution to converge. In [146], nonlinear learning rate functions are proposed.

$$c_1 = c_{min} sin\left(\frac{\pi}{2}\tau_1 \frac{(T/2 - t)}{T/2}\right) + c_{max}, \tag{4.24}$$

$$c_2 = c_{min} sin\left(\frac{\pi}{2}\tau_2 \frac{(t - T/2)}{T/2}\right) + c_{max}, \tag{4.25}$$

in which $c_{min} = 1$ while $c_{max} = 1.5$. Then, c_1 and c_2 are between 0.5 and 2.5. τ_1 and τ_2 determine the degree of non-linearity and it has been proven that they can be between 0.75 and 1.15. The non-linearity leads to more iterations with large c_1 and small c_2, which enhances the ability of search.

- **Inertial factor**: Similar to the learning rates, it can be a constant or change with the iteration linearly or non-linearly to improve the local search precision. In most cases, it starts from a relatively large value, for example, between 0.9 and 1.2. Then, it decreases linearly with iteration to a small value, for example, between 0.4 and 0.1. Large ω leads to a fast and wide search while small ω results in a precise local search. Thus, PSO can have a quick search over the whole search space at the beginning and then make a local search accurately and converge at the end of optimisation. The most used is the linear decrease from 0.9 to 0.4.

  In addition, 15 strategies of change inertia weight have been summarised in [147], and based on 5 common optimisation function results, it drew the conclusion that the random inertia factor [148] and Chaotic inertia factor [149] in the below equations leads to the best efficiency and accuracy respectively.

$$\omega = 0.5 + rand()/2. \tag{4.26}$$

$$\omega = (\omega_1 - \omega_2) \times \frac{T - t}{T} + \omega_2 \times z, \tag{4.27}$$

  where $z = 4z(1 - z)$ and z is initialised as a random number in (0 1). ω can also change adaptively with the evaluation factor f [150].

$$\omega(f) = \frac{1}{1 + 1.5e^{-2.6f}}, \tag{4.28}$$

  or with the distance between the particle and g_{best} [151].

$$\omega_i^t = \omega_i^{t-1} - \alpha_i^t g_{\omega,i}^t. \tag{4.29}$$

- **Ending criteria**: The criteria to determine whether the optimisation process can be stopped is usually the maximal iterations. When the iteration number reaches

the maximum, the optimisation is finished. This is a simple choice but may lead to computation waste or insufficient optimisation. Therefore, more criteria have been proposed [152]. If the $\mathbf{g}_{best}$ is not changed for many iterations, for example, 100 iterations, it can be concluded that PSO can not find a better global solution. The other one is from the convergence. When almost all the particles, for instance, 95%, have the same fitness value as the global best solution, the particles converge around the $\mathbf{g}_{best}$ and have little search-ability. These two criteria can prevent the waste of computation and monitor the behaviour of the particles then accordingly change the hyper-parameters.

In 2005, PSO has been utilized to optimize the quantization error and intra-cluster distances and the inter-cluster distances simultaneously in the image clustering [153]. Compared against K-means, fuzzy c-means (FCM), K-Harmonic Means (KHM), H_2 and GA, PSO has better performance. H.M. Elkamchouchi et al. [154] used PSO to solve the power control problem in CDMA system. Compared with GA application to the same problem, PSO obtained a better solution. And F.R. Durand et al. [155] introduced PSO into the power allocation of WDM network. Its great performance-complexity trade-off and fairness attracted researchers compared with other optimization methods. All in all, PSO has shown its ability in many complex optimization problems.

4.2.2 PSO workflow for MCF Optimisation

In this work, based on the fitness values given by the objective functions, the global best particle ($\mathbf{g}_{best}$) and the personal best particle ($\mathbf{p}_{best}$) can be picked for each generation of particles. They are included in the velocity update and then the velocity determines the particles moving path as Eq. 4.15 and 4.16. Meanwhile, the inertia factor ω decreases iteratively. The hyper-parameters used in this PSO algorithm are shown in Table. 4.4.

Table 4.4: Hyper-parameters used for PSO-base MCF design.

population size	100; 200;
neighbourhood	global
update strategy	synchronous
learning rate	$c_1 = c_2 = 2$
inertia factor	$\omega_{max} = 1, \omega_{min} = 0.1$
ending strategy	99% particles converge or $\mathbf{g}_{best}$ is not updated for more than 30 iterations
maximum iterations	500

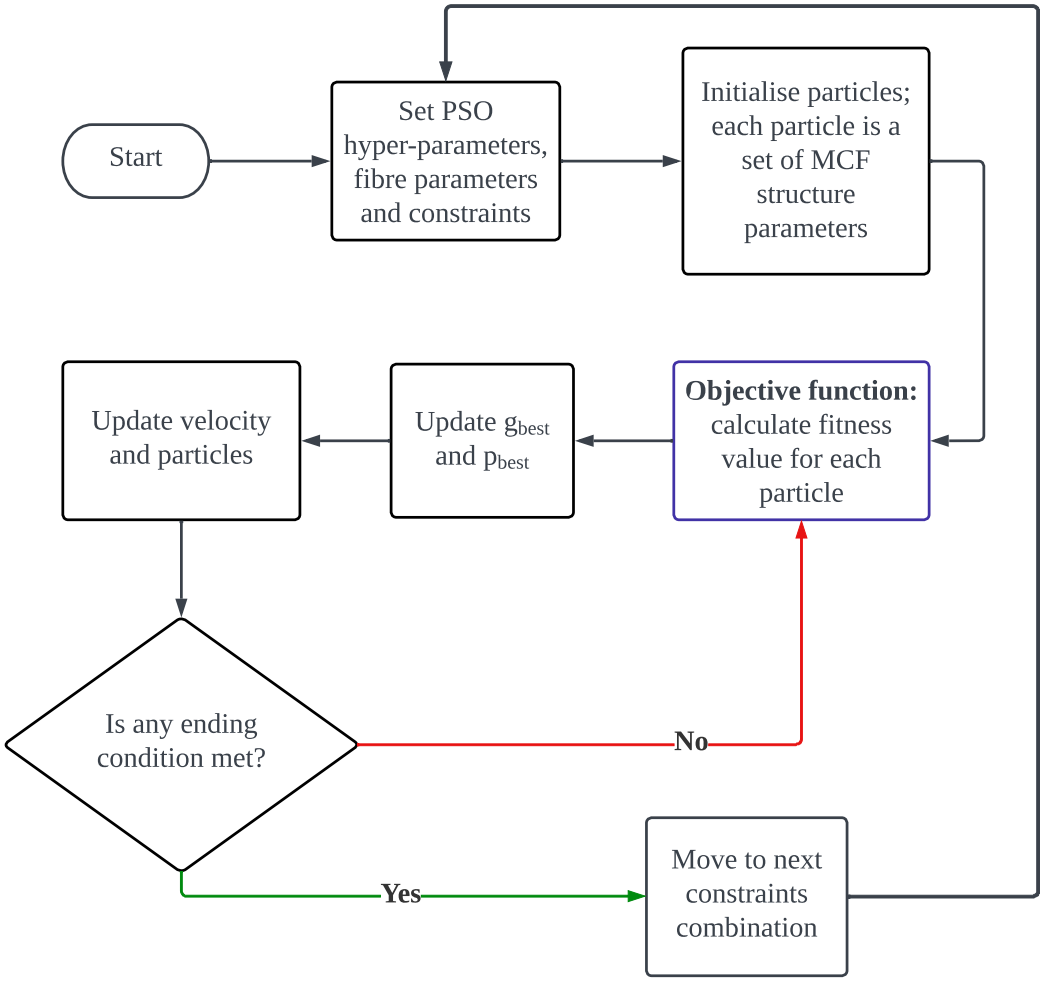

Fig. 4.13: Workflow of MCF optimisation process with PSO.

The workflow of the PSO-based fibre design process is illustrated in Fig. 4.13. The first step is to set up the PSO hyper-parameters and the fibre parameter ranges while giving constraints on the optical properties. Then the particles are initialised randomly within the parameter ranges and put into the objective function. In different applications, the objective function is designed to cover the requirements. In the following chapters, the design of the objective function will be explained in detail. In brief, there would be three objective functions: A_{eff}*-optimisation* for maximising A_{eff}, *XT-optimisation* for minimising XT and *yield-optimisation* for maximising fabrication yield. In *XT-optimisation*, the particle number is set as 100 while in A_{eff}*-optimisation* and *yield-optimisation*, the particle number is set as 200. With the fitness values calculated for particles, the updates on best solutions, particles and velocity are conducted. Then, the ending criteria are checked. The process will go to the next optimisation iteration if none of them is met otherwise move to the next constraint combination.

4.3 Summary

This chapter summarised the ML methods used to build up the MCF optical property toolbox and the PSO algorithm used in the optimisation toolbox. In the traditional methods, the mode in the fibre core needs to be solved first and then the optical properties are calculated based on the mode profile and the mode indices. The ML methods eliminate the mode solver and replace the numerical methods of optical properties calculations, which significantly speed up the computation and renders it feasible to optimise MCF structure and even consider the fabrication error to make thousands of fabrication samples around each MCF structure. Furthermore, according to the application requirements, the objective functions are designed to include these optical properties predicted with the ML toolbox. The PSO algorithm searches the optimal MCF structure efficiently. In the following chapters, the AI-based MCF optimisation toolkit was utilised in three scenarios and the toolkit performance and the obtained MCFs were investigated.

Chapter 5

Optimisation of 6-core multi-core fibres design with coating loss tool

5.1 Associated publications and contributions

The main part of this chapter was presented in the poster session of OFC 2021 and was published as a journal paper. In both, the author of this thesis is the primary author. In addition, a patent about the method proposed for designing and optimising MCF is filed. Specific details and contributions (bullet pointed below title) for each of these relevant papers are detailed below.

Mu, X., Ferreira, F. M., Ottino, A. and Zervas, G. Design optimisation of uncoupled six-core fibres in standard cladding diameter using artificial intelligence. In Optical Fiber Communication Conference (OFC) 2021, Th1A.34.

- Primary author;
- Lead researcher.

Mu, X., Ottino, A., Ferreira, F. and Zervas, G. Optimisation of 125-μm heterogeneous multi-core fibre design using artificial intelligence. IEEE Journal of Selected Topics in Quantum Electronics 28, 1–13 (2022).

- Primary author;
- Lead researcher.

Mu, X., Ottino, A., Ferreira, F. and Zervas, G, "Methods and apparatus for optical fibre design and production, " P122374GB, filed on 28 May 2021, UKIPO.

- Lead inventor.

5.2 Chapter summary

A high-level summary of the problem/motivations, proposed solution, and outcomes, as related to this chapter, is:

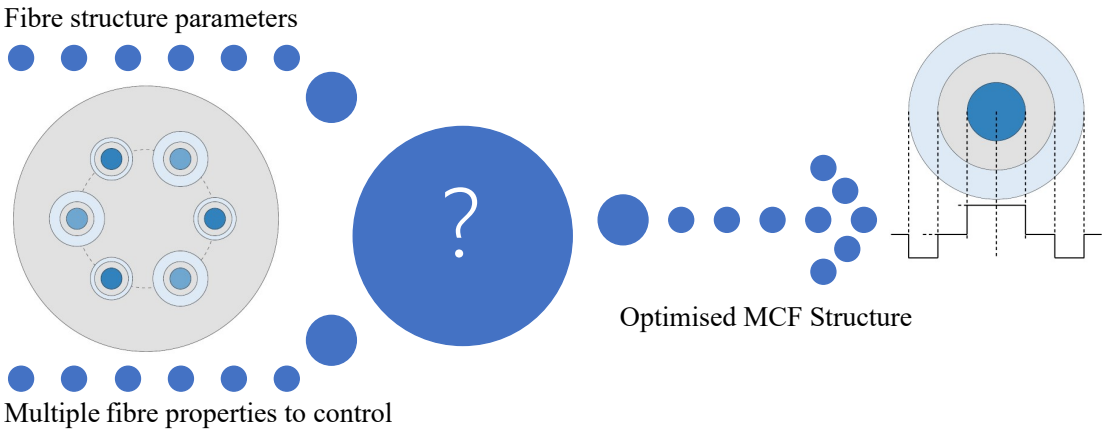

Fig. 5.1: Visualising the problem described in this chapter. How can the MCF be designed while controlling multiple fibre parameters and multiple fibre properties?

- Problem: as illustrated in Fig. 5.1, each MCF has tens of structural parameters to control while several properties need to be addressed. How can MCFs be designed for different application requirements efficiently, reliably and automatically?

- Proposed solution: a method based on PSO algorithm is proposed to optimise MCF structure with an objective function which includes the requirements of fibre properties.

- Outcomes:

  - The regressor and classifier for predicting coating loss in MCFs are trained as shown in the section. 4.1.2.1. The classifier can provide zero false positives while the regressor of the coating loss magnitude results in accurate prediction.

  - MCFs are designed for two objectives, *XT-optimisation* and A_{eff}-*optimisation*, under different combinations of property-constraints (cut-off wavelength and A_{eff}). It proves that this AI-based method has the capability to design TA MCFs.

  - In *XT-optimisation*, ultra-low XT MCFs are obtained while in A_{eff}-*optimisation*, MCFs with large A_{eff} are designed.

  - The capacity of the designed fibres is estimated and it is found that they can deliver up to 1.2 Pbit/s for 1200 km transmission. Meanwhile, by comparing it with the reference, it shows that the MCF designed for S+C+L band has a significantly higher capacity.

5.3 Introduction

As mentioned in Chapter 3, MCF is one of the promising solutions to the capacity crunch. However, while there has been significant research on MCFs design, design strategies are often presented in an ad-hoc fashion by omitting critical reasoning and underlying strategies such as in [30]. Also, it is often the case that optimisation only considers a subset of the parameters that analytically define the refractive index profile. For example, in [71], for a W-type pure silica core, layer widths are pre-selected and set as constants. Only the relative refractive index difference between the core and the depressed layer (Δn), and CP, which is the distance between the centre of two cores, are independent variables to calculate the inter-core XT and the excess loss. Then, according to the requirement of inter-core XT and the excess loss threshold, a 2-dimensional search space (Δn, CP) is defined, over which optimal fibre design search takes place. A *core selection method* is proposed in [105] where the refractive-index profile of the core at the outer and inner layers is decided individually.

To approach an optimal MCF structure all the fibre parameters need to be considered together. Considering all the parameters while controlling the optical properties makes the MCF design a multi-dimensional and multi-constraint problem. Targeting such a complex problem with a brute force method would be time-consuming and impractical, especially for heterogeneous MCFs (Hete-MCFs). Instead, we propose using artificial intelligence to optimise the design of Hete-MCFs over all refractive-index profile parameters. PSO algorithm [120], as one of the most important swarm intelligence paradigms, is chosen to realize this work. The algorithm itself has been described in Section 4.2.

In this chapter, the design of heterogeneous TA 6-core MCFs on a standard 125 μm cladding diameter is explored. A single-ring layout is chosen to prevent the cutoff wavelength elongation and inter-core XT degradation associated with having a central core. To reduce the design and fabrication complexity a symmetric fibre design with *N*/2 same pairs of dissimilar cores - with even *N* was considered. Each core (in the pair) can be described by five design parameters defining the refractive-index profile while fixing the cladding as pure silica. The parameters are optimised within the domain compatible with current fabrication constraints and limited resolution is assumed for easy fabrication as shown in Table. 4.1. Despite this simplification, brute force would be unpractical, for instance, considering discrete values per parameter leads to more than 3.7×10^{15} permutations. By adjusting the objective function and corresponding fitness value, PSO can be utilized to search for near-optimal Hete-MCF structures with various conditions and constraints of mechanical and optical properties while significantly reducing the number of permutations evaluated compared to the brute force method (from $\sim 10^{15}$ to $\sim 10^{5}$). Moreover, the computation of the

attenuation degradation caused by coating [30] which is noted as Coating Loss (CL), is sped up (from $\sim$ 100 s to ~ 50 μs) using a statistical classifier and a regressor based on neural networks.

Up to now, the capacity of the MCFs has not been taken into account quantitatively during the design process but rather measured experimentally upon fabrication. The capacity of a single-mode MCF link is directly related to the bandwidth of each fibre core, the number of cores supported and the SNR limited by linear and nonlinear effects. The achievable SNR is limited by the NLI noise and inter-core XT introduced by the link fibre and by the ASE noise introduced by the link optical amplifier. Optimising the capacity of MCF is a multi-dimensional problem. It involves complex relationships among the fibre parameters that either directly or indirectly influence the three main factors: core number, cutoff wavelength (i.e. bandwidth), and SNR, as described in Chapter 1. Specifically, it is the refractive-index profile of the fibre core and the core distribution which directly determine the cutoff wavelength, the modal effective area (A_{eff}) ($\propto$ 1/NLI) and inter-core XT. Furthermore, how these influence the theoretical maximum capacity was explored. In this work, using fabrication viable constraints MCFs were designed using PSO to optimise inter-core XT or A_{eff} with different cutoff wavelengths while satisfying key constraints (non-overlap and CL) such that how the capacity is influenced by the parameters is explored.

The following focuses on Hete-TA-MCF. The TA refractive-index profile has stronger light confinement ability than the conventional step-index while it is easier to fabricate compared with the hole-assisted or rod-assisted structures. For the heterogeneous structure, the n_{eff} difference between the cores leads to propagation constant difference. The influence of this propagation constant difference on the power coupling between a core pair depends on the bending radius (R_{b}). When R_{b} exceeds the critical bending radius, it can benefit from the non-phase matching and get a low XT.

The automated method proposed here uses the PSO algorithm to explore the optimal MCF structures for two objectives, a) minimal overall XT under certain constraints on A_{eff} and cutoff wavelength, and b) maximal A_{eff} with certain cutoff wavelength constraint for MCFs in standard cladding diameter with silica cladding. The output of the PSO feeds the ISRS GN model [55] to calculate the SNR and in turn the capacity of the fibre. The obtained results are used to showcase the influence of individual parameters and are also compared to the existing MCFs to validate the effectiveness of the method.

5.4 MCF profile and design strategies

The schematic diagrams of Hete-TA-MCF and its refractive-index profile are shown in Fig. 2.6. For the 6-core fibre, the central core is removed. Making use of symmetry to reduce the search space and the complexity of fibre design, we assumed two types of cores. They all have neighbouring cores non-identical to themselves so that they can benefit from the n_{eff} difference. The cores have fixed positions on the ring uniformly. The core pitch is set at 32.5 μm for 6-core fibres since the outer cladding diameter is set to be 30 μm [34], larger values would lead to non-negligible coating loss. With various layer widths, the fibre should meet the mechanical feasibility conditions:

1. The distance between the adjacent trenches' edges is larger than or equal to 2 μm to prevent the cores from overlapping with each other [75].

2. The coating loss needs to be less than 0.001 dB/km [30]. The coating loss is estimated by classifier and regressor in Section 4.1.2.1.

It assumes that the core is doped with germanium, the trench is doped with fluorine [13], and both the inner and outer cladding index are fixed as the index of pure silica. There are the five refractive-index profile parameters which become variables for each core, including the layer widths (a_1, w_{cl}, w_{tr}) and the relative refractive index differences (Δ_1 and Δ_2) as illustrated in Fig. 2.6. Since it is assumed that two neighbouring cores have non-identical refractive-index profiles, there are 10 variables in total to be optimised for each MCF structure. According to the fabricated MCF core index profiles [34, 70, 71, 72], the parameters are limited in certain ranges as shown in Table 4.1.

One of the fibre design strategies is the constraint to single-mode operation for preventing the inter-modal XT— defined by the cutoff condition. The cutoff wavelength can be assessed by checking the cutoff condition at different wavelengths, for instance, 1530 nm, 1460 nm and 1360 nm. Thus, the bending loss of LP01 should be smaller than 0.5 dB/100turn when R_b=30 mm at 1625 nm in ITU-T recommendations G.655 and G.656 while the bending loss of LP11 need to be larger than 1 dB/m when R_b=140 mm [94, 156]. The bending loss is calculated with the Maxwell equations' solutions described in [157]. The n_{eff} and A_{eff} are calculated by solving the Maxwell equations numerically using the method described in [17].

Four cutoff wavelength targets were set:

1. : cutoff$\leq$1530 nm, MCF can cover C+L band

2. : cutoff$\leq$1460 nm, MCF can cover S+C+L band;

3. : cutoff$\leq$1360 nm, MCF can cover E+S+C+L band;

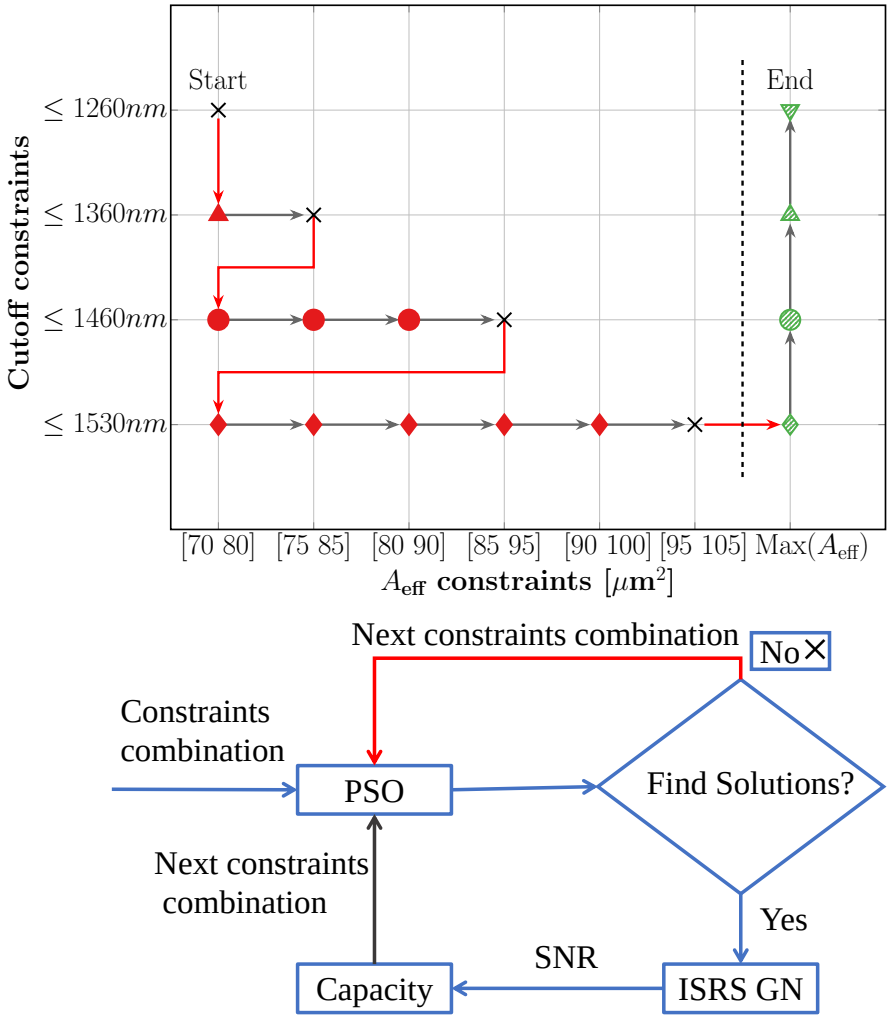

Fig. 5.2: Automated fibre design process through different cutoff and A_{eff} constraint combinations. The flowchart illustrates the actions taken for each combination. Red and black arrows (both in the flowchart and plot) indicate the transition following an unsuccessful and successful fibre design respectively.

4. : cutoff$\leq$1260 nm, MCF can cover O+E+S+C+L band.

XT-optimisation was conducted with PSO using cutoff wavelength constraints and A_{eff} constraints. In the XT-optimisation, five A_{eff} target constraints were used in the range of 70-100 μm^2. The process was initialised by running the PSO under the shortest cutoff wavelength constraint and the smallest A_{eff} constraint, this is: cutoff$\leq$1260 nm and A_{eff} $\in$ [70 80] μm^2. Once the *XT-optimisation* is complete, the *A_{eff}-optimisation* follows with PSO using the associated objective function. The maximum A_{eff} is searched with PSO one by one for four cutoff wavelength constraints. The design process traverses the constraint combinations to optimise the MCF with PSO.

As illustrated in Fig. 5.2, the black cross markers indicate those cutoff wavelength and A_{eff} constraints combinations at which PSO has not found solutions after ten runs (e.g. cutoff$\leq$1360 nm and $A_{\text{eff}} \in$ [75 85] μm^2) satisfying all the constraints. The PSO

then considers the next constraint combination without SNR and capacity calculation. The red markers represent the successful runs using *XT-optimisation* while the green markers are representing the successful runs using the A_{eff}*-optimisation*. Following this, the optimal fibre structure is then passed to ISRS GN model for SNR and capacity calculation.

5.5 Objective function design

The objective function contains all the design requirements. It returns the fitness value to PSO for every particle so that PSO can adjust the optimisation direction properly according to the fitness value. Two objective functions are used, 1) focusing on optimising XT with strict constraints on A_{eff} and cutoff wavelength that it is termed *XT-optimisation* and 2) purely aiming at maximizing A_{eff} for certain cutoff wavelength and it is termed A_{eff}*-optimisation*.

The objective function checks the following constraints in order. The first two are the essential conditions: non-overlap and coating loss. Hence, if they are not satisfied, the particle will be treated as invalid and the fitness value will be returned as

$$\text{Fitness value} = Cost_{\text{overlap}} + Cost_{\text{coat}} \tag{5.1}$$

When they are both satisfied, the valid particles have different objective functions in *XT-optimisation* and A_{eff}*-optimisation*. The fitness value of PSO in the *XT-optimisation* case is

$$\text{Fitness value} = XT + Cost_{A_{\text{eff}}} + Cost_{\text{cutoff}} \tag{5.2}$$

The A_{eff}*-optimisation* fitness value is

$$\text{Fitness value} = -\sum A_{\text{eff}} + Cost_{\text{cutoff}} \tag{5.3}$$

The flowchart of the objective function is illustrated as Fig. 5.3 and the detail of the cost terms is described below:

1. If the distance between the adjacent trench is smaller than 2 μm [28], $\text{overlap}_{pq} = CP_{pq} - (a_{3,p} + a_{3,q} + 2)$ will be smaller than zero. p and q are the core ID of the neighbouring core pair. If overlap_{pq} is below zero, the fitness value suffers a penalty: $Cost_{\text{overlap}} = (\text{overlap}_{pq} * 1e5)^2$. Otherwise, $Cost_{\text{overlap}} = 0$.

2. Firstly, the classifier is used to check if the outer core has a coating loss higher than the threshold. If the output of the classifier is higher than 0.5, the regressor is used to estimate the magnitude of coating loss and the fitness value suffers

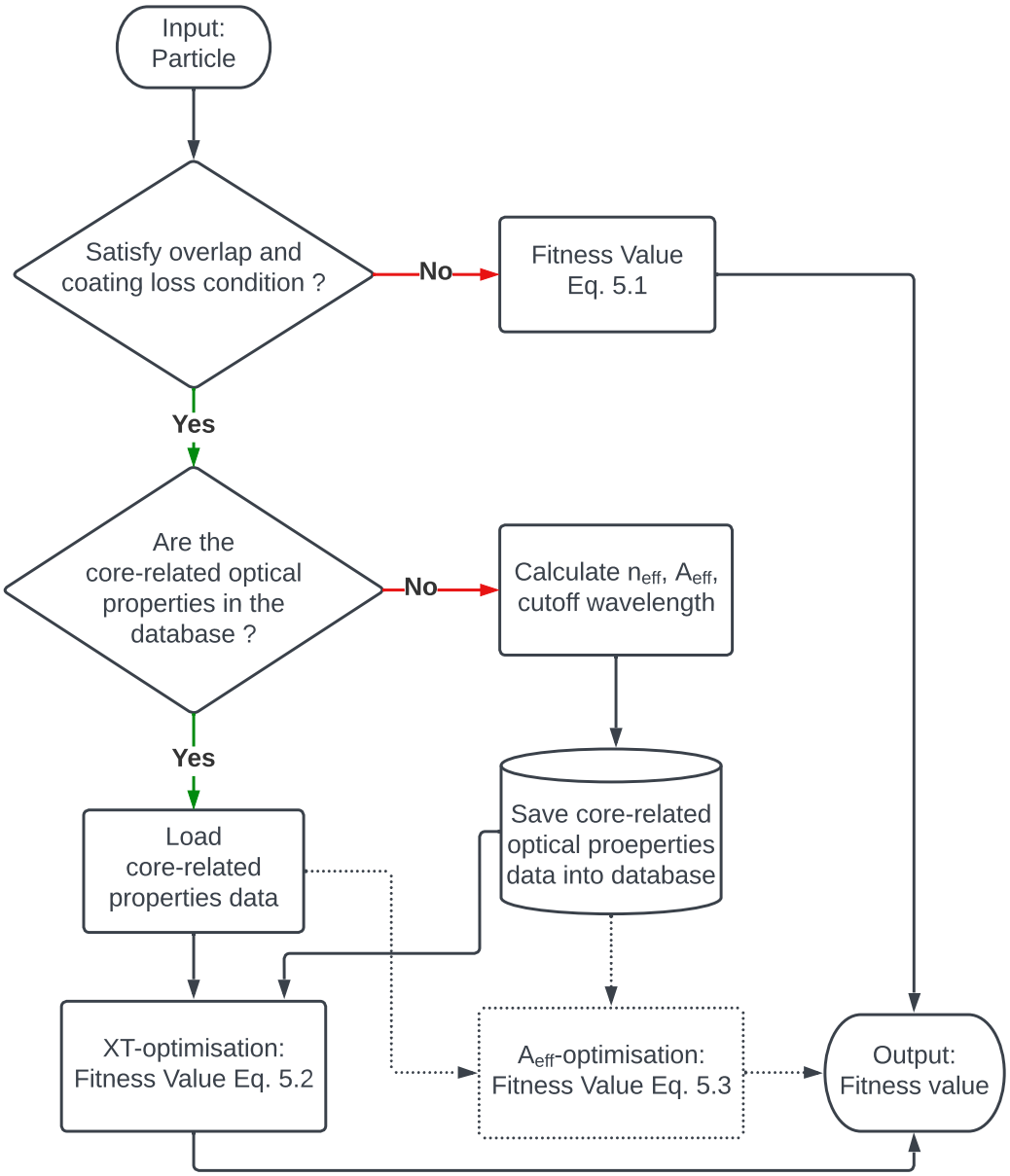

Fig. 5.3: Flowchart of the objective function in *XT-optimisation* and A_{eff}*-optimisation*.

a penalty: $Cost_{coat} = (\sum(-3.2 - CL) * 2e5)^2$ in which CL is the regressor's output for each core.

3. If the cutoff wavelength of the core is higher than the design constraints, the fitness value suffers a penalty: if cutoff>1530 nm, $Cost_{\text{cutoff}} = (\sum(\text{cutoff} - 1530) * 2.05)^2$ taking 1530 nm as the example. Otherwise, $Cost_{\text{cutoff}} = 0$.

4. The A_{eff} at 1550 nm is constrained in a range, for instance, between 75 and 85 μm^2, to offer choices for heterogeneous structure while keeping A_{eff} close to each other. If the core holds a A_{eff} higher than 85 μm^2, $Cost_{A_{\text{eff}}} = ((A_{\text{eff}} - 85) * 50)^2$. If the core holds a A_{eff} smaller than 75 μm^2, $Cost_{A_{\text{eff}}} = ((75 - A_{\text{eff}}) * 50)^2$.

It can be seen that the cost coefficients of overlap$_{pq}$ and CL are much larger than the others. That is to make sure that these two conditions can be satisfied because of the high cost with even a tiny constraint break. As for cutoff wavelength and A_{eff}, the coefficients were initially estimated based on the range of the penalty. The maximums of $Cost_{\text{cutoff}}$ and $Cost_{A_{\text{eff}}}$ are designed to be the same magnitude. Then the fine-tuning is conducted by running the optimisations and checking the cost values at each iteration. If $Cost_{\text{cutoff}}$ keeps high while $Cost_{A_{\text{eff}}}$ is minimised to be zero, the cost coefficient of $Cost_{\text{cutoff}}$ needs to be increased, and vice versa.

5.6 PSO Performance

MCF designs were collected with PSO under various fibre optical properties constraints' combinations for 6-core fibres. In this section, PSO's performance and the designed MCFs' optical properties were evaluated. PSO showed its reliability in different constraint combinations. MCFs have lower XT and good A_{eff} compared to the state-of-the-art.

Compared to $\sim 10^{15}$ permutations needed in the brute force, PSO only needs $\sim 10^5$ permutation calculations to converge to a good fitness value. This ten orders of magnitude reduction mean significant computation improvement. The PSO convergence process and final design result are illustrated for 1460 nm cutoff constraint and [70 80] μm^2 A_{eff} constraint as an example in Fig. 5.4.

The PSO performance was analysed from three aspects: whether it obtains valid solutions, the standard deviation among the valid solutions and how close the fibre structure is given by the valid solutions. In the *XT-optimisation*, except the case — [90 100] μm^2 A_{eff} with 1530 nm cutoff constraints, ten runs of PSO all found valid solutions which satisfy the constraints. In Fig. 5.4(a) and (b) which is the zoom-in of (a) in a small fitness value region, it can be seen that though the maximal iteration number is set as

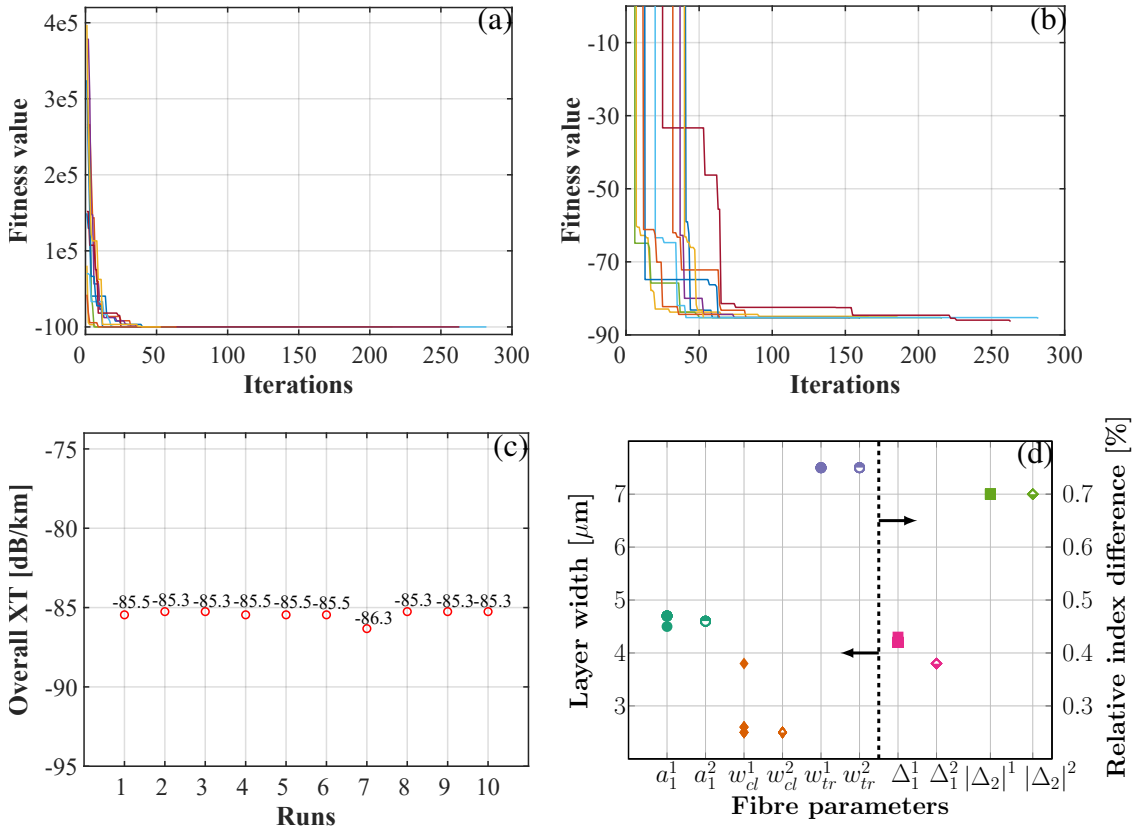

Fig. 5.4: (a) Fitness value decreases with iterations in the [70 80] μm^2 A_{eff} constraint and $\leq$1460 nm cutoff wavelength constraint; (b) Zoom in of (a); (c) The final overall XT which PSO obtained after all the iterations; (d) Parameters in g_{best} of ten runs obtained in cutoff$\leq$1460 nm case (the superscript indicates which core the parameter belongs to);

500, the fitness value reaches the minimum with less than 300 iterations because of the convergence criterion mentioned in Section 4.2.2. The ten runs converged to similar fitness values and the overall XT of the ten runs is shown in Fig. 5.4(c). They are the same as the final fitness value PSO reached, which means that the MCF designs satisfy all the constraints. The exceptional case holds 6 runs which found valid solutions. In the A_{eff}-*optimisation*, all the cases have ten to ten runs obtaining valid solutions.

The standard deviation of the ten PSO results in *XT-optimisation* cases is between 0 to 1.39 dB/km for overall XT. In case of A_{eff}-*optimisation*, it is between 0 to 4.02 μm^2 for A_{eff}. Meanwhile, PSO results obtained in different runs are similar for each constraint combination. Each result contains ten fibre parameters, five for core 1 and five for core 2, shown in Fig. 5.4(d). For each parameter, the values obtained in different runs converge together with a very small variance.

For the fibre structure illustrated in Fig. 5.4(d), an example of their PCC curves to the bending radius is illustrated in Fig. 5.5. For the non-identical core pair in the 6-core fibre, the PCC linearly increases with the bending radius when the bending radius is smaller than the critical bending radius. When it exceeds the threshold, the PCC

decreases sharply and the MCF enters the non-phase matching area.

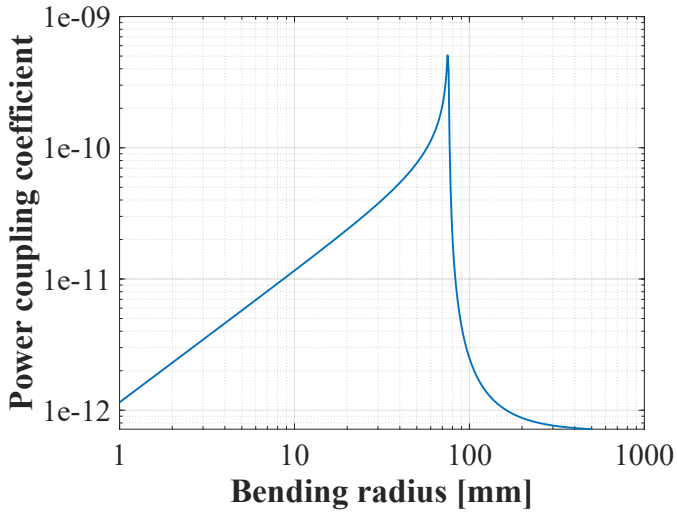

Fig. 5.5: The PCC corresponding to the result in Fig. 5.4(d).

In total, PSO has proved its ability to find out MCF designs satisfying the constraints and to optimise two different fitness values focusing on XT and A_{eff} respectively. Meanwhile, in the ten runs in each case, the similar fitness values and the similar final fibre designs which PSO converges to in ten runs have demonstrated PSO's reliability in MCF design.

5.7 optimised MCF design analysis

5.7.1 XT and RCMF performance comparison

XT-optimisation and A_{eff}*-optimisation* results are illustrated in Fig. 5.6 with green and red markers respectively same as in Fig. 5.2. The blue markers are the fabricated fibres with silica cladding and standard cladding diameters in the previous literature. Because the four blue points have XT characteristics for different bending radii, different transmission lengths and only for core-to-core XT, for comparing our designs with them in the same situation. Their overall XT is calculated based on the core-to-core XT measured. In [68], the details of the MCF index profile are reported so that its overall XT is calculated based on the index profile.

As mentioned in Section 2.4.1, RCMF illustrates the performance of MCF compared with SSMF in terms of core density and A_{eff}. For these MCFs with standard cladding diameter, the RCMF can be calculated as

$$RCMF = \frac{\sum_i^{N_c} A_{\text{eff}}^i}{A_{\text{eff-SSMF}}} \tag{5.4}$$

The aim of MCF design is to achieve higher RCMF and lower XT. These MCF

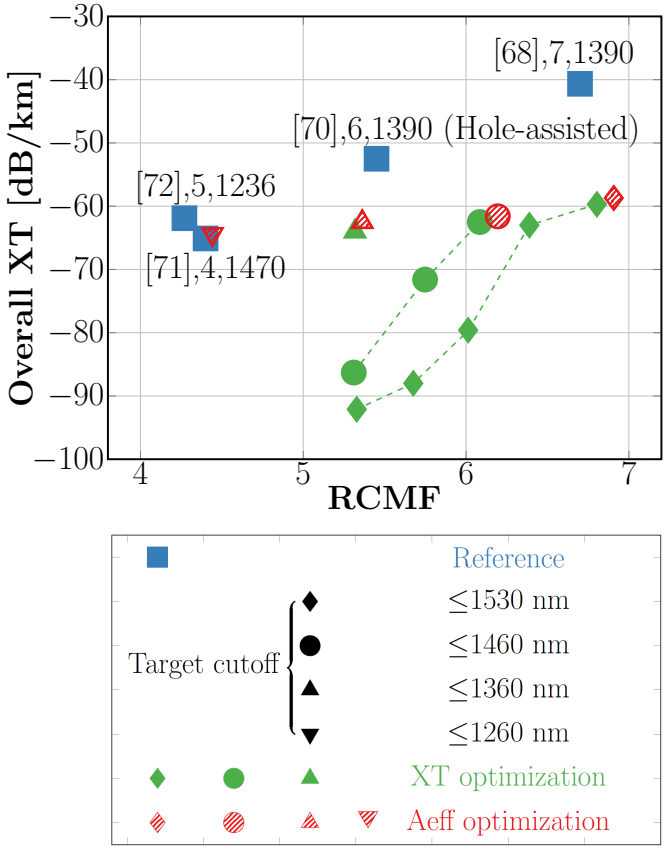

Fig. 5.6: Minimal overall crosstalk obtained with various constraints compared with references. The text next to each mark is [reference number], core number, cutoff wavelength.

designs perform significantly better in terms of overall XT even for similar RCMF. Meanwhile, the RCMF in the result has exceeded that of state-of-the-art.

XT-optimisation objective function aims to minimize the overall XT of MCF while constraining the optical properties as is explained in Section 5.5. Considering the four cutoff wavelength targets starting from the lowest, there are 0, 1, 3 and 5 cases that satisfy the A_{eff} constraint respectively. In each cutoff case, with the increasing RCMF, the PSO-optimised overall XT increases. It can be concluded that A_{eff} and XT have an inverse-proportional relationship when the cladding diameter is fixed.

The lowest overall XT reached with cutoff$\leq$1530 nm is -92.1 dB/km. The XT is 25 dB lower than the lowest XT of the reference points, -67 dB/km. In [158], a universal specification of inter-core XT per unit length, around -60 dB/km is proposed which is suitable for different systems from metropolitan ($\sim$100 km) to trans-pacific ($\sim$10000 km). The optimised 6-core fibres all satisfy this universal specification including the results of $A_{\textit{eff}}$*-optimisation* of which the highest overall XT is -58.7 dB/km.

In $A_{\textit{eff}}$*-optimisation*, the upper limits of A_{eff} were explored without XT constraint. The highest sum of A_{eff} was searched with PSO while constraining cutoff wavelength.

Compared to the *XT-optimisation*, the PSO results sacrificed a small overall XT performance for a higher A_{eff}. Since different A_{eff} constraints have been tested in the previous section, the A_{eff}*-optimisation* just shows a small improvement on A_{eff} compared to the *XT-optimisation* results.

By optimising A_{eff}, the RCMF of these 6-core fibres is up to 6.82 which is higher than the highest RCMF of the reference points, 6.7, in [68]. Comparing the fibres with similar RCMF, the wider bandwidth the worse XT. That is because higher bandwidth requirement leads to limitation of the core choices. This also limits the A_{eff} choice in each cutoff case.

Table 5.1: System parameters for transmission performance evaluation

Parameters	
Channel Bandwidth [GHz]	49.5
Channel Spacing [GHz]	50
Channel Launch Power [dBm]	-2
Noise Figure [dB]	5
Transceiver penalty [dB]	23
Span Length [km]	60
Span Number	20
Total Length [km]	1200

5.7.2 Transmission performance

The SNR and capacity performance of the designed MCFs are calculated using ISRS GN model [55] while taking XT [40] into consideration. Since some of the optimised MCFs have bandwidths wider than 15 THz, the Raman gain coefficient (C_r) cannot be approximated as a constant. Therefore, the Raman equations were solved to obtain the actual power profile and then match it to these power profiles for getting C_r [40]. Capacity was calculated with Eq. 2.101 and Eq. 2.102 in Section 2.4.2.

PSO-designed MCFs perform well in both RCMF and XT. In this section, their SNR and capacity performance was further explored taking both XT and ISRS into consideration. As seen in the following, XT is not a limiting factor for the work, its influence on SNR performance is insignificant even for ultra-long transmission (for XT smaller than or around -60 dB/km). Differently, ISRS shows a strong impact on SNR in MCFs with various bandwidths. As for the corresponding capacity, bandwidth plays the determinant role while the increase of A_{eff} has a small benefit to the capacity.

5.7.2.1 SNR Performance

The simulation parameters for SNR calculation of a single core are listed in Table 5.1. First, the SNR and its various contributions for both *XT-optimisation* and A_{eff}*-optimisation* were compared as depicted in Fig. 5.7. Because the cutoff wavelength constraints are set as smaller than or equal to a certain value, in the low A_{eff} constraint cases, some of the optimised MCF structures hold two largely different cutoff wavelengths. For example, in the [70 80] μm^2 A_{eff} constraint and $\leq$ 1530 nm cutoff wavelength constraint, the two types of core in the optimised fibre have 1356 nm and 1530 nm as cutoff wavelength, respectively. When calculating the XT penalty on the SNR, only the wavelengths which both cores guide are considered. But the cores shown in Fig. 5.7 are with the cutoff close to the constraint for comparing the bandwidth influence.

Fig. 5.7(a)-(c) showcases the cores obtained with *XT-optimisation* objective function. They cover different optical bands with low overall XT. Fig. 5.7(d)-(f) shows the cores optimised A_{eff} but with slightly higher overall XT. Comparing the cores designed with *XT-optimisation* and A_{eff}*-optimisation* objective functions – *that cover the same bandwidth* – the following behaviour was observed. The *XT-optimisation* method leads to lower XT which proved to negligibly or marginally influence the SNR. Specifically, Fig. 5.7(a) shows an XT-induced penalty smaller than 0.001 dB while in Fig. 5.7(d) the penalty is up to 1.6 dB for 1200 km transmission. On the other hand, the A_{eff}*-optimisation* method offers higher A_{eff} that leads to 2.71 dB improvement in SNR from NLI contribution compared to the former. In *Section. 5.7.2.2*, the impacts of XT and A_{eff} on capacity will be further discussed. The O+E+S+C+L-band fibre has a 12.3 μm^2 smaller A_{eff} and 107.6 THz wider bandwidth compared to E+S+C+L-band fibre. This leads to a reduced SNR by 3.18 dB (average) due to NLI contribution as shown in Fig. 5.8.

The cores with wider bandwidth have worse SNR performance in the short wavelength range. The ISRS transfers energy from short wavelengths to long wavelengths during transmission. Thus, at the end of each span, the power at the short wavelengths is lower than that of the long wavelengths. The imbalance in the actual power profile highly influences the ASE contribution and NLI contribution in SNR.

5.7.2.2 Capacity performance analysis and comparison

The capacity performance of each MCF was calculated as the sum of the capacity of each fibre core and compared against various parameters for a better understanding of their influence as illustrated in Fig. 5.9. When considering the total capacity across the *entirety of the supported spectrum of each core* then the performance degraded with increasing A_{eff} in Fig. 5.9(a), which is opposite to what was expected. Larger A_{eff}

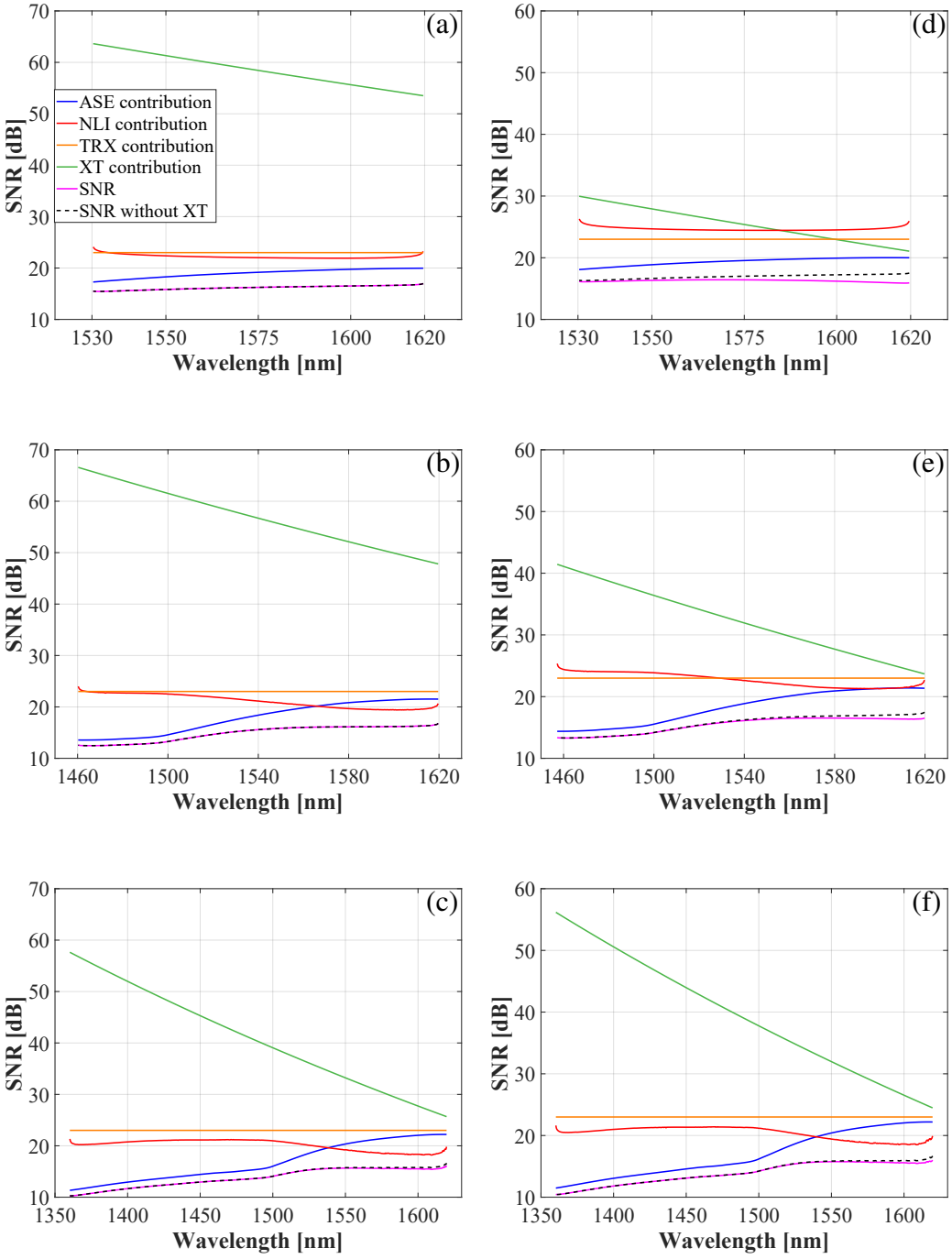

Fig. 5.7: (a),(b),(c) are the cores picked from *XT-optimisation*: (a) Fibre core with A_{eff} $\in$[70 80] μm^2 and cutoff$\leq$1530 nm; (b) Fibre core with A_{eff} $\in$[70 80] μm^2 and cutoff$\leq$1460 nm; (c) Fibre core with A_{eff} $\in$[70 80] μm^2 and cutoff$\leq$1360 nm; (d),(e),(f) are cores picked from A_{eff}*-optimisation*: (d) Fibre core with cutoff$\leq$1530 nm; (e) Fibre core with cutoff$\leq$1460 nm; (f) Fibre core with cutoff$\leq$1360 nm.

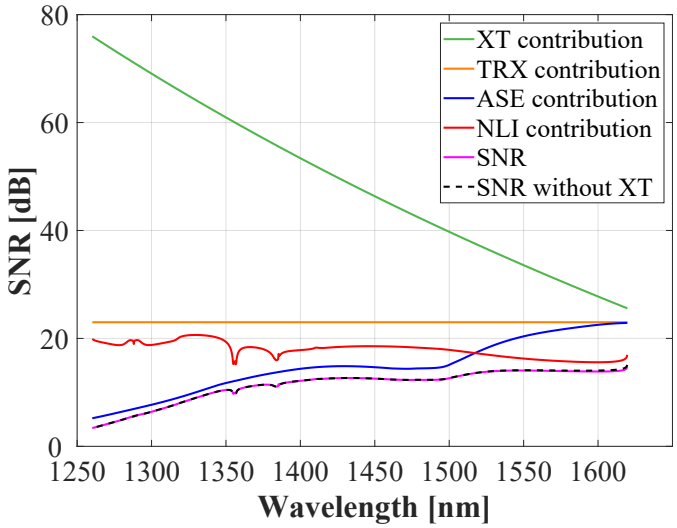

Fig. 5.8: The SNR and its contributions of O+E+S+C+L-band fibre in the A_{eff}-*optimisation*.

(smaller γ) should result in smaller NLI, thus better SNR and larger capacity. When the relationship between total capacity and the total bandwidth of the whole MCF, $\sum_i^N B_{ch}$, is presented in Fig. 5.9(b), it becomes clear that the total bandwidth dominants the capacity performance. The capacity increases almost linearly to the total bandwidth with a slope as ∼4.08 Tbit/s/THz.

If the bandwidth is limited to the optical bands which we designed to cover, the influence of the total bandwidth difference can be eliminated. For example, cores with ≤1530 nm cutoff wavelength constraint support the C+L bands and their associated capacity noted as cutoff-limited capacity. The impacts of XT and A_{eff} on cutoff-limited capacities can be investigated among the fibres having the same cutoff-limited. These fibres which cover the S+C+L band have about 35.1% more cutoff-limited capacity for 1200 km transmission than the 7-core fibre in [68] which also covers the S+C+L band. The fibres supporting O+E+S+C+L-band fibres have 1.68-times higher cutoff-limited capacity than [68]. As for capacity per core, that of [68] is only comparable to that of these 6-core C+L-band fibres.

The average of the cutoff-limited capacity per core in the fibres designed in this chapter can be compared with that of the Corning Ultra-low Loss (ULL) SMF28 as illustrated in Fig. 5.9(d). 6-core fibres have similar capacity per core to the SMF28 with very small decrease due to the A_{eff} and XT. The 7-core fibre in [68] has a much smaller cutoff-limited capacity per core compared to the SMF28 when it is limited to S+C+L band.

According to the analysis and discussion above about various capacity metrics, the O+E+S+C+L-band 6-core fibre has the highest total capacity. But in the practical applications, it might face the lack of amplifiers in O-Band and E-band as well as low transceiver efficiency. If people want to apply the fibre without any concern about the

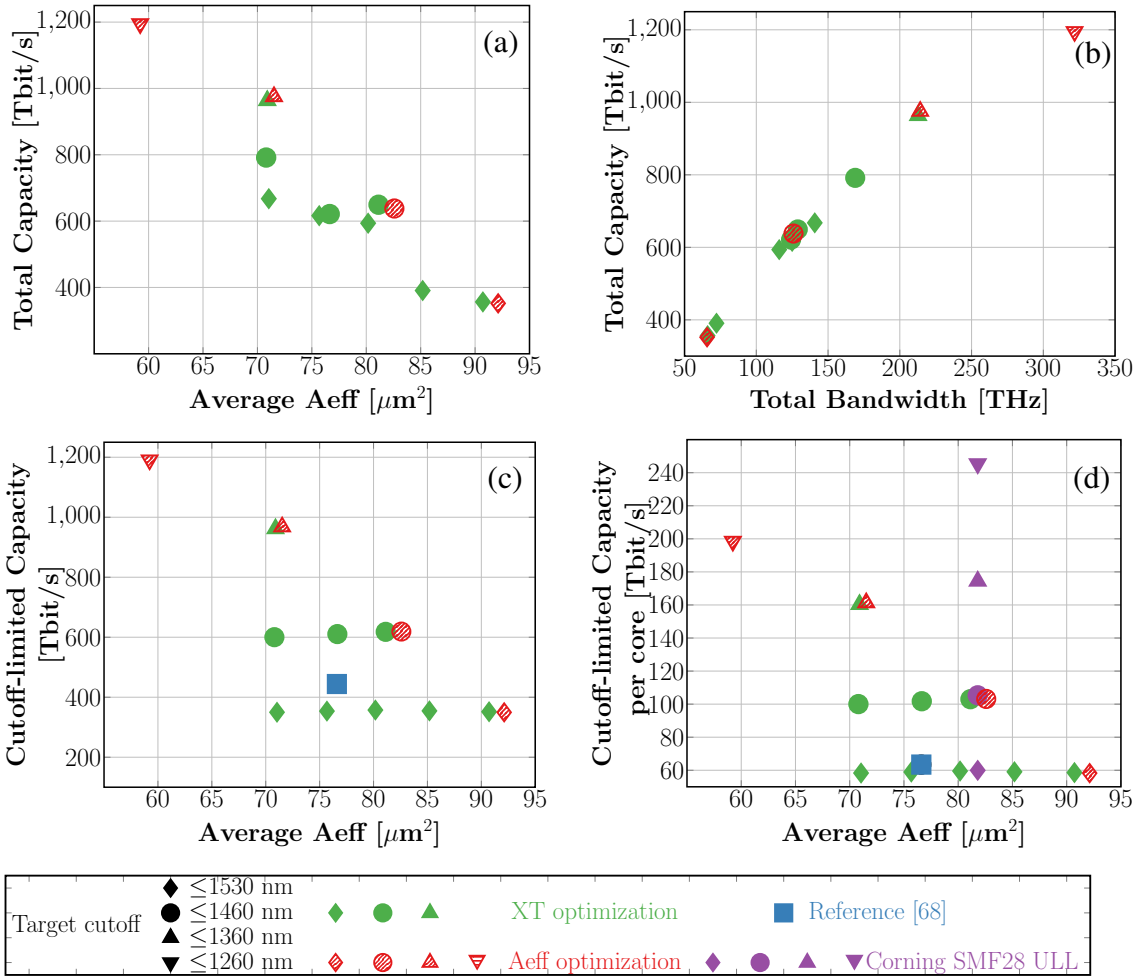

Fig. 5.9: (a) Total capacity of all the optimised MCFs calculated over the whole bandwidth of each fibre versus the A_{eff}; (b) Total capacity versus the total bandwidth of the MCF; (c) Cutoff-limited Capacity calculated when bandwidths are limited in the optical bands for 1200 km transmission; (d) Cutoff-limited capacity in (c) averaged by core number for 1200 km transmission.

amplifier, the 1460 nm fibres can be the one which covers S+C+L bands and has good capacity simultaneously. If the application highly depends on the A_{eff}, then the A_{eff}-optimised 6-core fibre with 1530 nm cutoff wavelength will be the best choice.

The transmission length was elongated to 6000 km with 60 km/span for exploring 6-core fibres' capacity in transoceanic transmission. The three *A_{eff}-optimisation* results with different optical bands were picked to be compared for two transmission lengths. For 1200 km transmission, O+E+S+C+L-band fibre holds a cutoff-limited capacity up to ∼1.2 Pbit/s while for 6000 km, it is 409.7 Tbit/s with a 65.6% drop. Fibres with narrower bandwidth have smaller drop, 46.1%, 39.0% and 35.2% for E+S+C+L-, S+C+L- and C+L-band fibres, respectively, as illustrated in Fig. 5.10(a). This is because the narrower the fibre bandwidth the larger A_{eff} and XT. To some extent, the benefit of A_{eff} compensates for the XT penalty increase due to the transmission length

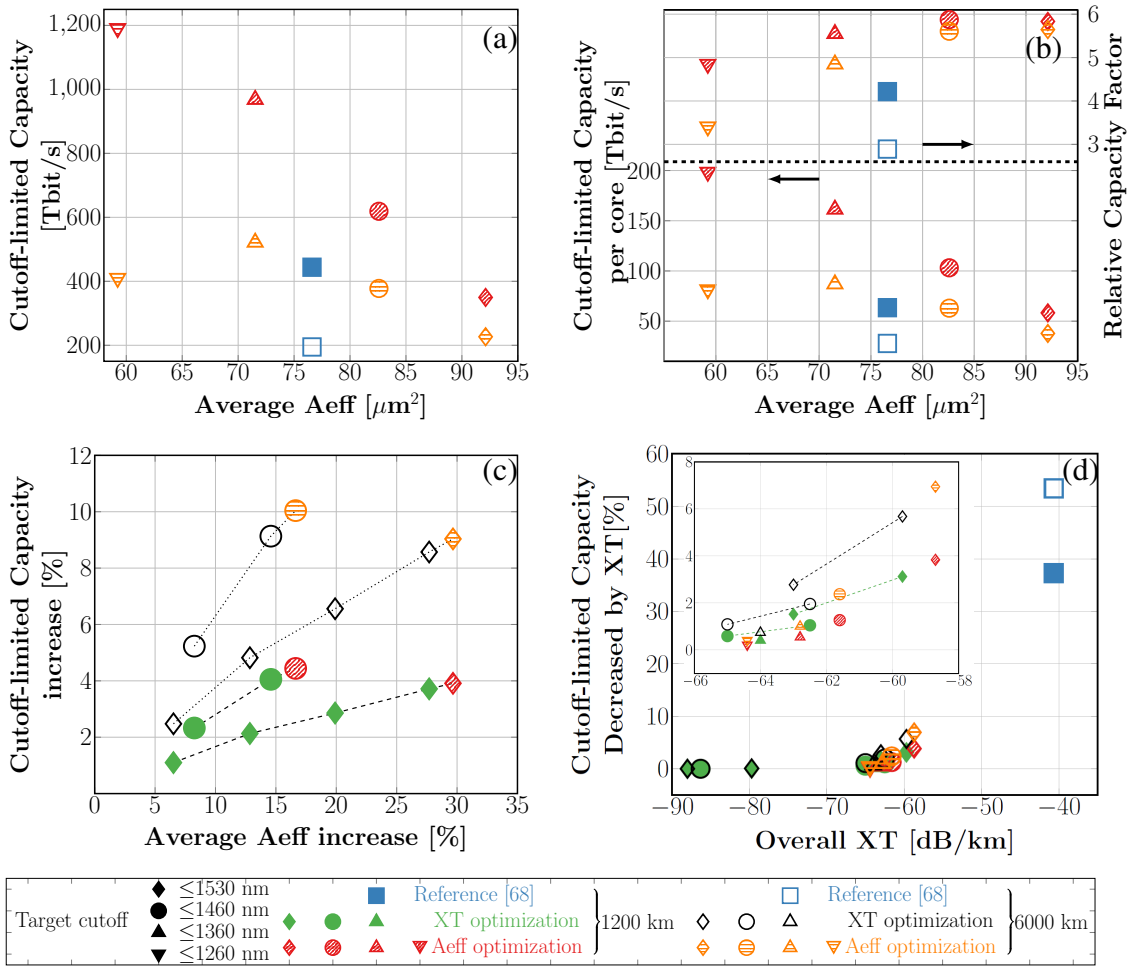

Fig. 5.10: (a) Cutoff-limited capacity of A_{eff}-*optimisation* results for two transmission lengths; (b) Cutoff-limited capacity per core and relative capacity factor comparison between 1200 km and 6000 km transmission ; (c) The benefit of A_{eff} increase to cutoff-limited capacity; (d) The penalty that cutoff-limited capacity suffers from XT.

elongation in the fibre with a narrower bandwidth. For 6000 km transmission, due to the large capacity drop of O+E+S+C+L-band MCF, E+S+C+L-band fibre has the highest capacity, 521.8 Tbit/s. The cutoff-limited capacity of [68] is further degraded while the transmission length increases to 6000 km because of poor SNR. This S+C+L-band fibre has around 84.8% more cutoff-limited capacity.

By normalizing their cutoff-limited capacity per core with the SMF28 capacity in Fig. 5.9 which is calculated with the same bandwidth and transmission length to the MCFs, the ratio is noted as a Relative Capacity Factor (RCF) shown in Fig. 5.10(b). O+E+S+C+L-band fibre has around 20 μm^2 smaller A_{eff} than the ULL SMF . Thus, it has smaller RCF, 4.8 and 3.4 for 1200 km and 6000 km transmission, respectively. The others are slightly smaller than 6 due to XT penalty. In other words, the optimised 6-core fibres have comparable capacity per core to the SMF28. Moreover [68] is a 7-core fibre, its cutoff-limited capacity per core is lower than that of these 6-core fibres, and

therefore, its RCF is 4.2 and 2.9 for 1200 km and 6000 km transmission, respectively.

Under these two transmission lengths, we investigate the impacts of A_{eff} and XT on the capacity performance separately. Firstly, the cutoff-limited capacity without considering XT increases slowly with the average A_{eff}. To analyse further their relationship, we calculated the increment in percentage by comparing the difference between the data of each point to the one which has the lowest average A_{eff} and smallest capacity. A 5-30% increase of A_{eff} leads to just a 1-4.5% increase in total capacity for 1200 km transmission. When the transmission is up to 6000 km, the same increment of A_{eff} results in around double the percentage increase in cutoff-limited capacity as illustrated in Fig. 5.10(c).

When taking XT into the SNR calculation, the cutoff-limited capacity is reduced. The XT penalty on cutoff-limited capacity increases with XT. When XT increases from $\sim$-65 dB/km to $\sim$-59 dB/km, the penalty increases from around 1% up to 7% as illustrated in the zoom-in Fig. 5.10(d). The longer the transmission length, the higher the accumulated XT and therefore the more reduction of the cutoff-limited capacity. Since the optimised MCFs all have ultra-low XT, the benefit of A_{eff} is offset by the penalty due to XT, and therefore the cutoff-limited capacity in Fig. 5.9(d) is similar for the same optical bands. But in the higher XT region, XT will have a non-negligible penalty in the capacity of the reference point shows.

5.8 Summary

In this chapter, an automated MCF design method based on the PSO algorithm has been proposed to optimise MCF optical properties and capacity. The MCFs design is simplified to optimise the neighbouring core pair taking advantage of the symmetry and heterogeneous MCF structure. In this work, the MCF design took all the refractive-index profile parameters as variables for the first time to search for the optimised MCF structure. The AI-based method can design MCFs with multi-objective functions and different constraints autonomously and efficiently compared to the brute force methods with ten orders of magnitude reduction of permutation evaluations. Meanwhile, by using the statistical classifier and regressor to estimate the CLinstead of an FDE solver, the computation time is reduced by six orders of magnitude.

Taking the minimization of XT as the main purpose, the PSO-designed MCFs have achieved with ultra-low XT from -92.1 dB/km to -58.7 dB/km, covering up to E+S+C+L band, which is comparable to or much lower than the lowest XT in the literature, -65.1 dB/km. However, it should be noticed here that the comparison is made between the design and the fabricated fibres. After the fabrication and during the measurement, the overall XT might be degraded. Thus, the XT performance of the designed fibres should be checked with the fabrication and measurement experiments.

When taking the maximization of A_{eff} as the main purpose, an RCMF of 6.82 was obtained for a 6-core fibre which is better than the 6.7 achieved in the literature. The successful designs with two objective functions demonstrate the reliability of the automated AI method to realize the multi-dimensional MCF design problem and its ability to optimise different MCF optical properties.

With ISRS GN model, the SNR and capacity performance can be checked upon MCF designing. By investigating the relationships among the optical properties of PSO-designed MCFs and the SNR and capacity, it can be concluded that the bandwidth dominates the capacity performance. A_{eff} increase brings almost linear cutoff-limited capacity increase without XT influence while XT results in an exponential-increasing penalty to cutoff-limited capacity. PSO-designed MCFs have similar capacity per core for the S+C+L-band and C+L-band fibres compared with the Corning ULL SMF28 (RCF approaching 6) in both 1200 km and 6000 km transmission. The E+S+C+L-band fibre results in a total capacity of $\sim$1 Pbit/s for 1200 km transmission and $\sim$500 Tbit/s for 6000 km transmission. The O+E+S+C+L-band fibre delivers up to $\sim$1.2 Pbit/s for 1200 km transmission and RCF approaching 5.

Compared with the 7-core fibre in [68], the optimised fibres have 35.1% and 84.8% more capacity considering the S+C+L optical bands, respectively, for 1200 km and 6000 km transmission. From the above, it can be concluded that the proposed AI-based MCF design method, with capacity-check post-process, is a promising tool-set for the design of future MCFs with single-ring or double-ring structure in the same or wider cladding diameter for the purpose of controlling or optimising XT, A_{eff}, cutoff wavelength or other optical property requirements.

Chapter 6

Design of 6-core and 8-core multi-core fibre with coating loss and cutoff wavelength ML tools

6.1 Associated publications and contributions

The main part of this chapter is taken from the paper below where the author of this thesis was the primary contributor.

Mu, X., Ottino, A., Ferreira, F. M. and Zervas, G. Design and transmission analysis of TA multi-core fibre in standard cladding diameter. Opt. Express 30, 38152–38166 (2022).

- Primary author;
- Lead researcher.

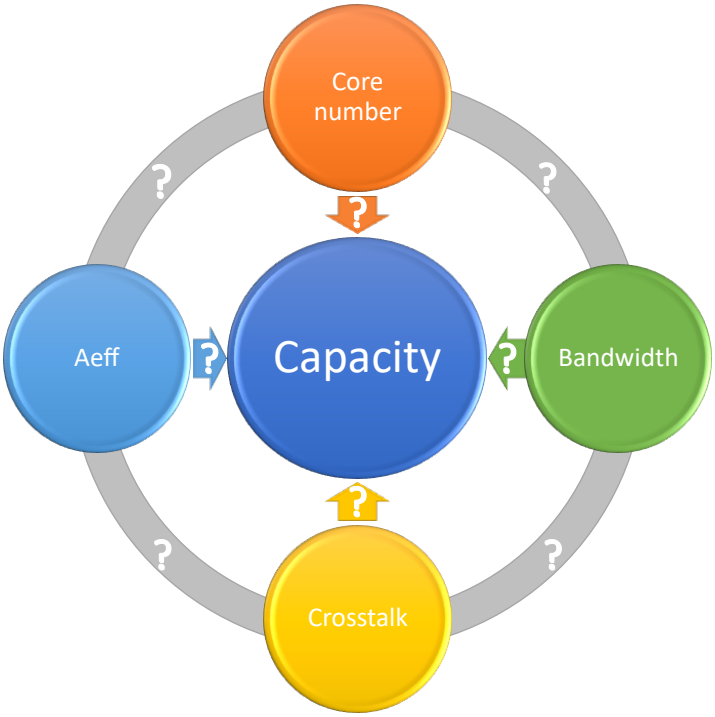

Fig. 6.1: Visualising the problem described in this chapter. How do these properties influence the MCF capacity? How do they mutually influence?

6.2 Chapter summary

A high-level summary of the problem/motivations, proposed solution, and outcomes, as related to this chapter, is:

- Problem: in the MCF design process, multiple properties need to be controlled, such as core density, bandwidth and A_{eff} of the fibre core, and XT, as illustrated in Fig. 6.1. These properties all have an influence on the MCF capacity and influence each other at the same time. Thus, how do these properties influence the MCF capacity? Which should be paid more attention to when the MCFs are designed?

- Proposed solution: the method mentioned in the previous chapter is further developed to include the regressors for both coating loss and cut-off wavelength. Then it is used to design 6-core and 8-core fibres in standard cladding diameter at various property-constraints cases. By thoroughly analyzing the structure, optical properties and transmission capacity of the optimised MCFs, the mutual relationship between the properties shown in Fig. 6.1 and their effects on the capacity are explored.

- Outcomes:

  - Apart from using the coating-loss regressor and classifier, a new cutoff-wavelength regressor is shown in the section. 4.1.2.2 is trained considering the unique loss behaviour of the trench-assisted fibre core. It provides fast and accurate cutoff wavelength prediction in the optimisation process.

  - Low-XT 6-core and 8-core fibres covering CL- and SCL- bands are designed by the proposed AI-based techniques. By investigating the index profiles of optimised MCFs, the search space can be shrunken to reduce the design workload.

  - The AI-design method delivers an 8-core fibre design that can offer notable capacity improvement, around 32% (approaching the theoretical 33.3%) for 50 km transmission compared to the 6-core fibre design. However, the 8-core fibre has a higher capacity degradation rate over distance leading to a similar performance at 10000 km.

  - Higher core density limits the bandwidth and A_{eff} and also results in higher XT. A_{eff} increment has a similar effect on 6-core and 8-core fibre. However, XT change results in different behaviour of capacity over transmission distance in these two cases.

6.3 Introduction

In the above chapter, the AI-based automatic method was proposed to design 6-core TA MCFs in standard cladding diameter. This chapter is an extension of the method to include a new cutoff wavelength regressor and then optimise both 6-core and 8-core fibres. Based on the optimised fibres, the impact of optical properties and core number on the capacity was investigated.

The existing uncoupled MCFs in standard cladding diameter have 4 cores [159, 160] to 8 cores [33, 75, 106, 161]. In [33], the authors present the only fabricated 8-core fibre supporting only O-band. As for other 8-core fibre designs based only on simulation, there are the fibres in [161] designed to support O-band and those in [75] supporting wide-band (cutoff wavelength = 1300 nm) lack the critical analysis of the coating loss - particularly relevant for high-index coating [30]. Based on the estimations, the coating loss of the fibre cores reported ranges from 0.067 dB/km to 1.15 dB/km which makes them unsuitable. Recently, [106] reported an 8-core fibre design optimised to keep coating loss smaller than 0.01 dB/km but covering only the C-band.

Previous works [28, 75, 84] reporting the design of TA MCFs ignored the unique loss behaviour of TA fibre core reported in [22]. Instead, they treated TA profiles the same as step-index ones, which leads to significant cutoff wavelength miscalculation. To address the shortcomings of the prior art, Lumerical was used to estimate the cutoff wavelength of 10,000 TA fibre core profiles by calculating the TA fibre core's LP11 loss at straight conditions. The data were used to train a machine learning regressor to speed up the design process by around $10^7\times$.

On the other hand, the optimisation of 6-core and 8-core fibres covering C+L- and S+C+L- bands were reported under coating loss constraint — smaller than 0.001 dB/km while optimising the inter-core XT or effective mode area (A_{eff}). Inter-core XT is one of the key metrics in the design of weakly-coupled MCF. When the spatial density is increased, the core pitch is reduced leading to higher inter-core XT. However, for a given pitch, it has been shown that inter-core XT can be reduced by making neighbour cores heterogeneous [73]. Therefore, the fibre assumes that there are two types of cores neighbouring each other for controlling the XT level. On the other hand, A_{eff} influences the NLI noise in transmission and it is a performance metric of MCF when compared to the SSMF.

Moreover, following the fibre design process, their capacity is evaluated. Transmission performance for distances between 50 km to 10000 km is obtained utilising a GN model. Given the ultra-wide bandwidth of the designs proposed, the transmission model includes ISRS [55]. The relationships between capacity and the optical properties (bandwidth, A_{eff} and XT) of the MCFs are thoroughly analysed. The influence brought by adding two more cores into the standard cladding diameter on the

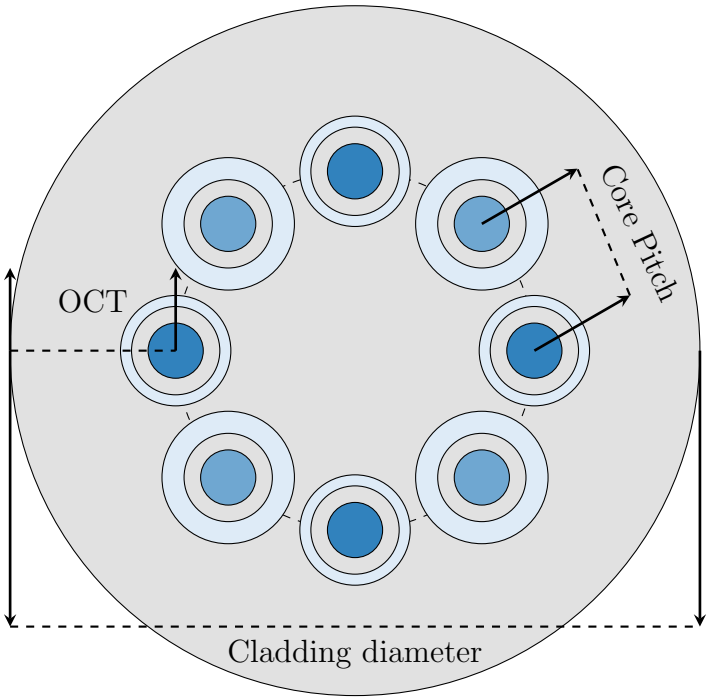

Fig. 6.2: 8-core trench-assisted fibre schematic diagram.

fibre core structures and the optical properties is investigated.

6.4 Design methodology

This work assumes that there are two types of cores alternated in a ring — the effective index difference between neighbour cores reduces the inter-core XT. The schematic diagram of the 8-core TA fibre design optimised here is illustrated in Fig. 6.2. The core pitch of 32.5 μm for 6-core fibres and 24.87 μm for 8-core fibres respectively, OCT of 30 μm (for reducing coating loss) [39] and a cladding diameter of 125 μm are set in the fibre design. The other parameters assumptions are the same as Section 5.4

In the PSO algorithm [1], each particle contains these 10 variables which represent an MCF structure. The particles search the optimal fibre structure according to their corresponding fitness values. In the fitness value calculation, the overlap condition and the coating loss condition are checked as the first step for all the optimisations:

- Overlap condition: the distance between the adjacent trench edges must be $\geq$ 2 μm for preventing superposition;
- Coating loss condition: the coating loss must be $\leq$ 0.001 dB/km.

If and only if both conditions are satisfied, the fitness values are calculated based on two different objectives: maximise-A_{eff} (A_{eff}*-optimisation*) or minimise-XT while constraining A_{eff} (XT*-optimisation*). Exploring two objectives is key to the whole

design process as the performance of meta-heuristics and in turn, the generated fibre structure significantly relies on the analytical formulation of the objective functions. The two types of cores have different A_{eff} since MCF is heterogeneous. Herein the maximum of the average A_{eff} of the two types of cores was explored.

The design process starts with the most challenging widest bandwidth requirement using the maximise-A_{eff} objective. The process of going through the constrained combinations of 8-core fibres is illustrated in Fig. 6.3 as an example. The PSO cannot find solutions satisfying all the constraints for the first two cases—OESCL band and ESCL band. That means that an 8-core fibre cannot be designed to support OESCL or ESCL bands. The design process moves to the S+C+L band bandwidth requirement. The maximum average A_{eff} is found to be 60.28 μm^2. Following this, the design process carries on with the second objective function that aims to minimise-XT while constraining the A_{eff} of the two types of cores within [60 70] range. Again, it is impossible to find a solution in which the A_{eff} is above 60 for both types of cores simultaneously. Then, the A_{eff} constraint is reduced to [55 65] and [50 60]. The design process is repeated under the C+L bandwidth constraint.

In the 6-core fibre case, the maximum average A_{eff} is found to be 64.41 μm^2 for S+C+L band and 73.65 μm^2 for C+L band. Fibres are designed in XT-optimisation for S+C+L band for A_{eff} from [70 80] to [50 60] and for C+L band for A_{eff} of [60 70] and [55 65]. The details about designing the objective functions including all the constraints are shown in [1].

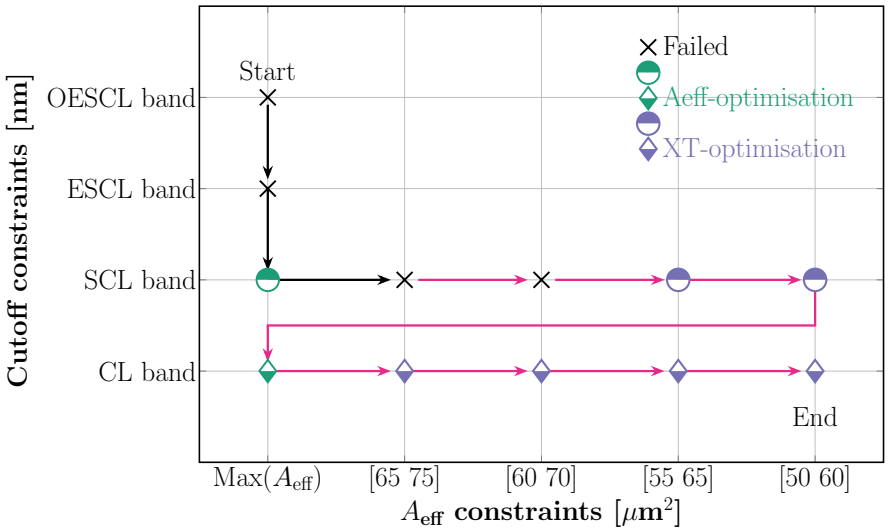

Fig. 6.3: Optimisation process to go through combinations of constraints taking 8-core fibre as an example. The green marks are for *A_{eff}-optimisation* and the blue marks are for *XT-optimisation*. The circle marks represent the S+C+L band fibres and the diamond marks stand for the C+L band fibres. The representation of mark colour and shape to the optical band is valid for all the following figures.

Particles optimise the MCF structure based on the fitness value. For each design

point, there are only up to 10^6 evaluations to converge which is nine orders of magnitude less than the brute force method ($\sim 10^{15}$). Then, the optimised MCF structure is extracted for each constraint combination. The flowchart, Fig. 4.13 in Section 4.2, shows the PSO process.

6.5 Performance evaluation of fibre designs

6.5.1 Fibre design analysis

After going through all the combinations of cutoff wavelength and A_{eff} constraints, 9 designs of 6-core fibres and 8 designs of 8-core fibres are obtained. Solid and half marks are used to represent 6-core fibres and 8-core fibres respectively in Fig. 6.4.

The optimised fibres are compared to MCFs previously presented in the literature [68, 70, 71, 72, 159], with standard cladding diameter, in terms of XT and RCMF [1]. RCMF is most useful to understand how the A_{eff} of cores in the MCF is against an SSMF and to make comparisons among MCFs with different core numbers.

6-core fibres in XT-optimisation have ultra-low XT less than -80 dB/km while the two designs in A_{eff}-optimisation have XT around -60 dB/km which is more than 20 dB/km higher. That is due to both their higher RCMFs and the homogeneous structures. Our 6-core fibres have RCMF from 4.23 to 5.52. Compared to the reference fibres shown as black square marks, the A_{eff}-optimisation 6-core fibres have up to 1.25 higher RCMF than the 4- and 5-core fibres [71, 72, 159] while more than 5 dB lower XT than the 6-core fibre [70].

The 8-core fibres have higher core density, which generally leads to higher XT. Most of them are between -45 dB/km and -60 dB/km except for the two results of A_{eff}-optimisation and the [65 75] case for the C+L band. The two in A_{eff}-optimisation are heterogeneous but their high RCMFs result in high XT. As for the latter one, it has a similar RCMF to that of the A_{eff}-optimisation but a homogeneous structure. Thus, it holds the highest XT. Compared to the 6-core [70] and 7-core [34, 68] fibres in Fig. 6.4, it can be seen that most of our 8-core fibre designs have similar XT, even smaller XT. Meanwhile, the new 8-core fibres have comparable RCMFs to that of the 6-core and 7-core fibres — between 5.42 and 6.50. As for 8-core fibre in [106], its A_{eff} is 80 μm^2 (the corresponding RCMF is 8), however, it has a higher XT than -30 dB/km, which is not suitable for long-haul transmission. It is worth noting here that this 8-core fibre is just a design which is not yet fabricated. The XT shown in Fig. 6.4 is calculated based on the core-to-core XT provided by [106]. Compared to it, our 8-core fibres have up to 35 dB lower XT.

To explore the fibre structures' difference between two core numbers, the refractive-index profile parameters' range in the final designs are illustrated in Fig. 6.5. The search area is reduced apparently. The total permutation number reduces by 991$\times$ for the 6-

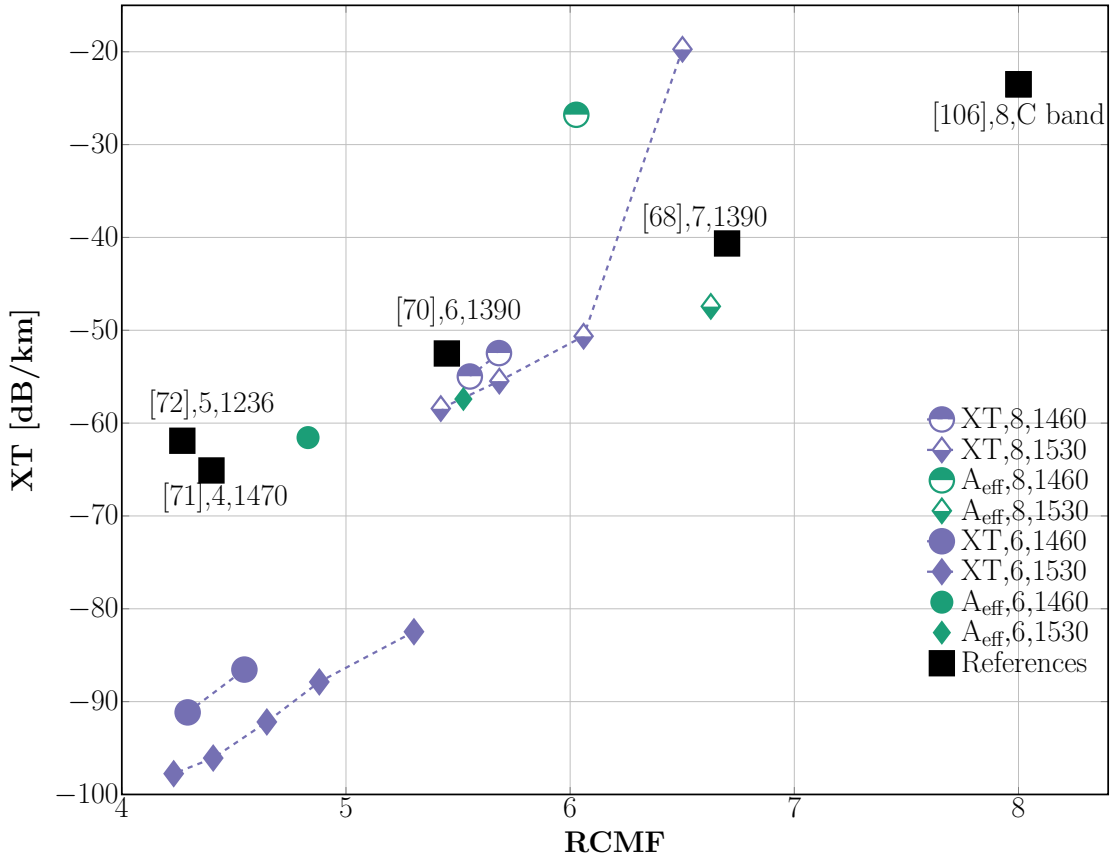

Fig. 6.4: XT and RCMF of the MCFs. Next to the square marks show the reference, core number and cutoff wavelength in nm. As for the legend, next to the marks show the design objective (XT or A_{eff}), core number (6 or 8) and cutoff wavelength constraint (1460 or 1530).

core case and 3.6e5× for the 8-core case. The permutation number is reduced more for 8-core fibres because the compact fibre structure limits the fibre structure.

a_1 and Δ_1 play the role of meeting the constraints of cutoff wavelength and A_{eff}. In both cases, their range can be reduced to half-width. In the 6-core fibre designs, w_{tr} converges to a very narrow region close to the widest while w_{cl} lays at the narrow side. In the 8-core fibres, although the trench is the deepest, the w_{tr} operates within a broader range because of the smaller core pitch and the overlap condition. w_{cl} converges to the narrowest layer width. Compared to the 6-core fibres, Δ_1 of the 8-core fibres is slightly higher. With the narrower w_{tr}, fibre cores need a higher index difference to compensate for the light confinement for preventing exceeding coating loss constraint. The key conclusion here is that the trench can be fixed to be deep while having the small w_{cl}. Should there be ample space/core pitch, the trench can also be fixed to the widest. This can simplify and speed up the MCF design by just optimising the a_1 and Δ_1. This can be particularly valuable when designing MCFs with large core numbers across larger cross-sectional areas.

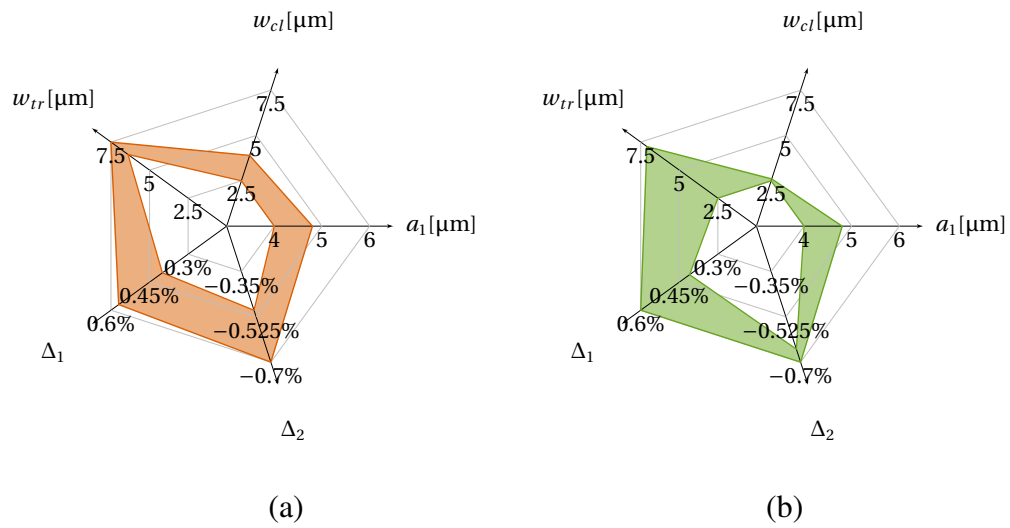

Fig. 6.5: Refractive-index profile parameters' range of (a) the 6-core fibres and (b) the 8-core fibres.

6.5.2 Transmission performance

We explore the capacity of the MCFs from 50 km to 10000 km transmission length and analyse the effects of the optical properties on the capacity in this section.

The capacity calculation assumes Gaussian modulation, uniform launch power -2 dBm/channel, bandwidth 49.5 GHz/channel with 50 GHz channel spacing and 50 km per span. The assumptions on the fibre attenuation of the SSMF and MCFs and the Noise Figure (NF) across the spectrum used in the capacity calculation are in Fig. 6.6.

The attenuation calculation is described in Section 2.2.5. The MCFs' attenuation is higher than that of the SSMF because of the higher core index as shown in Fig. 6.5. Similarly, the 6-core fibres have slightly higher attenuation than the 8-core fibres.

The 6-core and 8-core fibre with the best capacity were picked for CL- and SCL-band respectively. The properties of these four fibres are shown in Table 6.1. Different from the case of the 6-core fibres—the fibres with the highest capacity are close to the larger A_{eff} side and the fibre with the lower XT offers the optimum capacity among the 8-core fibres. The influence of A_{eff} and XT on capacity will be elaborated respectively later.

There are several factors influencing SNR performance. Here they are shown separately in Fig. 6.7. The TRX is assumed to be 23 dB The XT, ASE and NLI increase with the transmission length. The XT is worse for the longer wavelength and thus, the gap between the SNR without XT and SNR becomes wider with the increasing wavelength.

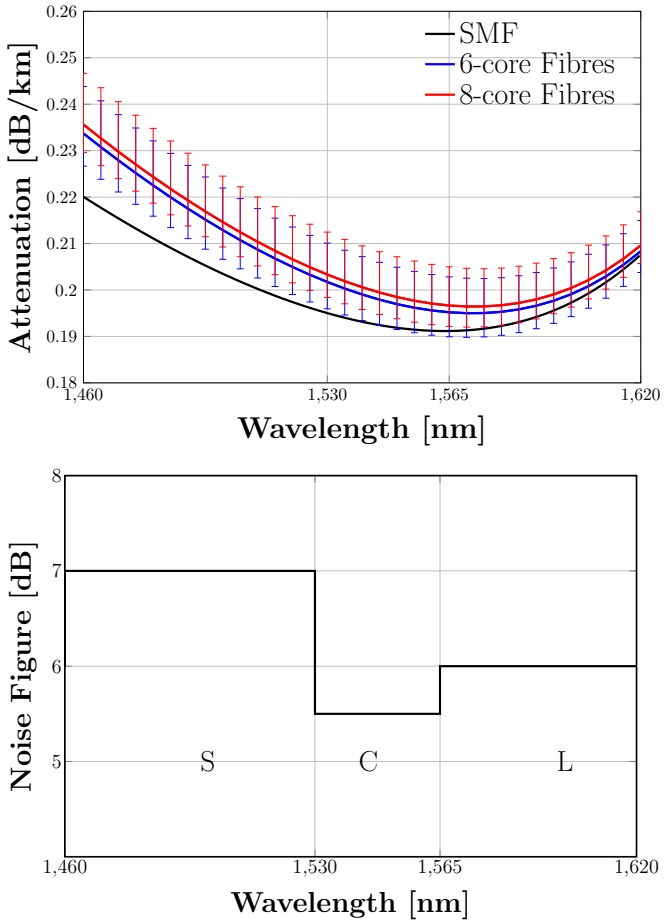

Fig. 6.6: The assumption of attenuation (a) and noise figure (b).

Table 6.1: The n_{eff}, A_{eff} and CD at 1550 nm for 6-core and 8-core fibre design shown in Fig. 6.8

Case name	Constraints	n_{eff} core1/core2	A_{eff} [μm^2] core1/core2	CD [ps/km/nm] core1/core2
6core-CL	XT-optimisation [70 80]	1.44695/1.44782	71.12/70.07	23.84/23.52
6core-SCL	A_{eff}-optimisation	1.44707/1.44707	64.41/64.41	23.51/23.51
8core-CL	XT-optimisation [55 65]	1.44738/1.44888	57.26/56.42	23.05/23.16
8core-SCL	XT-optimisation [55 65]	1.44726/1.44838	57.69/55.96	23.07/23.00

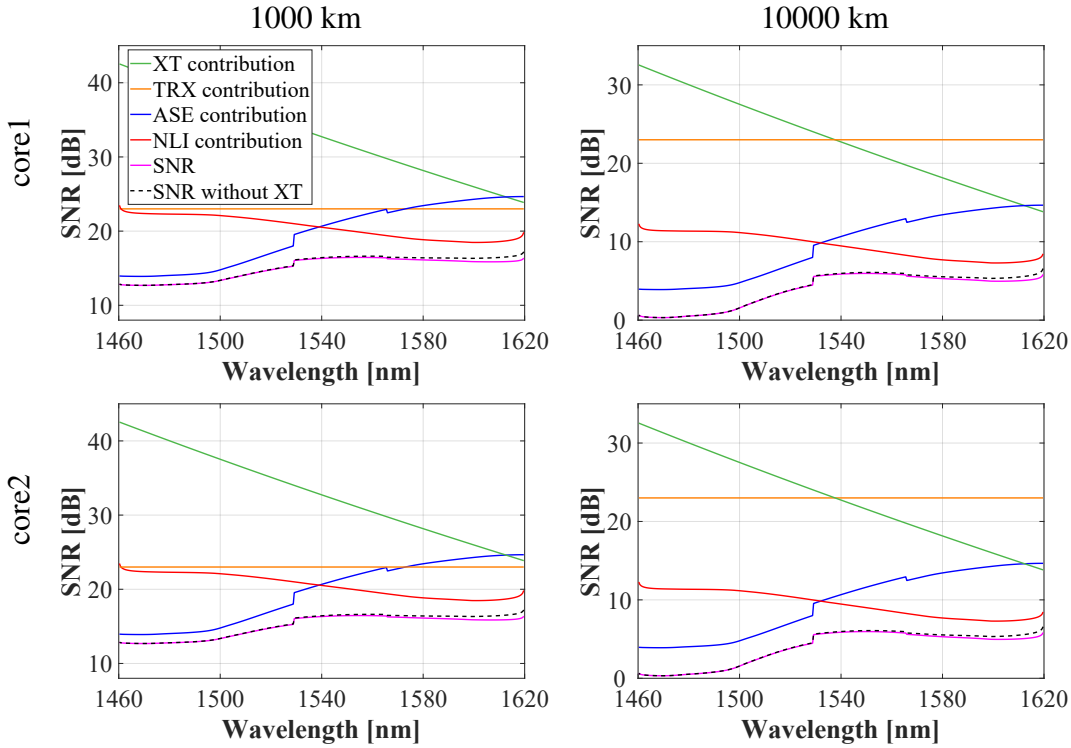

Fig. 6.7: SNR and its contributions including crosstalk (XT), transceiver (TRX), amplified spontaneous emission (ASE) and nonlinear interference (NLI) of two types of cores in SCL-band 6-core fibre.

The full-band capacity is calculated while considering all the optical bands the MCFs can cover as shown in Fig. 6.8. The SCL-band 8-core fibre provides the highest capacity at 50 km (1157.97 Tbit/s) while the SCL-band 6-core fibre delivers 879.71 Tbit/s. The 8-core fibre holds 31.63% higher capacity than the 6-core fibre while in the CL-band case, the 8-core fibre has 31.96% higher capacity. Both are very close to the 33.33% spatial density increase. At 50 km, the influence brought by XT is negligible. The small margin to the ideal case is due to the smaller A_{eff} of the 8-core fibre compared to the 6-core fibre.

As the transmission length increases, the capacity drops because of the accumulated noise. The capacity of 8-core fibres remains above that of 6-core fibres. The capacity of the 8-core fibre keeps reducing at a faster pace than the 6-core fibre since the 8-core fibre has higher XT (27.04 dB for CL-band and 9.1 dB for SCL-band) and smaller A_{eff} (13.87 μm^2 for CL-band and 7.58 μm^2 for SCL-band). At 10000 km, the total capacity of the SCL-band 8-core fibre is 6.82% more compared to the SCL-band 6-core fibre. Meanwhile, the total capacity of the CL-band 8-core fibre is 7.97% more than that of the CL-band 6-core fibre.

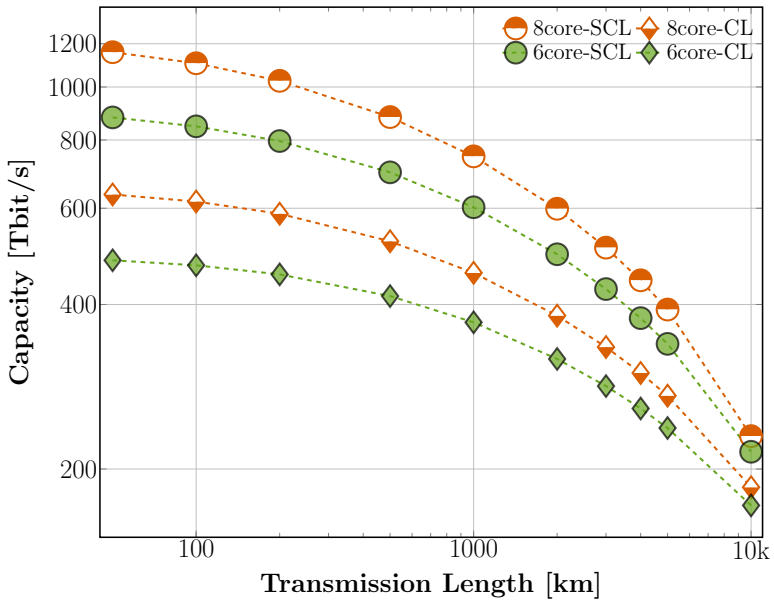

Fig. 6.8: Capacity of the MCFs for from 50 km to 10000 km transmission

6.5.3 Investigation of optical properties' influence on capacity

In the following discussion, the influence of the bandwidth, A_{eff} and XT on the transmission performance was analysed. Firstly, in order to further investigate the MCF transmission performance dependence on the bandwidth, the metric of spatial-spectral efficiency is used here in Fig. 6.9. Spatial spectral efficiency (SSE) is defined as the spectral efficiency per cladding area of the SSMF [3]. Herein since the MCFs are designed in the standard cladding diameter, Spectral-spatial efficiency (SSE) equals the spectral efficiency per fibre which is easily compared with the SSMF. There are several factors leading to the spectral efficiency degradation in ultra-wideband optical fibre transmission systems:

- The ISRS-induced penalty increases with an increase in the channel number;
- The attenuation is higher out of the C band, especially at short wavelengths;
- The A_{eff} is smaller at the short wavelengths, which brings more non-linearity into the wide-band capacity;
- In the MCF case, the XT increases with a longer wavelength;
- The optical components have different performances across the entire bandwidth. For example, the NF in S band is higher than in C band.

The relationship between SSE and bandwidth per core is depicted in Fig. 6.9 from C band to full band in two transmission lengths, 1000 km and 10000 km. First of all, the SSE keeps almost the same when the operation changes from C band only to CL-band. That means that expanding the transmission into C+L-band would benefit from

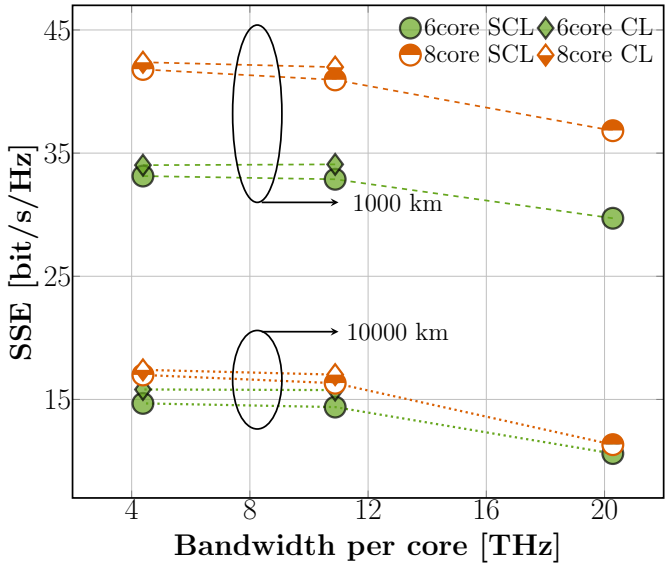

Fig. 6.9: Spatial spectral efficiency for different bands (C, CL, SCL from left to right) at 1000 km and at 10000 km.

the wider bandwidth without apparent SSE degradation. At 1000 km, the 8-core fibre has 42.38 bit/s/Hz SSE while operating only in C-band, about 8.36 bit/s/Hz higher than the 6-core fibres. When it comes to 10000 km, the SSE of the 8-core fibre falls by around 34.98 bit/s/Hz while that of the 6-core fibres decreases by about 18.22 bit/s/Hz. Thus, the SSE of 8-core fibre at 10000 km is similar to that of the 6-core fibre.

The SSE of the 8-core fibre decreases faster than that of the 6-core fibres when the bandwidth is increased from CL-band to SCL-band. The relatively high XT, high attenuation and small A_{eff} of the 8-core fibre lead to this fast drop. This drop makes the SSE of SCL-band 8-core and 6-core fibre closer, resulting in a smaller capacity increase in the SCL-band case compared to the CL-band case in the total capacity at 10000 km.

Furthermore, the capacity sensitivity on A_{eff} and XT are analysed. Higher A_{eff} corresponds to lower nonlinear effects, which leads to higher capacity. The capacity increase brought by A_{eff} increases in the rate of capacity increment compared to the 6-core or 8-core fibre that has the smallest A_{eff}. Here the capacity is calculated with SNR_0 for eliminating the XT influence.

As for 6-core fibres, the A_{eff} increases up to 30.54% for CL-band fibre and 12.51% for SCL-band fibre illustrated in Fig. 6.10(a). It leads to up to a 6.10% capacity increase for 1000 km and up to a 23.14% increase for 10000 km. The A_{eff} increase has about four times the benefit for 10000 km compared to the 1000 km case. Meanwhile, the SCL-band fibre benefits the same as the CL-band fibre with half the A_{eff} increase. In the 8-core case in Fig. 6.10(b), the highest A_{eff} increase is 8.33% smaller than that in the 6-core case. The corresponding capacity increase is 4.81% and 16.60% for 1000 km and 10000 km respectively. The ratio between capacity increase and A_{eff} increase is similar in both cases.

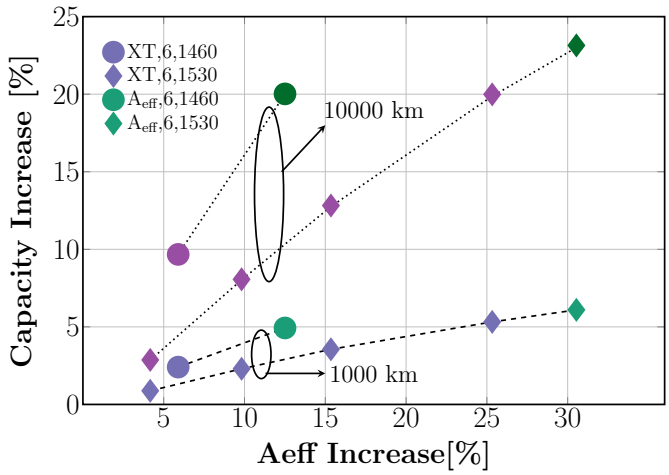

(a)

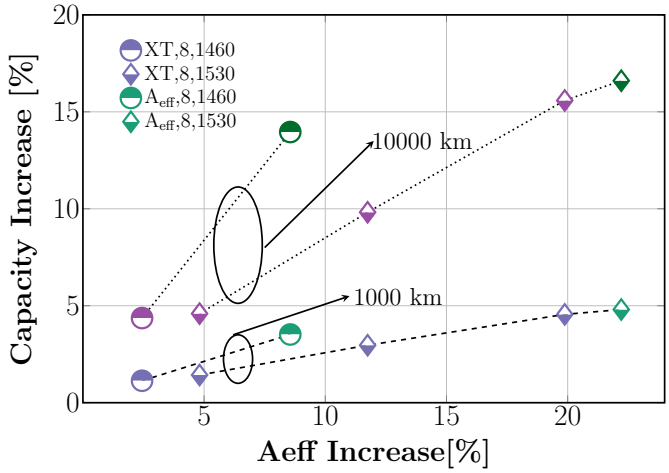

(b)

Fig. 6.10: Capacity increases with A_{eff} increase:(a) 6-core fibres; (b) 8-core fibres.

Since XT is included in the SNR calculation as noise in Eq. 2.101, by comparing the capacity calculated with SNR and SNR_{XT}, the capacity penalty induced by the XT noise can be calculated.

$$C(SNR) = \sum_{j}^{N_c} \sum_{i}^{N} B_{ch} \cdot log_2(1 + SNR_i), \tag{6.1}$$

$$Penalty = \frac{C(SNR) - C(SNR_{XT})}{C(SNR)}, \tag{6.2}$$

in which N_c is the number of cores in the MCF, N is the total number of wavelength channels in each core and B_{ch} is the bandwidth of each channel.

As illustrated in Fig. 6.11, the XT-induced penalty increases super-linearly with the XT. For 6-core fibres of which the XT is below -80 dB/km, the capacity penalty is ultra-low and close to zeros in both 1000 km and 10000 km transmission. The marks

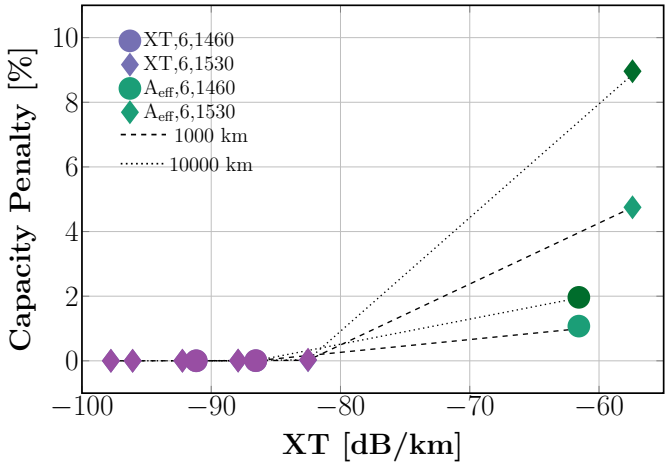

(a)

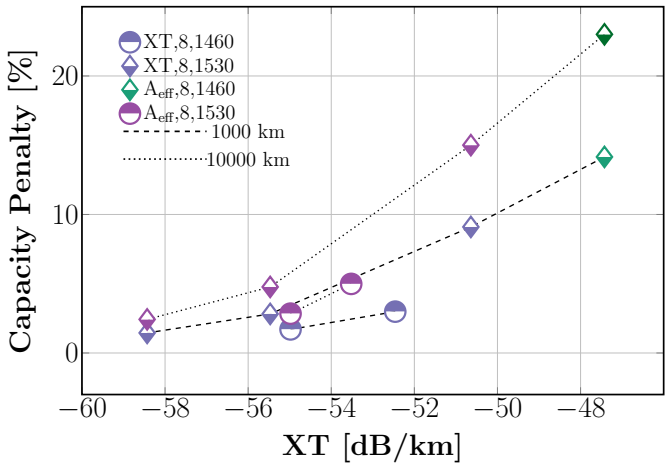

(b)

Fig. 6.11: The XT-induced capacity penalty as a function of the XT at 1550 nm: (a) 6-core fibres; (b) 8-core fibres.

with darker colours are the results at 10000 km. Those 6-core fibres obtained in A_{eff}-optimisation have XT close to -60 dB/km and the influence due to XT starts to show up but stays below 10%. The CL-band fibres suffer more penalty than the SCL-band fibres because the XT is smaller at a short wavelength. At S band, with the shorter wavelength, the XT becomes smaller. Thus, it brings less penalty than in the CL-bands. When the transmission length increases from 1000 km to 10000 km, XT would be 10 dB higher which leads to a double capacity penalty.

Since it focuses on the capacity at 1000 km and 10000 km, the MCFs which have XT higher than -30 dB/km and -40 dB/km are not suitable. Thus, in Fig. 6.11(b), only part of the 8-core fibres are illustrated. 8-core fibres have higher XT and therefore the penalty is up to 14.15% for 1000 km while it is up to 23.01% for 10000 km. Here it can be seen that the penalty increases due to the longer transmission length becoming higher with increasing XT.

Among the 6-core fibres, the penalty induced by XT is much lower than the benefit from the A_{eff} increase. Thus, large-A_{eff} 6-core fibre has better transmission performance. On the other hand, for 8-core fibres, the XT-induced capacity penalty is slightly higher than the capacity increase brought by the A_{eff} increase. Therefore, the 8-core fibres with smaller XT have better capacity.

6.6 Summary

Within this chapter, 6-core and 8-core fibres covering CL- and SCL-band were designed by the AI-based automated method with a cutoff wavelength regressor for the TA fibre core. The MCF designs benefit nine orders of magnitude reduction of the permutation evaluation compared to the brute force method. 6-core fibres' inter-core crosstalk at 1550 nm is ultra-low between -91.16 and -57.41 dB/km. The XT of 8-core fibres is optimised to -58.43 dB/km for the CL-band and -54.98 dB/km for the SCL-band. Following the core profiles generated by our AI-based method, it can be concluded that the range width of most of the fibre index profile parameters can be reduced so that the total permutation number can be reduced by 991$\times$ for the 6-core case and 3.6e5$\times$ for the 8-core case. This can largely reduce the MCF design time.

In terms of transmission, the capacity of the proposed 8-core fibre is higher than the 6-core fibre covering the same bands from 50 km until 10000 km. The AI-design method delivers an 8-core fibre design that can offer notable capacity improvement, around 32% (approaching the theoretical 33.3%) for 50 km transmission. However, the 8-core fibre has a higher capacity degradation rate over distance leading to a similar performance at 10000 km.

A thorough exploration of the effects of bandwidth, XT and A_{eff} is conducted. Increasing the core density from 6 cores to 8 cores in standard cladding diameter reduces bandwidth achieved per core, reduces the A_{eff} and increases the XT. By investigating the SSE of MCFs, it can be noted that 8-core ultra-wide-band fibres experience slightly sharper SSE degradation compared to 6-core ones. The capacity reduction brought by the smaller A_{eff} is similar for both the 6-core and 8-core fibres. However, the change of XT leads to a significantly different performance behaviour over distance. The 6-core fibres have ultra-low XT, which leads to a marginal influence. Minimizing XT in 8-core fibres is more important than offering high A_{eff} as it compensates the capacity penalty imposed by unavoidable A_{eff} reduction within a fixed cross-sectional area.

Chapter 7

Multi-core fibre fabrication yield optimisation

7.1 Associated publications and contributions

The content in this chapter will be submitted to Scientific Report after patent filing. Meanwhile, the method elaborated in this chapter will be licensed to Sumitomo Electric Industry ltd. for evaluation.

Mu, X., Ottino, A., Ferreira, and Zervas, G. Fabrication yield optimisation of heterogeneous multi-core fibres with Machine Learning.

- Primary author;
- Lead researcher.

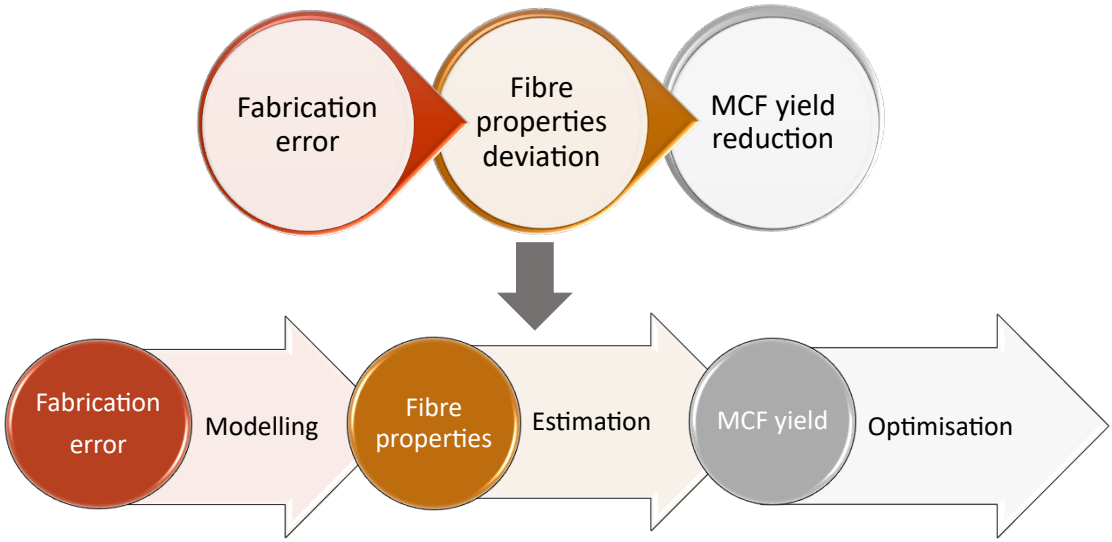

Fig. 7.1: Visualizing the problem addressed in this chapter. How can the influence of the fabrication error on multiple fibre properties be estimated? How can the fabrication yield be optimised while controlling the MCF properties?

7.2 Chapter summary

A high-level summary of the problem/motivations, proposed solution, and outcomes, as related to this chapter, is:

- Problem: Even though the fabrication process of the MCF has been improved in the past years, fabrication error is inevitable and leads to the deviation of the fibre properties from the fibre design. As a result, the yield of the MCF will be reduced as shown in Fig. 7.1. How can the influence of the fabrication error on multiple fibre properties be estimated? How can the fabrication yield be optimised while controlling the MCF properties?

- Proposed solution: First, machine learning methods are used to realize ultra-fast fibre properties estimation because when calculating the fabrication yield of each MCF structure, thousands of random samples are drawn from the probability distributions of the index-profile variables and then they are used to evaluate the optical properties. Without the speed up by the ML, each optimisation process will take years. Then, the cost function is designed to quantify every optical property distribution of the samples. The fitness value obtained with the sum of cost functions is used to represent the fabrication yield. Searching for the minimal fitness value with PSO algorithm equals searching for the maximum fabrication yield while satisfying all the property constraints.

- Outcomes:

  – ML tools in section. 4.1.2.3 are trained for the fibre properties calculation covering the parameter range including the fabrication error. The fibre properties calculation is sped up by up to around 10^6x.

  – A general fabrication yield optimisation process is proposed for the case in which there are several parameters to control and multiple properties being influenced.

  – As for MCF, the yield of 6-core fibre is increased to above 90% in almost property-constraint combinations from below 19% when there is no consideration of fabrication yield optimisation.

7.3 Introduction

The research presented in the above two chapters has demonstrated the efficiency and reliability of the AI-based method on MCF design optimisation. As mentioned in Chapter 3.2, even though the MCF fabrication method has been improved in the past years, comparing the fabricated MCFs to the design, there is always structural deviation. For example, the deviation of the core-to-core distance is reported to be $\pm 0.2\mu$m [71] or $\pm 0.3\mu$m [33]. The core structure also deviates from the design [71, 110]. As a result, the optical properties of the fabricated fibre also deviate from the expectation, such as effective mode area (A_{eff}) and cut-off wavelength in both

homogeneous [30, 33, 71, 110] and heterogeneous fibres [80, 82, 93, 162]. Furthermore, in mass production, the quantity of fabricated fibres is huge and some would hold unacceptable performance metrics due to the fabrication error, which results in reduced yield. This chapter addresses the fabrication error influence on the MCF design and fabrication yield by proposing a fabrication-yield optimisation method based on AI techniques.

Yield estimation and optimisation have been a long-lasting topic in device fabrication, especially for integrated circuits and micro-systems [163, 164, 165, 166, 167]. However, so far there is no reliable method to estimate and optimise the fabrication yield of MCFs. MCF design itself is a multi-dimensional and multi-constraint problem. AI based optimisation process [1] is proposed for MCF design but without consideration of fabrication error. Thus, herein we propose the AI-based optimisation process to include the multi-dimensional fabrication error influence on multiple properties and realize the yield improvement.

There are three difficulties in the MCFs fabrication yield estimation and optimisation and this work is devoted to the solutions respectively. First, each core or each type of core in MCFs might suffer from different fabrication errors. In heterogeneous MCFs, the complexity of the fabrication tolerance modelling increases with the core number and the type number. In this work, there are two types of cores neighboring each other in a ring structure in the standard cladding diameter. To address these difficulties, we first make the assumption that the cores that have the same index profile design will have the same fabrication error.

The second one is that there are multiple fibre properties of which the tolerance needs to be addressed. Moreover, each property has different responses to the shifts. Herein, cost functions are designed to translate the property distributions to penalty distributions. Then, they are added up to be a part of the new objective function to include all the mechanical and optical properties together. The mechanical property here is the distance between the adjacent trench edges. When the two types of cores have different fabrication deviations, there would be two distances between the adjacent trench edges as D_1 and D_2 shown in Fig. 7.2. As for the optical properties, the most concerned—inter-core XT, coating loss, A_{eff}, cutoff wavelength, CD—are comprised. Inter-core XT will be minimised while the others are constrained with corresponding thresholds.

The last one is the computation time. Many samples are needed to get stable distributions of optical properties. Calculating the properties of thousands of samples around one MCF structure with numerical methods will take hours. During the optimisation process, the fabrication error influence on many MCF structures needs to be checked to find out the optimum. It will take months to do the optimisation for one application. Therefore, the regressors of the optical properties are trained to speed up

the whole process while keeping high accuracy.

After addressing these difficulties properly, the PSO algorithm is used to optimise the fitness value of the objective function. After the optimisation, the fabrication yield of the two-type-core heterogeneous fibre, the corresponding XT penalty and the property distribution of samples around the optimised MCF are analysed.

7.4 Fabrication tolerance modelling

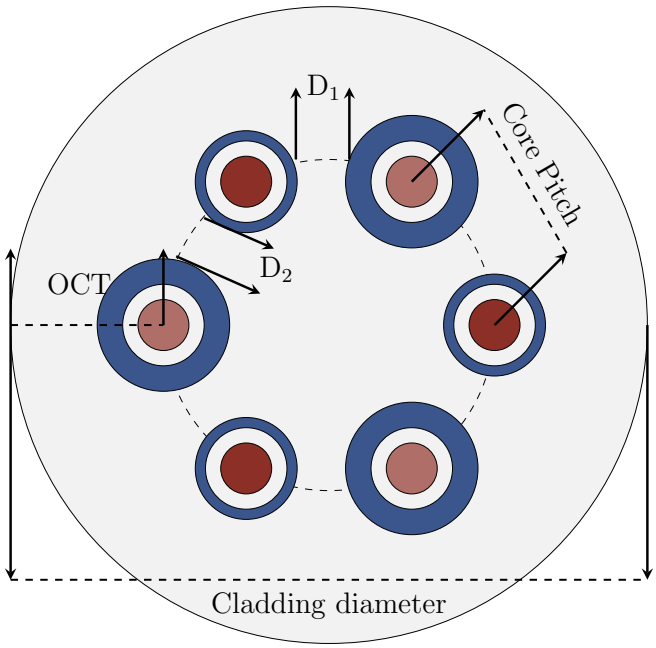

Fig. 7.2: Trench-assisted Hete-MCF layout. (OCT: Outer Cladding Diameter)

The error that happens in fabrication is modeled by a normal distribution. The standard deviation (std) of the normal distribution depends on the fabrication accuracy and the confidence interval that the MCF fabrication needs. Here the confidence interval 99.73% is assumed and it corresponds to 3σ for all the parameters. For example, as for the layer width, it is assumed that $3\sigma = 0.1\ \mu m$, which means that the fabrication has 99.73% probability to bring error $\leq 0.1\ \mu m$ on each layer. The maximal corresponding deviation is around $\pm 0.15\ \mu m$. For the 5 refractive-index profile parameters and the core position, the assumption of the deviation is shown in Table 4.2. It is worth noting that as for the core position, with the position error $0.1\ \mu m$ at both the x and y axis for two neighbouring cores, the deviation of the CP becomes $\pm 0.25\ \mu m$ and that of the OCT is $\pm 0.15\ \mu m$.

7.5 Optimisation process

In brief, the optimisation process includes four steps. First, the fabrication error was modelled with normal distribution. Based on the probability distributions, random samples are drawn. Then, the distributions of the properties, such as cut-off wavelength and A_{eff} in Fig. 7.3, were calculated with the regressors. These property distributions are converted to the penalty distribution via the penalty functions and added up together resulting in a multi-peak penalty value distribution. The peaks represent the constraints broken. More constraints are broken, which leads to more peaks and then a wider penalty distribution. After using PSO to optimise the fitness value which is the 90% value of the distribution, the peaks are almost eliminated in the optimised results.

The optimisation process is tested with the following constraints of the properties:

- The distance between the adjacent trench edges needs to be equal or larger than 2 μm;
- The coating loss needs to be equal to or lower than 0.001 dB/km;
- The CD is constrained between 16 and 25 ps/nm/km;
- The A_{eff} is constrained between two A_{eff} values. As for the example in Fig. 7.9(e), A_{eff} constraint is [50 60] μm^2;
- The cut-off wavelength needs to be lower than the threshold: (1530-19) or (1460-19) nm for C+L band or SCL band. 19 nm is the regression error buffer of the cutoff wavelength regressor which can cover 99% regression error.

The first three are kept the same while several combinations of constraints, cutoff wavelength and A_{eff} are tested.

The objective function is a mathematical interpretation of the physical property requirements for the AI to understand and perform its task efficiently. In this work, the objective function of the MCF design including fabrication tolerance is split into two parts as depicted in Fig. 7.4. The first part [1] is to check the particle itself, which represents an MCF structure, to see if it satisfies the constraints of the properties. The fitness value of the particle is calculated with the penalty functions proposed in Section 5.5. If all the constraints are satisfied, the particle comes to the second part in which the fabrication sampling is conducted around the particle and then the properties are calculated for all the samples. Using the penalty functions in Section 7.5.1, the properties are translated to the corresponding penalty. The fitness value is the 90% value of the distribution which is the sum of the penalties of all the properties. By minimising the fitness value using PSO algorithm [1], the fabrication yield of the MCF structure can be improved.

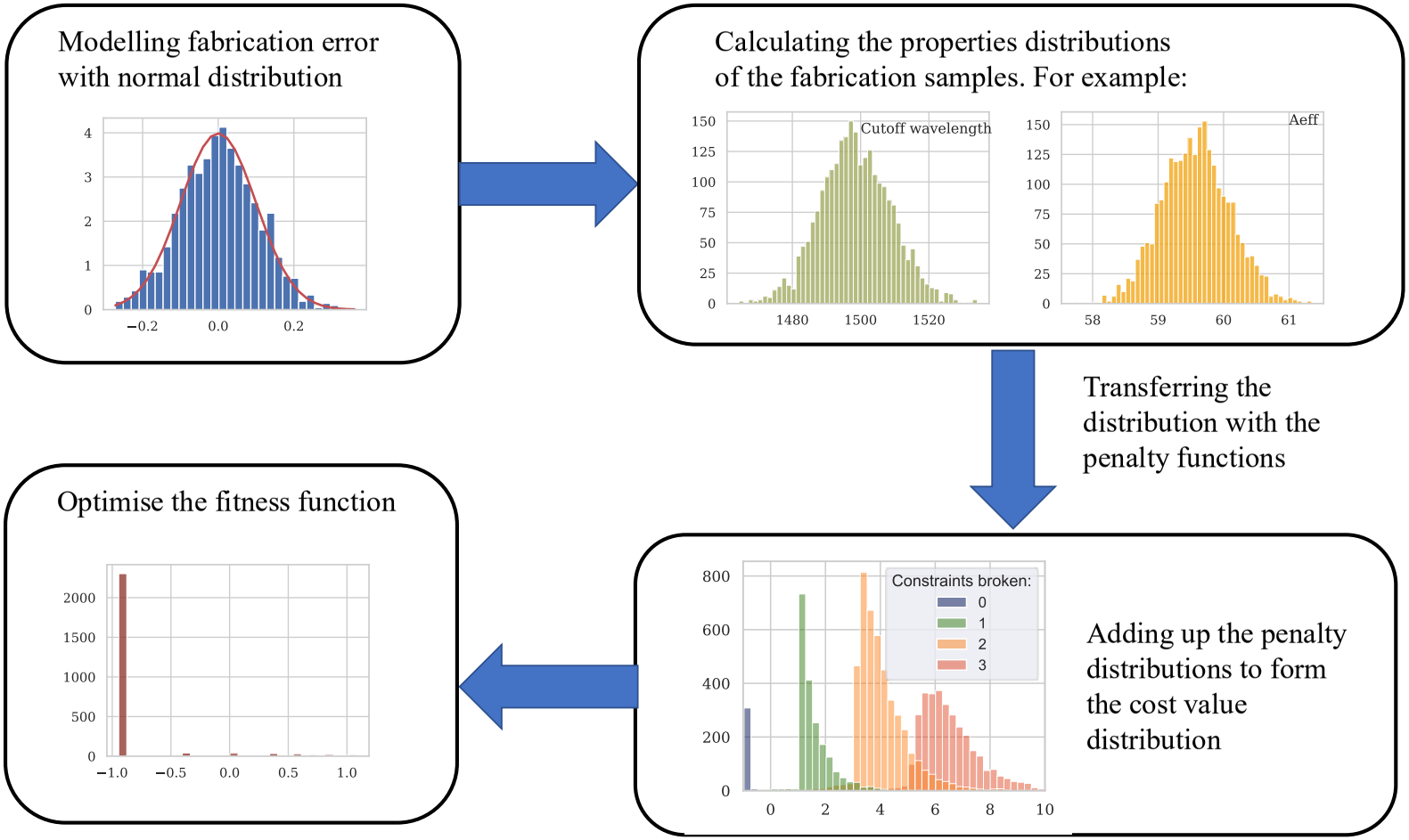

Fig. 7.3: The workflow to include fabrication tolerance in the optimisation process.

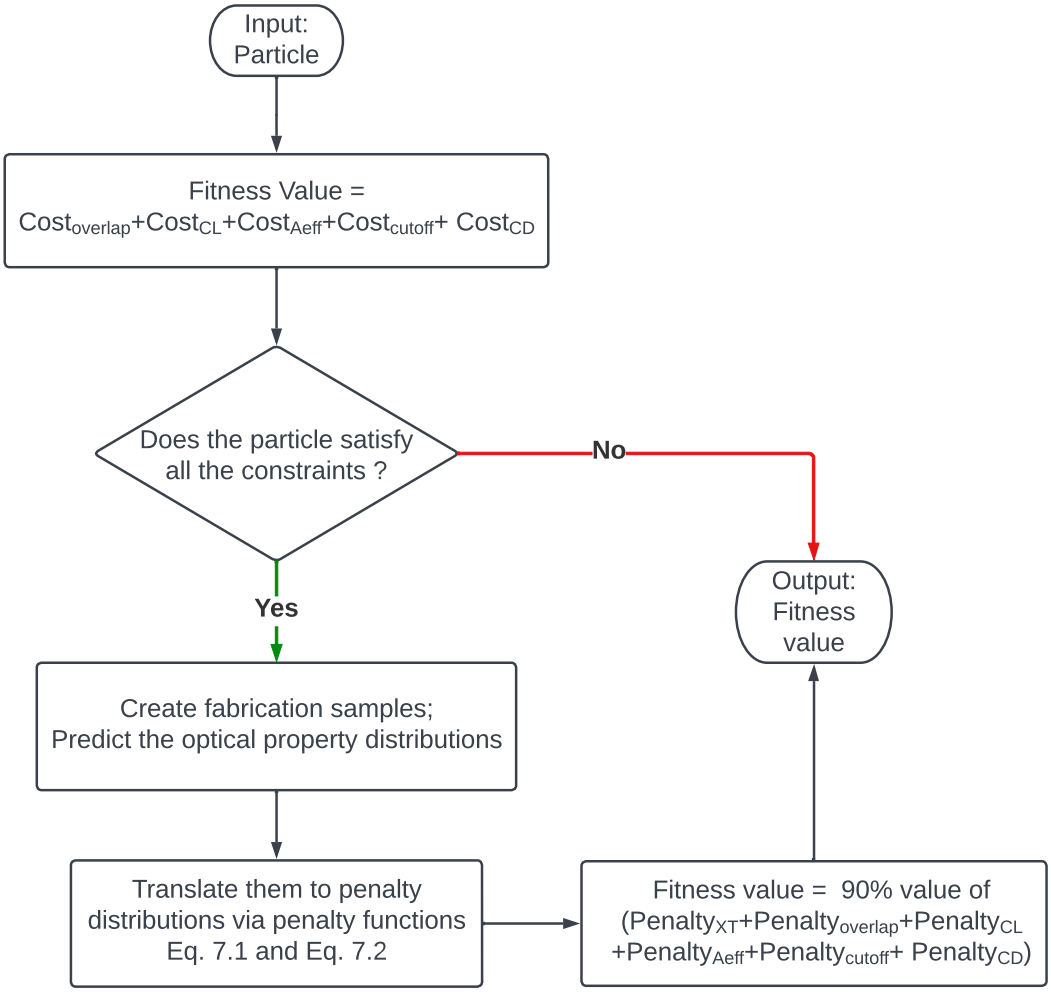

Fig. 7.4: Objective function workflow in fabrication yield optimisation.

7.5.1 Penalty function design

The design purpose of the penalty functions is to treat XT as the main optimisation objective while making sure that the sum of the penalty function represents the situation where the samples break the constraints. Hence, there are a few design strategies:

- The penalty range of XT and the penalty range of the constraints are designed to be negative and positive;
- The value of the constraints penalty should be larger than the absolute maximal value of XT penalty. Then, when all the penalty functions are summed up, the peak of XT penalty won't be eliminated. Thus, when the XT penalty is designed to be within [-1 0], the constraint penalty is designed to be sharply increased to 2 with a tiny constraint break ($\leq 10^{-6}$);
- The penalty functions are designed to be continuous and their gradients decrease. Hence, optimisation algorithm can have an easier understanding of the

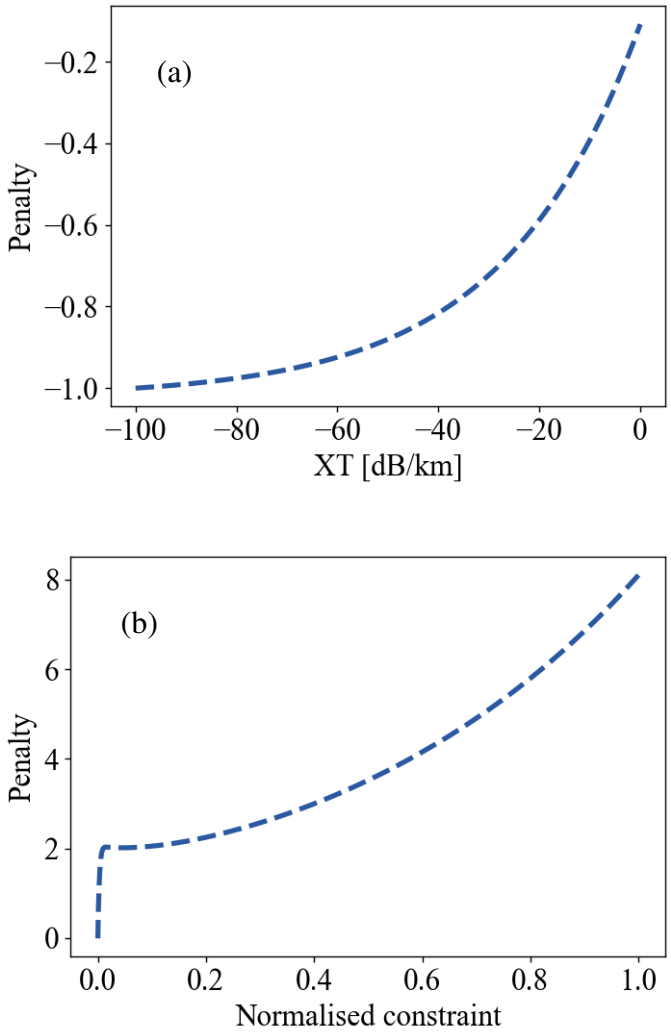

Fig. 7.5: (a) the penalty curve of XT; (b) the penalty curve of optical properties constraints obtained by scaling the normalised constraint.

optimisation direction.

Following the above design strategies, the XT scaled to [-1 0] with an exponential fitting function as follows:

$$\text{Penalty}_{xt} = ae^{(bx+c)} + d, \tag{7.1}$$

in which the x is the XT. The fitting curve is shown in Fig. 7.5 (a). For each constraint, the penalty scaled from the normalised constraint increases significantly from 0 to 2 with a tiny normalised constraint value. Then, it increases following a parabolic trend from 2 to 8 as illustrated in Fig. 7.5 (b). The upper limit of the constraint penalty will influence the spreading of the multi-peak distribution but will not influence the fitness value. The fitting function of optical property is designed to be the sum of four

exponential functions as follows:

$$\text{Penalty}_{op} = \sum_{1}^{i=4} a_i e^{(b_i x + c_i)}, \tag{7.2}$$

in which the x is the normalised constraints and op is the D_1, D_2 and coating loss, A_{eff}, cutoff wavelength, CD of two types of cores.

XT and the constraints are on the negative and positive sides respectively. Meanwhile, the absolute value of the constraint penalty is larger than that of the XT as soon as the sample structure breaks one of the constraints. As a result, the summation of the penalty functions shows multiple peaks. Moreover, when more distributions are summed together, more peaks and a wider range of the summation as illustrated in Fig. 7.3. Thus, the width of the distribution represents the number of constraints that are broken to a certain extent. By reducing the peaks and pushing the distribution to [-1 0], more structure samples satisfy the constraints. If all the fabrication samples satisfy all the constraints, the distribution is purely that of the XT.

7.5.2 Penalty distribution of samples

To make sure the penalty distribution of each MCF structure is stable, the Jensen–Shannon divergence (JSD) is used to compare the distributions obtained with different sample numbers. The JSD decreases with increasing sample number and 0.01 is used as the threshold at which the distribution starts to stay stable. Fig. 7.6(a) is an example of how the running JSD (rJSD) decreases with the sample number. It can be seen that for this particle, the rJSD reaches the threshold of 0.01 when the sample number is 1481.

To find the sample number that assures all the particles can hold a stable penalty distribution, JSD tests are conducted for 500 random particles. The sample numbers at which the JSD reaches the threshold are recorded and its distribution is shown in Fig. 7.6 (b). The maximal sample number is 2354, and therefore we pick 2500 to be the sample number in the following MCF optimisations. To further reduce the noise of the 90% value of the penalty distribution, it is calculated 9 times and then the 90% confidence interval of the 9-value set is obtained to be the fitness value.

7.6 Performance evaluation

The swarm of particles reduces the fitness value with increasing iterations for searching for the lowest fitness value as illustrated in Fig. 7.7 (a). For each case of optical properties requirements, PSO is conducted 10 times. Because the particles are initialised randomly, the start points of the runs are different. However, after the search

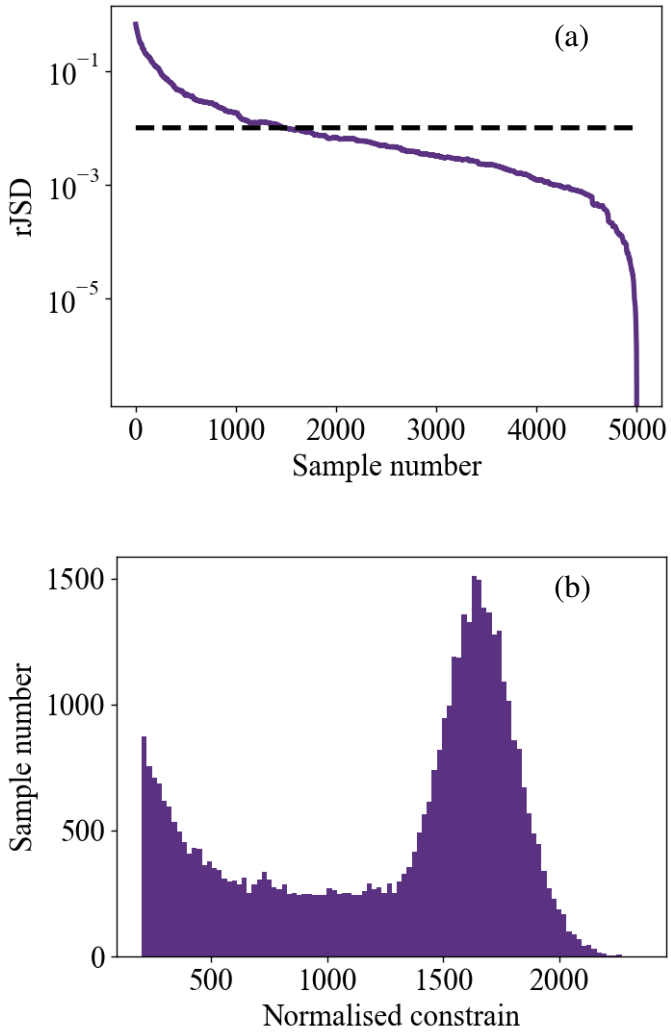

Fig. 7.6: (a) example of rJSD decreasing with sample number; (b) Sample number distribution at which the rJSD reaches the threshold 0.01 as the example in (b).

iteration by iteration, the fitness value is reduced and converges to the optimal structure with the minimum. As for the fitness value distribution of the fabrication samplings, it has tiny peaks and is mainly laid in the range [-1 0] which is the XT region. The distribution in the case that there is no yield optimisation in the design process spreads in the range [-1 5] with several peaks. In other words, the MCF structure reaches a high possibility of satisfying all the constraints while having a low XT. An example of the penalty value distribution of the fabrication sampling around the optimised MCF structure with or without the consideration of the fabrication error is shown in Fig. 7.7 (b).

The fabrication yield was checked as the percentage of the samples that lie in the valid region for all the properties constraints. The MCFs [1] optimised without considering the fabrication deviation have a low fabrication yield of less than 21% as

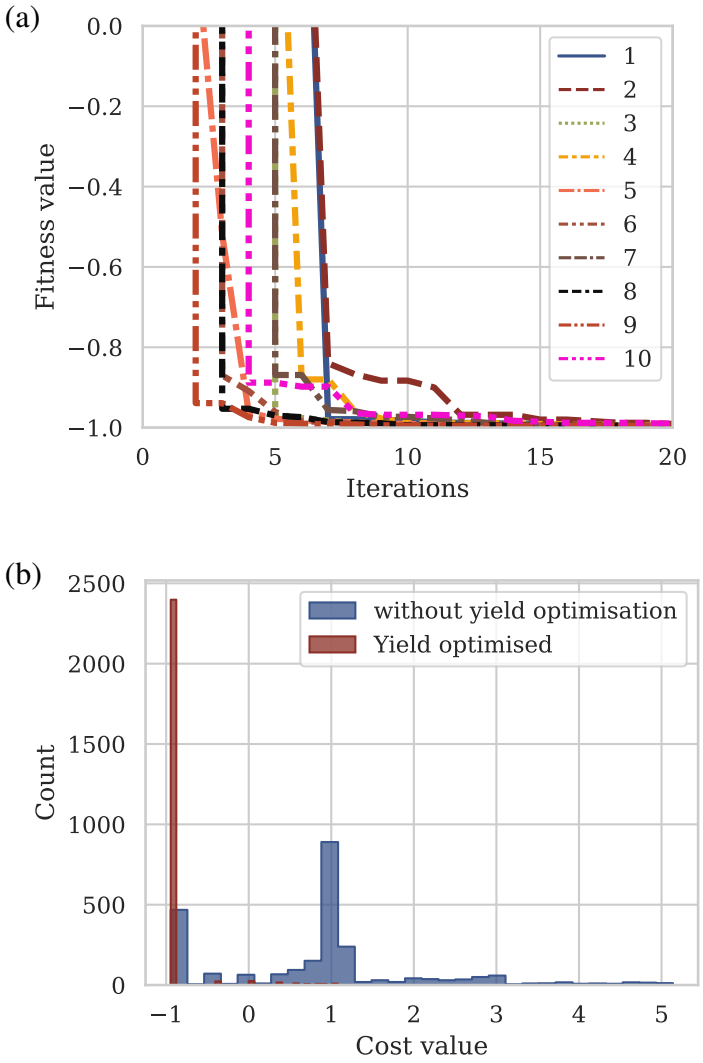

Fig. 7.7: (a) Learning curves of 10 runs for the case 1530 [50 60]; (b) Fitness value distributions of fabrication samples in the cases with or without optimisation of the fabrication tolerance.

the blue bars illustrated in Fig. 7.8. In this case, the optimisation focuses on minimising XT and therefore the other properties are usually pushed to the edge of the constraints. The fabrication samples around the optimised MCF structure are highly possible to break the constraints.

After the yield optimisation, the success possibility increases significantly shown as in the brown bars. In most cases, the yield can reach above 90%, which means that the optimised MCF structure has at least 90% possibility to be fabricated to satisfy all the property requirements even though suffering the fabrication error. The other 10% fabrication samples break one or two constraints because of the corresponding distributions' tail. As for the extreme case, 1530 [70 80], the valid sample ratio increases from 2.4% to 72%. Thus, even in a case in which the optical properties have

already been pushed to the border, the fabrication success rate can still be improved to around 50% through AI-based optimisation.

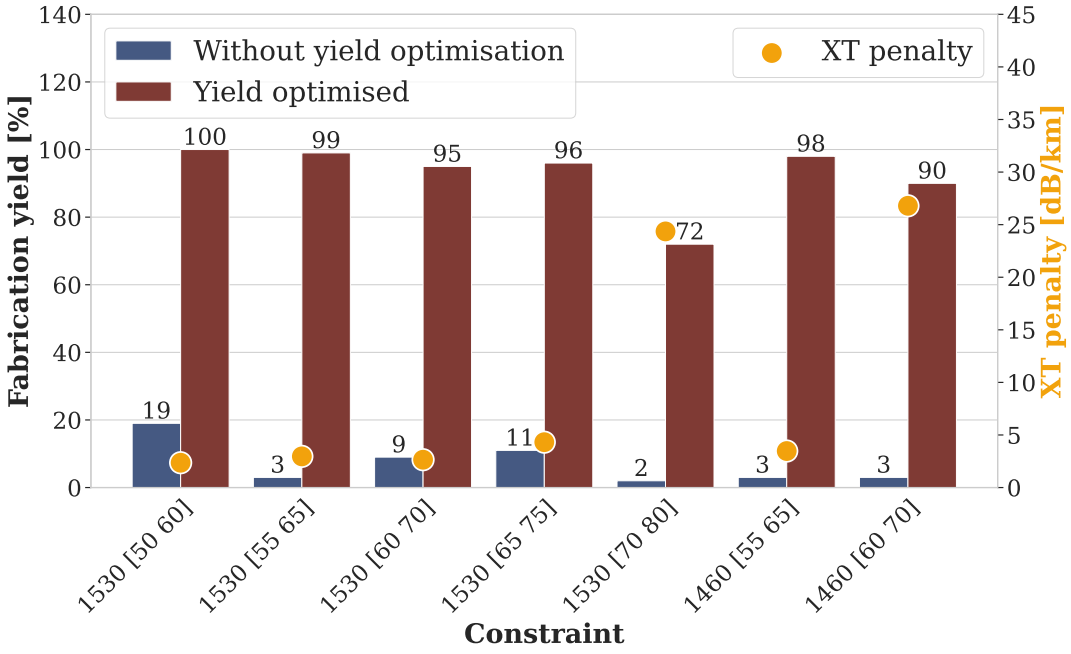

Fig. 7.8: Fabrication yield of MCF and the XT penalty brought by the yield optimisation.

Because the MCFs optimised without tolerance consideration are focused on the XT minimising as mentioned before, when the fabrication tolerance is added, the XT would be degraded to cover the gap and leads to an XT penalty as in Fig. 7.9 (a). In the left four cases, the XT penalty is lower than 4 dB/km which is negligible. In other words, via this AI-based yield optimisation method, the fabrication yield can be increased above 90% with marginal XT degradation. However, when the constraint combination approaches the TA core's boundary, the XT penalty increases to around 25 dB/km. In these requirements, the MCF needs to sacrifice the XT performance to the improvement of fabrication yield. Nevertheless, the inter-core XT after yield optimisation is still around -60 dB/km in Table 7.1 which is suitable for long-haul transmission system [158].

The distributions of the overall XT and that of the properties of two types of cores after the optimisation are calculated with 2500 samples around the optimised MCF structure with constraint 1530 [50 60] shown in Fig. 7.9. It can be seen that with the same fabrication samples, the range and variation of the optical properties distributions are different. This further demonstrates the difficulty of comprising them in one optimisation process. Compared to the case without yield optimisation, most of the optical properties are pushed further away from the threshold lines to ensure that more fabrication samplings can satisfy the constraints. In this case, 1530 [50 60], the coating

loss of the two types of cores is closer to the threshold of 0.001 dB/km than that without optimisation. That is because the constraints mutually restrain. For example, in general, wider A_{eff} leads to higher coating loss and worse XT. This also leads to outliers that fail in the fabrication.

To show the property change quantitatively, we define the guardrail as the average distance to the threshold of the two types of cores and compare it between the two cases: w.o yield and w yield, as shown in Table. 7.1. Overall, Δguardrails of the properties are small. In other words, the improvement of the fabrication yield only requires small property sacrifice. The D_{tr} for all the constraint combinations is wider than that in the case without yield optimisation because the cores are smaller for getting smaller cut-off wavelength which is the property significantly changed. They have pushed away from the threshold for between 6 to 56 nm. Meanwhile, the A_{eff} are between 0.31 to 2.81 μm^2 closer to each other. To make up for these guardrails' increase, the CL and CD slightly approach the threshold by less than 7% and 3% respectively but without constraint breaking.

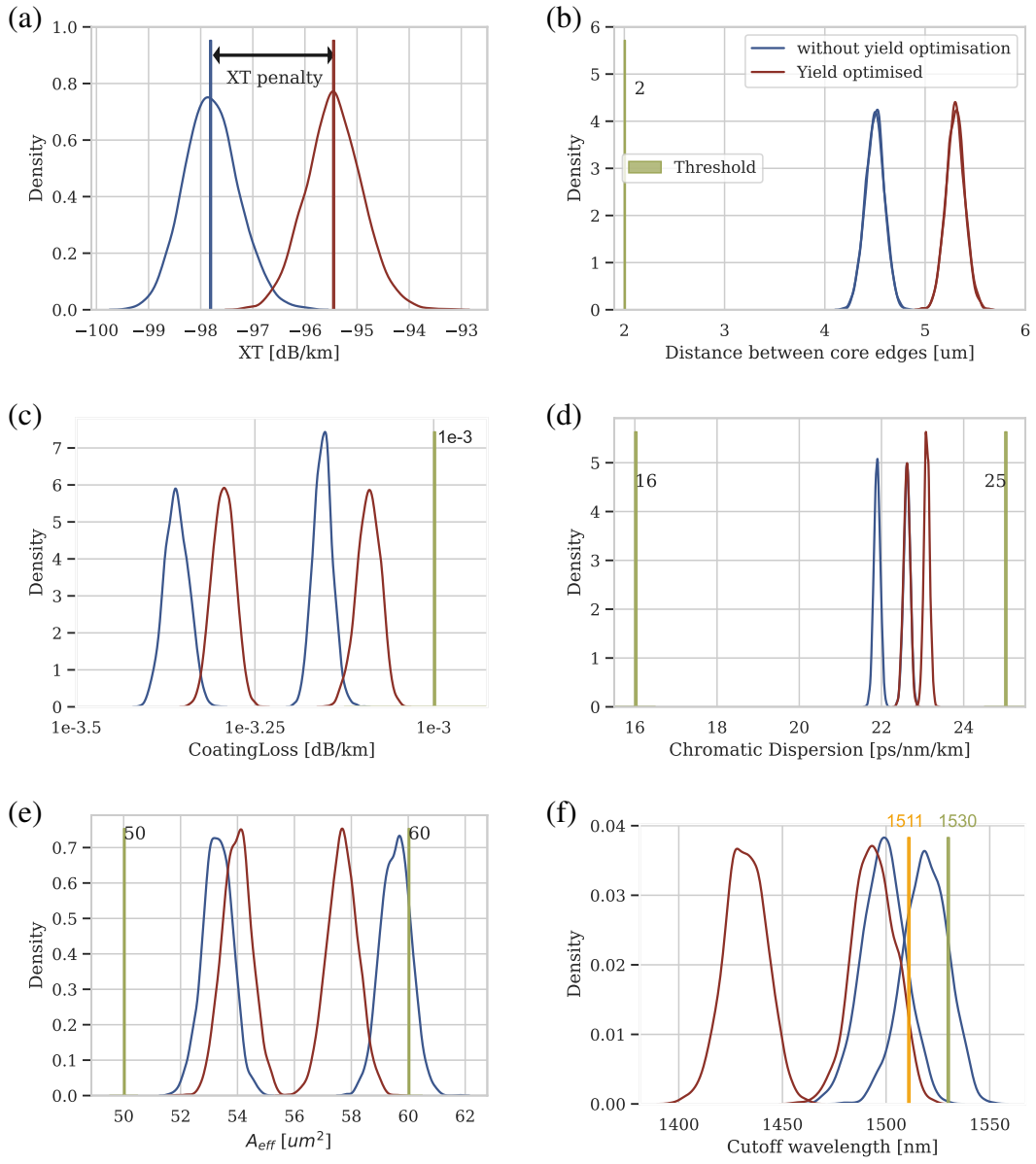

Fig. 7.9: kernel density estimate (KDE) plot of the properties in MCFs with or without yield optimisation for the constraint 1530 [50 60].
(a) overall XT; (b) distance between the trench edges of the neighboring cores; (c) coating loss; (d) chromatic dispersion; (e) A_{eff}; (f) cut-off wavelength;

Case	Constraint	Yield	XT	D_{tr}	Cutoff1	Cutoff2	$A_{eff}1$	$A_{eff}2$	CL1	CL2	CD1	CD2
w.o yield	1530 [50 60]	18.63	-97.83	4.50	1499	1518	59.57	53.26	-3.61	-4.44	21.89	22.61
w. yield	1530 [50 60]	96.15	-95.47	5.30	1432	1495	57.70	53.97	-3.34	-4.17	23.10	22.61
Δ guardrail			2.36	0.80	45		1.29		-0.24		-0.12	
w.o yield	1530 [55 65]	2.99	-96.18	3.20	1497	1518	62.54	55.01	-3.28	-4.16	21.30	22.17
w yield	1530 [55 65]	98.48	-93.22	5.40	1483	1420	56.25	58.16	-3.95	-3.22	22.76	23.13
Δ guardrail			2.97	2.2	56		2.81		-0.13		-0.25	
w.o yield	1530 [60 70]	8.77	-92.21	3.70	1495	1521	63.46	60.47	-3.16	-3.88	21.20	23.18
w yield	1530 [60 70]	91.95	-89.57	4.50	1471	1493	61.58	60.93	-3.25	-3.64	21.84	23.16
Δ guardrail			2.65	0.8	26		1.17		-0.08		-0.33	
w.o yield	1530 [65 75]	11.36	-87.90	3.60	1514	1494	65.62	65.12	-3.49	-3.10	23.37	21.68
w yield	1530 [65 75]	93.83	-83.59	4.50	1482	1485	66.96	66.22	-3.10	-3.25	23.52	23.28
Δ guardrail			4.31	0.9	20.5		-0.12		-0.12		-0.73	
w.o yield	1530 [70 80]	2.36	-82.38	4.90	1492	1514	71.11	70.11	-3.01	-3.15	23.83	23.53
w yield	1530 [70 80]	45.05	-58.02	5.50	1505	1505	71.23	71.23	-3.12	-3.12	23.85	23.85
Δ guardrail			24.36	0.6	-2		0.5		0.04		-0.15	

Table 7.1: Comparison between MCFs with or without yield optimisation.

Case	Constraint	Yield	XT	D_{tr}	Cutoff1	Cutoff2	$A_{eff}1$	$A_{eff}2$	CL1	CL2	CD1	CD2
w.o yield	1460 [55 65]	3.07	-91.17	5.10	1401	1452	59.12	55.42	-2.96	-3.59	23.18	22.28
w yield	1460 [55 65]	93.93	-87.70	5.30	1422	1413	56.10	58.63	-3.39	-3.10	22.44	23.15
Δ guardrail			3.47	0.2	9		0.59		-0.03		-0.1	
w.o yield	1460 [60 70]	2.79	-86.47	5.10	1411	1446	61.16	60.15	-2.95	-3.25	23.33	22.68
w yield	1460 [60 70]	86.37	-59.68	6.30	1422	1423	60.87	61.26	-3.15	-3.15	23.29	23.37
Δ guardrail			26.79	1.2	6		0.31		0.05		-0.28	

Comparison between MCFs with or without yield optimisation.

7.7 Summary

This chapter presents the optimisation method with pure AI techniques of the heterogeneous MCF fabrication yield. The fabrication error modeled with normal distribution is added around the MCF structure to create the fabrication samples. The corresponding property distributions can be obtained with the regressors and then interpreted with penalty functions. The distribution of the sum of penalties includes peaks which correspond to how many constraints the fabrication samples break. The range is narrower and closer to -1, which means more fabrication samples that satisfy all constraints and have lower XT.

This optimisation process contains the replacement of numerical calculation of the optical properties with machine learning and the optimisation with PSO algorithm. The former technique contains the multi-variate linear regressors of the linear and/or second-order linear relationship and the residual regressor. It speeds up the calculation by up to around 10^6 times with high accuracy. The latter results in the increase of fabrication yield under various combinations of constraints with small property changes. Yield estimation and optimisation are the concerns in every engineering design problem. Combined with AI methods, the estimation and optimisation of fabrication yield can be more efficient and powerful.

Chapter 8

Conclusions and Future Work

The research on TA MCF design with AI techniques in various configurations has been presented in this thesis. The noteworthy findings and the perspectives on future work encompass this chapter.

8.1 Conclusions

The exponentially-increasing capacity requirement has exceeded the SSMF capability. SDM has proven its potential to overcome the capacity crunch. Existing MCFs were generally designed by taking two or three parameters as variables while fixing others. Meantime, the numerical methods of fibre optical properties calculation in Chapter 2 are time-consuming, which is the barrier to optimising MCF throughout the search space. Therefore, in this thesis, an AI-based method to optimise heterogeneous MCF has been proposed and further developed.

In Chapter 5, the optimisation process is elaborated. Two objectives, *XT-optimisation* and A_{eff}*-optimisation* were tested with other properties constraining for satisfying transmission requirements. The objective function comprises one of the objectives and constraints to give fitness value to each MCF structure. The fitness value represents the MCF's performance and is used by the optimisation algorithm to decide the optimisation direction. The optimisation algorithm and the ML methods used to replace the numerical methods are presented in Chapter 4. The coating loss regressor and classifier were used here and the combination of them can offer prediction with 0% false positive. This method optimised the 6-core heterogeneous TA fibre for different combinations of A_{eff} and cutoff wavelength. The AI-based method has shown its ability to design MCFs by handling 10-dimensional particles and multiple properties. Permutation numbers are reduced by ten orders of magnitude compared to the brute-force method. The optimised 6-core fibres have ultra-low XT and large A_{eff}, leading to even better RCMF than the 7-core fibre. By evaluating the MCF transmission performance with the ISRS GN model, it is found that the PSO-designed 6-core fibre can deliver up to $\sim$1.2 Pbit/s for 1200 km. For S+C+L bands, the optimised fibres have 35% and 84.8% more capacity than the 7-core fibre.

To extend the previous work to take the unique TA fibre core loss mechanism into

consideration, a new cutoff wavelength regressor was trained with LP11 loss of the TA core at straight conditions. The regressor was elaborated on in Section. 4.1.2.2. The updated optimisation method explored more fibre designs in both 6-core and 8-core fibre cases. 6-core fibres still keep ultra-low XT while 8-core fibres have relatively higher XT because of the higher spatial density. By comparing the optimised fibres' index profiles, it is found that the search space can be reduced in the future TA-MCF optimisation to save computation costs. As for capacity in 50 km transmission, the optimised 8-core fibre can provide around 32% more than the 6-core fibre, which is close to the ideal 33.3% corresponding to the spatial density increment.

As mentioned in the introduction, MCF capacity is influenced by several factors; among them, complex linear and nonlinear relationships exist. Furthermore, the impact of the crucial MCF properties (bandwidth, A_{eff}, XT and core number) on the capacity performance was investigated thoroughly. The increasing core number in standard cladding diameter leads to the achievable bandwidth per core reduction, A_{eff} reduction and XT degradation. SSE comparison at different transmission distances reveals that although the large spatial density can offer higher SSE at short transmission distance but suffer sharper reduction when it comes to long-haul. Meanwhile, the A_{eff} change has a similar influence on both 6-core and 8-core cases. However, for 8-core fibres, because their XT is above -60 dB/km, the XT-induced penalty on capacity increases sharply with transmission distance. In conclusion, when designing 8-core fibres, minimizing XT should be emphasised. As for 6-core fibres, since their XT is ultra-low and therefore results in a much smaller penalty compared to the benefit brought by A_{eff} increase. When designing MCF with a relatively smaller spatial density, the design objective can be focused on the A_{eff} improvement while keeping XT at an acceptable level.

After achieving the automatic and efficient MCF design method, in order to eliminate the gap between the design and fabrication, a pure-AI fabrication yield optimisation process was proposed in Chapter 7. Fabrication error deviates the design structure away from the expectation, leading to optical properties aberration. In mass production, it manifests as the reduction of fabrication yield. By adding the fabrication error to create fabrication samples around the design and then using cost functions to translate the optical properties into cost value, the objective function includes all the constraints distributions. Replacing the numerical calculations with ML methods improved the computation time up to $10^6\times$, which significantly solved the computation cost problem brought by a large number of fabrication sample evaluations. The fitness value was optimised to search for the MCF design which has the highest yield while suffering fabrication error. Comparing the MCF designed with fabrication yield optimisation to the MCF designed without considering the fabrication error influence, it can be seen that the fabrication yield is increased above 90% in most

cases from below 20%. As for the MCF optical properties, mostly A_{eff} and cutoff wavelength was pushed away from the threshold to prevent breaking the constraints while coating loss and chromatic dispersion moved closer to the threshold to compensate for the previous guardrail broadening. In a nutshell, the yield optimisation process has proven that it can achieve good yield with tiny optical properties degradation.

Overall, the research represented in this thesis is around the TA MCF design and optimisation. New methods to find optimal MCF designs that meet different requirements were proposed on the basis of AI. First, MCFs with different core numbers under various properties constraint combinations were designed for two objectives: minimising XT or maximising A_{eff}. The optimised MCFs have a low XT and a good RCMF. AI techniques speed up the computation time by around a million times and reduce the permutation number by ten orders of magnitude. Second, the MCF design is followed by capacity evaluation. The transmission performance of the optimised MCFs was appraised for different transmission distances and compared with each other for investigating the influence of the optical properties change. Finally, the fabrication yield of the MCFs was optimised by adding the fabrication error impact on the optical properties distributions into the fitness value calculation.

However, in the transmission performance evaluation, the influence of CD and its slope on the capacity is not considered comprehensively. The CD is assumed as a linear function of its value and its slope at the central frequency for the whole bandwidth. The dispersion itself is decreasing towards a shorter wavelength while the dispersion slope is increasing. When the dispersion is relatively large, the Kerr effect decreases with frequency spacing, reducing the NLI noise. Thus, when the channels are around the zero-dispersion wavelength, they will be sensitive to NLI noise. Although the assumption of constant dispersion slope is proven to have a negligible influence on the SNR estimation for up to S+C+L band [52, 168], for ultra-wideband like E+S+C+L and O+E+S+C+L band, the closed-form GN model is not accurate as the integral form. Thus, the SNR estimations for the E+S+C+L and O+E+S+C+L band fibre should be conducted with the integral form GN model.

Meanwhile, the power profile should be optimised to compensate for the power transfer between channels caused by ISRS for maximising the throughput [124, 125]. Therefore, the maximized capacity of the fibres which cover different bands can be compared.

8.2 Future work

Following the research reported in the thesis, there are several interesting directions that can be explored. In this section, they are described briefly.

8.2.1 MCF Design Method Development

Sumitomo will evaluate the ML toolkit developed in this work in the near future. The accuracy and efficiency will be improved further by the collaboration. More tools will be added to the toolkit according to the needs of fibre manufacturers.

The work in this thesis mainly focuses on the TA index profile and the ring structure. As mentioned in Chapter 3, there are numerous index profiles, core arrangements and different materials, such as pure-silica core. Developing the AI-based MCF design method to cover more fibre types can offer more choices to researchers or customers when they need to do some customisation. Different types of cores have their own index-profile parameters and optical behaviours. Thus, the data sets of their optical properties need to be collected and then used to develop the ML methods to replace the numerical calculation. Then, the objective function needs to be adjusted based on the optical properties range and the application requirements.

Meanwhile, the single-mode operation is one of the design strategies here. To design few mode-MCF, more properties are required to be considered. Since there are few modes in each fibre core, the modal interaction is also ineluctable. Thus, in the design, the inter-mode XT [169] will be minimised. Similarly, the different group velocities of the modes lead to inter-mode dispersion, which limits the transmission system. Thus, DMD as one of the most important metrics will be minimised for reducing the inter-mode dispersion. In brief, more efforts are needed to develop the MCF design method to be an MCF design platform.

8.2.2 Optimised MCF Fabrication and Characterization

The optimised 6-core and 8-core fibre designs in this thesis have great performance in both XT and capacity. Although some of them have been verified with Sumitomo, they are not yet fabricated and characterised. Thus, one of the next steps is to manufacture some of the fibre designs and characterise them for comparison to the properties estimated in the simulations. Then, the MCF transmission experiment will be demonstrated to verify the capacity and the influence of the optical properties on transmission performance.

8.2.3 AI-based Design Method for Other Complex Structure

Similar to the MCF, the design of other complex components, such as photonic crystal fibre [170] or metasurface [171], needs to address multiple parameters and multiple property requirements. Thus, the design process is always time- and computation-consuming. Some AI-based design methods [172, 173] have been reported. However, fabrication yield optimisation has not been explored for these components. The cost function in the yield-optimisation AI-based method is designed

suitable for various property constraints. Thus, it can be applied for different component fabrication yield optimisation while controlling all the optical properties.

Bibliography

[1] Mu, X., Ottino, A., Ferreira, F. and Zervas, G. Optimization of 125-μm heterogeneous multi-core fibre design using artificial intelligence. *IEEE Journal of Selected Topics in Quantum Electronics* **28**, 1–13 (2022).

[2] Mu, X., Ottino, A., Ferreira, F. M. and Zervas, G. Design and transmission analysis of trench-assisted multi-core fibre in standard cladding diameter. *Opt. Express* **30**, 38152–38166 (2022).

[3] Saridis, G. M., Alexandropoulos, D., Zervas, G. and Simeonidou, D. Survey and evaluation of space division multiplexing: From technologies to optical networks. *IEEE Communications Surveys Tutorials* **17**, 2136–2156 (2015).

[4] Winzer, P. J., Neilson, D. T. and Chraplyvy, A. R. Fiber-optic transmission and networking: the previous 20 and the next 20 years [invited]. *Opt. Express* **26**, 24190–24239 (2018).

[5] Klaus, W., Winzer, P. J. and Nakajima, K. The role of parallelism in the evolution of optical fiber communication systems. *Proceedings of the IEEE* **110**, 1619–1654 (2022).

[6] Liu, Y., Yuan, H., Peters, A. and Zervas, G. Comparison of SDM and WDM on direct and indirect optical data center networks. In *Proc. of Eur. Conf. Opt. Commun. (ECOC)* (Dusseldorf, Germany, 2016).

[7] Saljoghei, A., Yuan, H., Mishra, V., Enrico, M., Parsons, N., Kochis, C., De Dobbelaere, P., Theodoropoulos, D., Pnevmatikatos, D., Syrivelis, D., Reale, A., Hayashi, T., Nakanishi, T. and Zervas, G. MCF-SMF hybrid low-latency circuit-switched optical network for disaggregated data centers. *J. Lightw. Technol.* **37**, 4017–4029 (2019).

[8] Yuan, H., Furdek, M., Muhammad, A., Saljoghei, A., Wosinska, L. and Zervas, G. Space-division multiplexing in data center networks: On multi-core fiber solutions and crosstalk-suppressed resource allocation. *J. Opt. Commun. Netw.* **10**, 272–288 (2018).

[9] Hayashi, T., Mekis, A., Nakanishi, T., Peterson, M., Sahni, S., Sun, P., Freyling, S., Armijo, G., Sohn, C., Foltz, D. *et al.* End-to-end multi-core fibre transmission

link enabled by silicon photonics transceiver with grating coupler array. In *Proc. of Eur. Conf. Opt. Commun. (ECOC)* (Gothenburg, Sweden, 2017).

[10] Mu, X., Ferreira, F. M., Ottino, A. and Zervas, G. Design optimization of uncoupled six-core fibers in standard cladding diameter using artificial intelligence. In *Optical Fiber Communication Conference (OFC) 2021*, Th1A.34 (Optica Publishing Group, 2021).

[11] Moon, P. and Spencer, D. E. *Field theory handbook: including coordinate systems, differential equations and their solutions* (Springer, 2012).

[12] Fleming, J. W. Dispersion in geo2–sio2 glasses. *Appl. Opt.* **23**, 4486–4493 (1984).

[13] Hermann, W. and Wiechert, D. U. Refractive index of doped and undoped pcvd bulk silica. *Materials Research Bulletin* **24**, 1083–1097 (1989).

[14] Chiang, K. S. Review of numerical and approximate methods for the modal analysis of general optical dielectric waveguides. *Optical and Quantum Electronics* **26** (1994).

[15] Vassallo, C. 1993–1995 optical mode solvers. *Optical and Quantum Electronics* **29**, 95–114 (1997).

[16] Goell, J. E. A circular-harmonic computer analysis of rectangular dielectric waveguides. *The Bell System Technical Journal* **48**, 2133–2160 (1969).

[17] Yeh, C. and Lindgren, G. Computing the propagation characteristics of radially stratified fibers: an efficient method. *Appl. Opt.* **16**, 483–493 (1977).

[18] Dods, S. R. A. Fiber vector modesolver - improvements to the efficient 4×4 matrix method. In *Integrated Photonics Research and Applications/Nanophotonics*, ITuF5 (2006).

[19] Yee, K. Numerical solution of initial boundary value problems involving maxwell's equations in isotropic media. *IEEE Transactions on Antennas and Propagation* **14**, 302–307 (1966).

[20] Zhu, Z. and Brown, T. G. Full-vectorial finite-difference analysis of microstructured optical fibers. *Opt. Express* **10**, 853–864 (2002).

[21] Makovejs, S., Roberts, C. C., Palacios, F., Matthews, H. B., Lewis, D. A., Smith, D. T., Diehl, P. G., Johnson, J. J., Patterson, J. D., Towery, C. R. and Ten, S. Record-low (0.1460 db/km) attenuation ultra-large aeff optical fiber for

submarine applications. *Proc. of Opt. Fiber Commun. Conf. and Exhib. (OFC)* 1–3 (2015).

[22] de Montmorillon, L. A., Bigot Astruc, M. and Sillard, P. Cutoff mechanisms in bend-insensitive single-mode fibers. In *Proc. of Opt. Fiber Commun. Conf. and Exhib. (OFC)* (Los Angeles, CA, USA, 2011).

[23] Fugihara, M. and Pinto, A. N. Attenuation fitting function. *Microw. Opt. Technol. Lett.* **51**, 2294–2296 (2009).

[24] Tsujikawa, K., Tajima, K., Shiraki, K. and Sankawa, I. Method for predicting rayleigh scattering loss of silica-based optical fibers. *J. Lightw. Technol.* **25**, 2122–2128 (2007).

[25] Snyder, A. W. Coupled-mode theory for optical fibers. *J. Opt. Soc. Am.* **62**, 1267–1277 (1972).

[26] Okamoto, K. Fundamentals of optical waveguides (second edition). 159–207 (Academic Press, Burlington, 2006).

[27] Miller, S. E. Coupled wave theory and waveguide applications. *The Bell System Technical Journal* **33**, 661–719 (1954).

[28] Tu, J., Saitoh, K., Koshiba, M., Takenaga, K. and Matsuo, S. Design and analysis of large-effective-area heterogeneous trench-assisted multi-core fiber. *Opt. Express* **20**, 15157–15170 (2012).

[29] Marcuse, D. Derivation of coupled power equations. *The Bell System Technical Journal* **51**, 229–237 (1972).

[30] Hayashi, T., Taru, T., Shimakawa, O., Sasaki, T. and Sasaoka, E. Design and fabrication of ultra-low crosstalk and low-loss multi-core fiber. *Opt. Express* **19**, 16576–16592 (2011).

[31] Koshiba, M., Saitoh, K., Takenaga, K. and Matsuo, S. Analytical expression of average power-coupling coefficients for estimating intercore crosstalk in multicore fibers. *IEEE Photon. J.* **4**, 1987–1995 (2012).

[32] Masanori, K., Kunimasa, S., Katsuhiro, T. and Shoichiro, M. Multi-core fiber design and analysis: coupled-mode theory and coupled-power theory. *Opt. Express* **19**, B102–B111 (2011).

[33] Hayashi, T., Nakanishi, T., Hirashima, K., Shimakawa, O., Sato, F., Koyama, K., Furuya, A., Murakami, Y. and Sasaki, T. 125-μm-cladding eight-core multi-core

fiber realizing ultra-high-density cable suitable for o-band short-reach optical interconnects. *J. Lightw. Technol.* **34**, 85–92 (2016).

[34] Takenaga, K., Arakawa, Y., Sasaki, Y., Tanigawa, S., Matsuo, S., Saitoh, K. and Koshiba, M. A large effective area multi-core fiber with an optimized cladding thickness. *Opt. Express* **19**, B543–B550 (2011).

[35] Imamura, K., Mukasa, K. and Yagi, T. Investigation on multi-core fibers with large aeff and low micro bending loss. In *Proc. of Opt. Fiber Commun. Conf. and Exhib. (OFC)* (San Diego, CA, USA, 2010).

[36] Katsunori, I., Kazunori, M. and Takeshi, Y. Effective space division multiplexing by multi-core fibers. In *Proc. of Eur. Conf. Opt. Commun. (ECOC)* (Torino, Italy, 2010).

[37] Imamura, K., Tsuchida, Y., Mukasa, K., Sugizaki, R., Saitoh, K. and Koshiba, M. Investigation on multi-core fibers with large aeff and low micro bending loss. *Opt. Express* **19**, 10595–10603 (2011).

[38] Hayashi, T., Taru, T., Shimakawa, O., Sasaki, T. and Sasaoka, E. Low-crosstalk and low-loss multi-core fiber utilizing fiber bend. In *Proc. of Opt. Fiber Commun. Conf. and Exhib. (OFC)* (Los Angeles, CA, USA, 2011).

[39] Takenaga, K., Sasaki, Y., Guan, N., Matsuo, S., Kasahara, M., Saitoh, K. and Koshiba, M. A large effective area few-mode multi-core fiber. In *IEEE Photonics Society Summer Topical Meeting Series*, 191–192 (2012).

[40] Luís, R. S., Rademacher, G., Puttnam, B. J., Semrau, D., Killey, R. I., Bayvel, P., Awaji, Y. and Furukawa, H. Crosstalk impact on the performance of wideband multicore-fiber transmission systems. *IEEE J. Select. Topics Quantum Electron.* **26**, 1–9 (2020).

[41] Carena, A., Bosco, G., Curri, V., Poggiolini, P., Taiba, M. T. and Forghieri, F. Statistical characterization of pm-qpsk signals after propagation in uncompensated fiber links. In *Proc. of Eur. Conf. Opt. Commun. (ECOC)* (Torino,Italy, 2010).

[42] Vacondio, F., Simonneau, C., Lorcy, L., Antona, J. C., Bononi, A. and Bigo, S. Experimental characterization of gaussian-distributed nonlinear distortions. In *Proc. of Eur. Conf. Opt. Commun. (ECOC)* (Geneva, Switzerland, 2011).

[43] Poggiolini, P., Carena, A., Curri, V., Bosco, G. and Forghieri, F. Analytical modeling of nonlinear propagation in uncompensated optical transmission links. *IEEE Photon. Technol. Lett.* **23**, 742–744 (2011).

[44] Carena, A., Bosco, G., Curri, V., Jiang, Y., Poggiolini, P. and Forghieri, F. Egn model of non-linear fiber propagation. *Opt. Express* **22**, 16335–16362 (2014).

[45] Poggiolini, P. The gn model of non-linear propagation in uncompensated coherent optical systems. *J. Lightw. Technol.* **30**, 3857–3879 (2012).

[46] Chen, X. and Shieh, W. Closed-form expressions for nonlinear transmission performance of densely spaced coherent optical ofdm systems. *Opt. Express* **18**, 19039–19054 (2010).

[47] Johannisson, P. and Karlsson, M. Perturbation analysis of nonlinear propagation in a strongly dispersive optical communication system. *J. Lightw. Technol.* **31**, 1273–1282 (2013).

[48] Serena, P. and Bononi, A. A time-domain extended gaussian noise model. *J. Lightw. Technol.* **33**, 1459–1472 (2015).

[49] Carena, A., Curri, V., Bosco, G., Poggiolini, P. and Forghieri, F. Modeling of the impact of nonlinear propagation effects in uncompensated optical coherent transmission links. *J. Lightw. Technol.* **30**, 1524–1539 (2012).

[50] Dar, R., Feder, M., Mecozzi, A. and Shtaif, M. Properties of nonlinear noise in long, dispersion-uncompensated fiber links. *Opt. Express* **21**, 25685–25699 (2013).

[51] Saavedra, G., Tan, M., Elson, D. J., Galdino, L., Semrau, D., Iqbal, M. A., Phillips, I. D., Harper, P., Ellis, A., Thomsen, B. C., Lavery, D., Killey, R. I. and Bayvel, P. Experimental analysis of nonlinear impairments in fibre optic transmission systems up to 7.3 thz. *J. Lightw. Technol.* **35**, 4809–4816 (2017).

[52] Semrau, D., Killey, R. and Bayvel, P. Achievable rate degradation of ultra-wideband coherent fiber communication systems due to stimulated raman scattering. *Opt. Express* **25**, 13024–13034 (2017).

[53] Semrau, D., Killey, R. I. and Bayvel, P. The gaussian noise model in the presence of inter-channel stimulated raman scattering. *J. Lightw. Technol.* **36**, 3046–3055 (2018).

[54] Semrau, D., Killey, R. and Bayvel, P. A closed-form approximation of the gaussian noise model in the presence of inter-channel stimulated raman scattering. *J. Lightw. Technol.* **37**, 1924–1936 (2019).

[55] Semrau, D., Galdino, L., Sillekens, E., Lavery, D., Killey, R. I. and Bayvel, P. Modulation format dependent, closed-form formula for estimating nonlinear

interference in s+c+l band systems. In *Proc. of Eur. Conf. Opt. Commun. (ECOC)* (Dublin, 2019).

[56] Stolen, R. H. and Ippen, E. P. Raman gain in glass optical waveguides. *Applied Physics Letters* **22**, 276–278 (1973).

[57] Tariq, S. and Palais, J. A computer model of non-dispersion-limited stimulated raman scattering in optical fiber multiple-channel communications. *Journal of Lightwave Technology* **11**, 1914–1924 (1993).

[58] Inao, S., Sato, T., Sentsui, S., Kuroha, T. and Nishimura, Y. Multicore optical fiber. In *Proc. of Opt. Fiber Commun. Conf. and Exhib. (OFC)* (Washington, D.C. United States, 1979).

[59] Naone, G. L., Boscher, D., Grosso, P., Bizeul, J. C. and Botton, C. Ultra high density cables using a new concept of bunched multicore monomode fibers : A key for the future ftth networks. In *The International Wire and Cable Symposium (IWCS)* (1994).

[60] Morioka, T. New generation optical infrastructure technologies: "exat initiative" towards 2020 and beyond. In *Proc. of Opto. Commun. Conf. (OECC)* (Hong Kong, China, 2009).

[61] Sillard, P., Benyahya, K., Soma, D., Labroille, G., Jian, P., Igarashi, K., Ryf, R., Fontaine, N. K., Rademacher, G. and Shibahara, K. Few-mode fiber technology, deployments, and systems. *Proceedings of the IEEE* **110**, 1804–1820 (2022).

[62] Kaneko, S., Sato, S., Kaji, T., Tomikawa, K. and Osato, K. Innovative solution using SWR / WTC for data centers. In *The International Cable Connectivity Symposium (IWCS)* (2018).

[63] Matsuo, S., Yamashiro, K., Tsujimoto, Y., Miyata, M., Murata, A., Ishikawa, T., Nakajima, T. and Osato, K. 1,728-fiber cable with 12-fiber ribbons comprising 160-μm-coating fiber with 80-μm cladding. *Journal of Lightwave Technology* **40**, 1552–1559 (2022).

[64] Hayashi, T., Sakamoto, T., Yamada, Y., Ryf, R., Essiambre, R.-J., Fontaine, N., Mazur, M., Chen, H. and Hasegawa, T. Randomly-coupled multi-core fiber technology. *Proceedings of the IEEE* **110**, 1786–1803 (2022).

[65] Matsui, T., Pondillo, P. L. and Nakajima, K. Weakly coupled multicore fiber technology, deployment, and systems. *Proceedings of the IEEE* **110**, 1772–1785 (2022).

[66] Imamura, K., Mukasa, K., Sugizaki, R., Mimura, Y. and Yagi, T. Multi-core holey fibers for ultra large capacity wide-band transmission. In *Proc. of Eur. Conf. Opt. Commun. (ECOC)* (Brussels, Belgium, 2008).

[67] Zhu, B., Taunay, T. F., Yan, M. F., Fini, J. M., Fishteyn, M., Monberg, E. M. and Dimarcello, F. V. Seven-core multicore fiber transmissions for passive optical network. *Opt. Express* **18**, 11117–11122 (2010).

[68] Takenaga, K., Arakawa, Y., Tanigawa, S., Guan, N., Matsuo, S., Saitoh, K. and Koshiba, M. Reduction of crosstalk by trench-assisted multi-core fiber. In *Proc. of Opt. Fiber Commun. Conf. and Exhib. (OFC)* (Los Angeles, CA, USA, 2011).

[69] Mukasa, K. 1,000-core fibers. In *Proc. of Opto. Commun. Conf. (OECC)* (Taipei, Taiwan, 2020).

[70] Sakamoto, T., Saitoh, K., Hanzawa, N., Tsujikawa, K., Ma, L., Koshiba, M. and Yamamoto, F. Crosstalk suppressed hole-assisted 6-core fiber with cladding diameter of 125 μm. In *Proc. of Eur. Conf. Opt. Commun. (ECOC)* (London, UK, 2013).

[71] Sagae, Y., Matsui, T. and Nakajima, K. Ultra-low-xt multi-core fiber with standard 125-μm cladding for long-haul transmission. In *Proc. of Opto. Commun. Conf. (OECC)* (Fukuoka, Japan, 2019).

[72] Gonda, T., Imamura, K., Sugizaki, R., Kawaguchi, Y. and Tsuritani, T. 125 μm 5-core fibre with heterogeneous design suitable for migration from single-core system to multi-core system. In *Proc. of Eur. Conf. Opt. Commun. (ECOC)* (Dusseldorf, Germany, 2016).

[73] Koshiba, M., Saitoh, K. and Kokubun, Y. Heterogeneous multi-core fibers: proposal and design principle. *IEICE Electronics Express* **6**, 98–103 (2009).

[74] Kumar, D. and Ranjan, R. Optimal design for crosstalk analysis in 12-core 5-lp mode homogeneous multicore fiber for different lattice structure. *Optical Fiber Technology* **41**, 95–103 (2018).

[75] Jiang, S., Ma, L., Velazquez, M. N., He, Z. and Sahu, J. K. Design of 125-μm cladding diameter multicore fibers with high core multiplexing factor for wideband optical transmission. *Opt. Fiber Technol.* **50**, 55–61 (2019).

[76] Xie, Y., Pei, L., Zheng, J., Zhao, Q., Ning, T. and Li, J. Impact analysis of a dense hole-assisted structure on crosstalk and bending loss in homogeneous few-mode multi-core fibers. *Opt. Express* **28**, 23806–23819 (2020).

[77] Sakaguchi, J., Puttnam, B. J., Klaus, W., Awaji, Y., Wada, N., Kanno, A., Kawanishi, T., Imamura, K., Inaba, H., Mukasa, K., Sugizaki, R., Kobayashi, T. and Watanabe, M. 19-core fiber transmission of 19×100×172-Gb/s SDM-WDM-PDM-QPSK signals at 305Tb/s. *Proc. of Opt. Fiber Commun. Conf. and Exhib. (OFC)* (2012).

[78] Hayashi, T., Nagashima, T., Yonezawa, K., Wakayama, Y., Soma, D., Igarashi, K., Tsuritani, T. and Sasaki, T. 6-mode 19-core fiber for weakly-coupled mode-multiplexed transmission over uncoupled cores. In *Proc. of Opt. Fiber Commun. Conf. and Exhib. (OFC)* (Anaheim, CA, USA, 2016).

[79] Sakaguchi, J., Puttnam, B. J., Klaus, W., Awaji, Y., Wada, N., Kanno, A., Kawanishi, T., Imamura, K., Inaba, H., Mukasa, K., Sugizaki, R., Kobayashi, T. and Watanabe, M. 305 tb/s space division multiplexed transmission using homogeneous 19-core fiber. *Journal of Lightwave Technology* **31**, 554–562 (2013).

[80] Amma, Y., Sasaki, Y., Takenaga, K., Matsuo, S., Tu, J., Saitoh, K., Koshiba, M., Morioka, T. and Miyamoto, Y. High-density multicore fiber with heterogeneous core arrangement. In *Proc. of Opt. Fiber Commun. Conf. and Exhib. (OFC)* (Los Angeles, CA, USA, 2015).

[81] Sakaguchi, J., Klaus, W., Mendinueta, J.-M. D., Puttnam, B., Luis, R., Awaji, Y., Wada, N., Hayashi, T., Nakanishi, T., Watanabe, T., Kokubun, Y., Takahata, T. and Kobayashi, T. Realizing a 36-core, 3-mode fiber with 108 spatial channels. In *Proc. of Opt. Fiber Commun. Conf. and Exhib. (OFC)* (Los Angeles, CA, USA, 2015).

[82] Sasaki, Y., Takenaga, K., Aikawa, K., Miyamoto, Y. and Morioka, T. Single-mode 37-core fiber with a cladding diameter of 248 μm. In *Proc. of Opt. Fiber Commun. Conf. and Exhib. (OFC)* (Optica Publishing Group, Los Angeles, CA, USA, 2017).

[83] Matsuo, S., Takenaga, K., Arakawa, Y., Sasaki, Y., Taniagwa, S., Saitoh, K. and Koshiba, M. Large-effective-area ten-core fiber with cladding diameter of about 200 μm. *Opt. Lett.* **36**, 4626–4628 (2011).

[84] Tu, J., Saitoh, K., Takenaga, K. and Matsuo, S. Heterogeneous trench-assisted few-mode multi-core fiber with low differential mode delay. *Opt. Express* **22**, 4329–4341 (2014).

[85] Takara, H., Sano, A., Kobayashi, T., Kubota, H., Kawakami, H., Matsuura, A., Miyamoto, Y., Abe, Y., Ono, H., Shikama, K., Goto, Y., Tsujikawa, K., Sasaki,

Y., Ishida, I., Takenaga, K., Matsuo, S., Saitoh, K., Koshiba, M. and Morioka, T. 1.01-pb/s (12 sdm/222 wdm/456 gb/s) crosstalk-managed transmission with 91.4-b/s/hz aggregate spectral efficiency. In *Proc. of Eur. Conf. Opt. Commun. (ECOC)* (Amsterdam, Netherlands, 2012).

[86] Sano, A. *et al.* 409-tb/s + 409-tb/s crosstalk suppressed bidirectional mcf transmission over 450 km using propagation-direction interleaving. *Opt. Express* **21**, 16777–16783 (2013).

[87] Sakaguchi, J., Klaus, W., Puttnam, B. J., Mendinueta, J. M. D., Awaji, Y., Wada, N., Tsuchida, Y., Maeda, K., Tadakuma, M., Imamura, K., Sugizaki, R., Kobayashi, T., Tottori, Y., Watanabe, M. and Jensen, R. V. 19-core mcf transmission system using edfa with shared core pumping coupled via free-space optics. *Opt. Express* **22**, 90–95 (2014).

[88] Puttnam, B. J., Luís, R. S., Klaus, W., Sakaguchi, J., Delgado Mendinueta, J.-M., Awaji, Y., Wada, N., Tamura, Y., Hayashi, T., Hirano, M. and Marciante, J. 2.15 pb/s transmission using a 22 core homogeneous single-mode multi-core fiber and wideband optical comb. In *Proc. of Eur. Conf. Opt. Commun. (ECOC)* (Valencia, Spain, 2015).

[89] Mishra, J. K., Rahman, B. M. A. and Priye, V. Rectangular array multicore fiber realizing low crosstalk suitable for next-generation short-reach optical interconnects with low misalignment loss. *IEEE Photonics Journal* **8**, 1–14 (2016).

[90] Hayashi, T., Mekis, A., Nakanishi, T., Peterson, M., Sahni, S., Sun, P., Freyling, S., Armijo, G., Sohn, C., Foltz, D., Pinguet, T., Mack, M., Kaneuchi, Y., Shimakawa, O., Morishima, T., Sasaki, T. and De Dobbelaere, P. End-to-end multi-core fibre transmission link enabled by silicon photonics transceiver with grating coupler array. In *2017 European Conference on Optical Communication (ECOC)*, 1–3 (2017).

[91] Tu, J., Saitoh, K., Amma, Y., Takenaga, K. and Matsuo, S. Heterogeneous trench-assisted few-mode multi-core fiber with graded-index profile and square-lattice layout for low differential mode delay. *Opt. Express* **23**, 17783–17792 (2015).

[92] Arikawa, M., Ito, T., Le Taillandier de Gabory, E. and Fukuchi, K. Crosstalk reduction using bidirectional signal assignment over square lattice structure 16-core fiber for gradual upgrade of ssmf-based lines. In *Proc. of Eur. Conf. Opt. Commun. (ECOC)* (Valencia, Spain, 2015).

[93] Sasaki, Y., Fukumoto, R., Takenaga, K., Aikawa, K., Saitoh, K., Morioka, T. and Miyamoto, Y. Crosstalk-managed heterogeneous single-mode 32-core fibre. In *ECOC 2016; 42nd European Conference on Optical Communication*, 1–3 (2016).

[94] Xie, X., Tu, J., Zhou, X., Long, K. and Saitoh, K. Design and optimization of 32-core rod/trench assisted square-lattice structured single-mode multi-core fiber. *Opt. Express* **25**, 5119–5132 (2017).

[95] Saitoh, K., Matsui, T., Sakamoto, T., Koshiba, M. and Tomita, S. Multi-core hole-assisted fibers for high core density space division multiplexing. In *OECC 2010 Technical Digest*, 164–165 (2010).

[96] Yao, B., Ohsono, K., Shiina, N., Fukuzato, K., Hongo, A., Sekiya, E. H. and Saito, K. Reduction of crosstalk by hole-walled multi-core fibers. In *Optical Fiber Communication Conference*, OM2D.5 (Optica Publishing Group, 2012).

[97] Nozoe, S., Fukumoto, R., Sakamoto, T., Matsui, T., Amma, Y., Takenaga, K., Tsujikawa, K., Aozasa, S., Aikawa, K. and Nakajima, K. Low crosstalk 125 μm-cladding multi-core fiber with limited air-holes fabricated with over-cladding bundled rods technique. In *2017 Optical Fiber Communications Conference and Exhibition (OFC)*, Th1H.6 (2017).

[98] Goto, Y., Tsujikawa, K., Aozasa, S., Sakamoto, T., Matsui, T., Nakajima, K. and Ohashi, M. Impact of air hole on crosstalk suppression and spatial core density of multi-core fiber. *J. Lightw. Technol.* **36**, 4819–4825 (2018).

[99] Mizuno, T., Kobayashi, T., Takara, H., Sano, A., Kawakami, H., Nakagawa, T., Miyamoto, Y., Abe, Y., Goh, T., Oguma, M., Sakamoto, T., Sasaki, Y., Ishida, I., Takenaga, K., Matsuo, S., Saitoh, K. and Morioka, T. 12-core × 3-mode dense space division multiplexed transmission over 40 km employing multi-carrier signals with parallel mimo equalization. In *Proc. of Opt. Fiber Commun. Conf. and Exhib. (OFC)* (Optica Publishing Group, San Francisco, CA, 2014).

[100] Li, Z., Wang, L., Wang, Y., Li, S., Meng, X., Guo, Y., Wang, G., Zhang, H., Cheng, T., Xu, W., Qin, Y. and Zhou, H. Manufacturable low-crosstalk high-RCMF 13-core 5-LP mode fiber with graded-index core and stairway-index trench. *Opt. Express* **29**, 26418–26432 (2021).

[101] Dai, Y., Wang, Y.-J., Tian, F., Zhang, Q. and Xin, X. Design and optimization of heterogeneous few-mode multi-core fiber with graded-index profile and trench/rod assisted. In *Asia Commun. and Photon. Conf. (ACP)* (Beijing, China, 2020).

[102] Kokubun, Y. and Koshiba, M. Novel multi-core fibers for mode division multiplexing: proposal and design principle. *IEICE Electronics Express* **6**, 522–528 (2009).

[103] Marcuse, D. Influence of curvature on the losses of doubly clad fibers. *Appl. Opt.* **21**, 4208–4213 (1982).

[104] Mukasa, K. 100-core fibers. In *Proc. of Opto. Commun. Conf. (OECC)* (Fukuoka, Japan, 2019).

[105] Tu, J., Long, K. and Saitoh, K. An efficient core selection method for heterogeneous trench-assisted multi-core fiber. *IEEE Photon. Technol. Lett.* **28**, 810–813 (2016).

[106] Wang, Y., Fujisawa, T., Sagae, Y., Sakamoto, T., Matsui, T., Nakajima, K. and Saitoh, K. A novel core allocation in heterogeneous step-index multi-core fibers with standard cladding diameter. *J. Lightw. Technol.* **39**, 7231–7237 (2021).

[107] Ishida, I., Akamatsu, T., Wang, Z., Sasaki, Y., Takenaga, K. and Matsuo, S. Possibility of stack and draw process as fabrication technology for multi-core fiber. In *2013 Optical Fiber Communication Conference and Exposition and the National Fiber Optic Engineers Conference (OFC/NFOEC)*, 1–3 (2013).

[108] Giraud, A., Sandoz, F. and Pelkonen, J. Innovation in preform fabrication technologies. In *2009 14th OptoElectronics and Communications Conference*, ThM1 (2009).

[109] Yamamoto, J., Yajima, T., Kinoshita, Y., Ishii, F., Yoshida, M., Hirooka, T. and Nakazawa, M. Fabrication of multi core fiber by using slurry casting method. In *Optical Fiber Communication Conference*, Th1H.5 (Optica Publishing Group, 2017).

[110] Nozoe, S., Fukumoto, R., Amma, Y., Sakamoto, T., Matsui, T., Takenaga, K., Abe, Y., Tsujikawa, K., Hanzawa, N., Aozasa, S., Aikawa, K., Ohashi, M. and Nakajima, K. Ultra-low crosstalk 125-μm-cladding four-hole four-core fibers fabricated by the over-cladding bundled rods method. *Journal of Lightwave Technology* **37**, 5600–5608 (2019).

[111] Blankenship, M. and Deneka, C. The outside vapor deposition method of fabricating optical waveguide fibers. *IEEE Transactions on Microwave Theory and Techniques* **30**, 1406–1411 (1982).

[112] Takahashi, M., Maeda, K., Sugizaki, R. and Tsukamoto, M. Multicore fiber fabricated by modified cylinder method. In *2020 Optical Fiber Communications Conference and Exhibition (OFC)*, Th2A.17 (2020).

[113] Cai, J. X., Batshon, H. G., Mazurczyk, M. V., Davidson, C. R., Sinkin, O. V., Wang, D., Paskov, M., Patterson, W. W., Bolshtyansky, M. A. and Foursa, D. G. 94.9 tb/s single mode capacity demonstration over 1,900 km with c+l edfas and coded modulation. In *2018 European Conference on Optical Communication (ECOC)*, 1–3 (2018).

[114] Sakaguchi, J., Awaji, Y., Wada, N., Kanno, A., Kawanishi, T., Hayashi, T., Taru, T., Kobayashi, T. and Watanabe, M. Space division multiplexed transmission of 109-tb/s data signals using homogeneous seven-core fiber. *Journal of Lightwave Technology* **30**, 658–665 (2012).

[115] Matsui, T. *et al.* 118.5 tbit/s transmission over 316 km-long multi-core fiber with standard cladding diameter. In *2017 Opto-Electronics and Communications Conference (OECC) and Photonics Global Conference (PGC)*, 1–2 (2017).

[116] Rademacher, G., Puttnam, B. J., Luís, R. S., Sakaguchi, J., Klaus, W., Eriksson, T. A., Awaji, Y., Hayashi, T., Nagashima, T., Nakanishi, T., Taru, T., Takahata, T., Kobayashi, T. and Furukawa, H. Multi-span transmission over 65 km 38-core 3-mode fiber. In *2020 European Conference on Optical Communications (ECOC)*, 1–4 (2020).

[117] Soma, D., Wakayama, Y., Beppu, S., Sumita, S., Tsuritani, T., Hayashi, T., Nagashima, T., Suzuki, M., Takahashi, H., Igarashi, K., Morita, I. and Suzuki, M. 10.16 peta-bit/s dense sdm/wdm transmission over low-dmd 6-mode 19-core fibre across c+l band. In *2017 European Conference on Optical Communication (ECOC)*, 1–3 (2017).

[118] Turukhin, A., Sinkin, O. V., Batshon, H. G., Zhang, H., Sun, Y., Mazurczyk, M., Davidson, C. R., Cai, J.-X., Bolshtyansky, M. A., Foursa, D. G. and Pilipetskii, A. 105.1 tb/s power-efficient transmission over 14,350 km using a 12-core fiber. In *2016 Optical Fiber Communications Conference and Exhibition (OFC)*, Th4C.1 (2016).

[119] Turukhin, A., Batshon, H. G., Mazurczyk, M., Sun, Y., Davidson, C. R., Chai, J.-X., Sinkin, O. V., Patterson, W., Wolter, G., Bolshtyansky, M. A., Foursa, D. G. and Pilipetskii, A. Demonstration of 0.52 pb/s potential transmission capacity over 8,830 km using multicore fiber. In *ECOC 2016; 42nd European Conference on Optical Communication*, 1–3 (2016).

[120] Mata, J., de Miguel, I., Durán, R. J., Merayo, N., Singh, S. K., Jukan, A. and Chamania, M. Artificial intelligence (ai) methods in optical networks: A comprehensive survey. *Optical Switching and Networking* **28**, 43–57 (2018).

[121] He, Z., Du, J., Chen, X., Shen, W., Huang, Y., Wang, C., Xu, K. and He, Z. Machine learning aided inverse design for few-mode fiber weak-coupling optimization. *Opt. Express* **28**, 21668–21681 (2020).

[122] Poletti, F., Finazzi, V., Monro, T. M., Broderick, N. G. R., Tse, V. and Richardson, D. J. Inverse design and fabrication tolerances of ultra-flattened dispersion holey fibers. *Opt. Express* **13**, 3728–3736 (2005).

[123] Parsonson, C. W. F., Shabka, Z., Chlupka, W. K., Goh, B. and Zervas, G. Optimal control of soas with artificial intelligence for sub-nanosecond optical switching. *Journal of Lightwave Technology* **38**, 5563–5573 (2020).

[124] Buglia, H., Sillekens, E., Vasylchenkova, A., Bayvel, P. and Galdino, L. On the impact of launch power optimization and transceiver noise on the performance of ultra-wideband transmission systems [invited]. *J. Opt. Commun. Netw.* **14**, B11–B21 (2022).

[125] Shevchenko, N. A., Nallaperuma, S. and Savory, S. J. Maximizing the information throughput of ultra-wideband fiber-optic communication systems. *Opt. Express* **30**, 19320–19331 (2022).

[126] Tanimura, T., Hoshida, T., Rasmussen, J. C., Suzuki, M. and Morikawa, H. Osnr monitoring by deep neural networks trained with asynchronously sampled data. In *OptoElectronics and Communications Conference (OECC) held jointly with International Conference on Photonics in Switching (PS)*, TuB3–5 (2016).

[127] Thrane, J., Wass, J., Piels, M., Diniz, J. C. M., Jones, R. and Zibar, D. Machine learning techniques for optical performance monitoring from directly detected pdm-qam signals. *Journal of Lightwave Technology* **35**, 868–875 (2017).

[128] Lau, A. P. T. and Kahn, J. M. Signal design and detection in presence of nonlinear phase noise. *Journal of Lightwave Technology* **25**, 3008–3016 (2007).

[129] Granada Torres, J. J., Chiuchiarelli, A., Thomas, V. A., Ralph, S. E., Cárdenas Soto, A. M. and González, N. G. Adaptive nonsymmetrical demodulation based on machine learning to mitigate time-varying impairments. In *2016 IEEE Avionics and Vehicle Fiber-Optics and Photonics Conference (AVFOP)*, 289–290 (2016).

[130] Karanov, B., Chagnon, M., Thouin, F., Eriksson, T. A., Bülow, H., Lavery, D., Bayvel, P. and Schmalen, L. End-to-end deep learning of optical fiber communications. *Journal of Lightwave Technology* **36**, 4843–4855 (2018).

[131] Martinelli, F., Andriolli, N., Castoldi, P. and Cerutti, I. Genetic approach for optimizing the placement of all-optical regenerators in wson. *J. Opt. Commun. Netw.* **6**, 1028–1037 (2014).

[132] Rubio Largo, A., Vega Rodriguez, M. A., Gomez Pulido, J. A. and Sanchez Perez, J. M. A comparative study on multiobjective swarm intelligence for the routing and wavelength assignment problem. *IEEE Transactions on Systems, Man, and Cybernetics, Part C (Applications and Reviews)* **42**, 1644–1655 (2012).

[133] Perelló, J., Gené, J. M., Pagès, A., Lazaro, J. A. and Spadaro, S. Flex-grid/sdm backbone network design with inter-core xt-limited transmission reach. *J. Opt. Commun. Netw.* **8**, 540–552 (2016).

[134] Fernández, N., Durán, R. J., de Miguel, I., Merayo, N., Aguado, J. C., Fernández, P., Jiménez, T., Rodríguez, I., Sánchez, D., Lorenzo, R. M., Abril, E. J., Angelou, M. and Tomkos, I. Survivable and impairment-aware virtual topologies for reconfigurable optical networks: A cognitive approach. In *2012 IV International Congress on Ultra Modern Telecommunications and Control Systems*, 793–799 (2012).

[135] Morales, F., Ruiz, M., Gifre, L., Contreras, L. M., López, V. and Velasco, L. Virtual network topology adaptability based on data analytics for traffic prediction. *J. Opt. Commun. Netw.* **9**, A35–A45 (2017).

[136] McCulloch, W. S. and Pitts, W. A logical calculus of the ideas immanent in nervous activity. *The bulletin of mathematical biophysics* **5**, 115–133 (1943).

[137] Nair, V. and Hinton, G. E. Rectified linear units improve restricted boltzmann machines. In *Proc. of International Conf. on Machine Learning (ICML)*, 807–814 (Madison, WI, USA, 2010).

[138] Kingma, D. P. and Ba, J. Adam: A method for stochastic optimization. In *3rd International Conference on Learning Representations, ICLR, San Diego, CA, USA* (2015).

[139] Friedman, J. H. Greedy function approximation: A gradient boosting machine. *The Annals of Statistics* **29**, 1189 – 1232 (2001).

[140] Lumerical. `https://www.lumerical.com/products/`.

[141] Eberhart, R. and Kennedy, J. Particle swarm optimization. In *Proc. of IEEE Int. Conf. on Neural Networks*, vol. 4, 1942–1948 (Perth, WA, Australia, 1995).

[142] Shi, Y. and Eberhart, R. A modified particle swarm optimizer. In *1998 IEEE International Conference on Evolutionary Computation Proceedings. IEEE World Congress on Computational Intelligence (Cat. No.98TH8360)*, 69–73 (1998).

[143] Clerc, M. and Kennedy, J. The particle swarm - explosion, stability, and convergence in a multidimensional complex space. *IEEE Transactions on Evolutionary Computation* **6**, 58–73 (2002).

[144] Carlisle, A. and Dozier, G. An off-the-shelf pso. In *Proc. of Workshop on Particle Swarm Optimization*, vol. 1, 1–6 (Indianapolis, Indiana, USA, 2001).

[145] Ratnaweera, A., Halgamuge, S. and Watson, H. Self-organizing hierarchical particle swarm optimizer with time-varying acceleration coefficients. *IEEE Transactions on Evolutionary Computation* **8**, 240–255 (2004).

[146] Wu, J., Song, C., Fan, C., Hawbani, A., Zhao, L. and Sun, X. Denpso: A distance evolution nonlinear pso algorithm for energy-efficient path planning in 3d uasns. *IEEE Access* **7**, 105514–105530 (2019).

[147] Bansal, J. C., Singh, P. K., Saraswat, M., Verma, A., Jadon, S. S. and Abraham, A. Inertia weight strategies in particle swarm optimization. In *2011 Third World Congress on Nature and Biologically Inspired Computing*, 633–640 (2011).

[148] Eberhart, R. and Shi, Y. Tracking and optimizing dynamic systems with particle swarms. In *Proceedings of the 2001 Congress on Evolutionary Computation (IEEE Cat. No.01TH8546)*, vol. 1, 94–100 vol. 1 (2001).

[149] Feng, Y., Teng, G.-F., Wang, A.-X. and Yao, Y.-M. Chaotic inertia weight in particle swarm optimization. In *Second International Conference on Innovative Computing, Informatio and Control (ICICIC 2007)*, 475–475 (2007).

[150] Zhan, Z.-H., Zhang, J., Li, Y. and Chung, H. S.-H. Adaptive particle swarm optimization. *IEEE Trans. on Systems, Man, and Cybernetics* **39**, 1362–1381 (2009).

[151] Hu, M., Wu, T. and Weir, J. D. An adaptive particle swarm optimization with multiple adaptive methods. *IEEE Transactions on Evolutionary Computation* **17**, 705–720 (2013).

[152] Jin, Y.-X., Cheng, H.-Z., yong Yan, J. and Zhang, L. New discrete method for particle swarm optimization and its application in transmission network expansion planning. *Electric Power Systems Research* **77**, 227–233 (2007).

[153] Omran, M., Engelbrecht, A. P. and Salman, A. Particle swarm optimization method for image clustering. *Int. J. of Pattern Recognition and Artificial Intelligence* **19**, 297–321 (2005).

[154] Elkamchouchi, H. M., Elragal, H. M. and Makar, M. A. Power control in cdma system using particle swarm optimization. In *National Radio Science Conf.*, 1–8 (Cairo, Egypt, 2007).

[155] Durand, F. R. and Abrão, T. Energy-efficient power allocation for wdm/ocdm networks with particle swarm optimization. *J. Opt. Commun. Netw.* **5**, 512–523 (2013).

[156] Sasaki, Y., Amma, Y., Takenaga, K., Matsuo, S., Saitoh, K. and Koshiba, M. Trench-assisted low-crosstalk few-mode multicore fiber. In *Proc. of Eur. Conf. Opt. Commun. (ECOC)*, 1–3 (London, UK, 2013).

[157] Sakai, J. and Kimura, T. Bending loss of propagation modes in arbitrary-index profile optical fibers. *Appl. Opt.* **17**, 1499–1506 (1978).

[158] Gené, J. M. and Winzer, P. J. A universal specification for multicore fiber crosstalk. *IEEE Photon. Technol. Lett.* **31**, 673–676 (2019).

[159] Sagae, Y., Matsui, T., Sakamoto, T. and Nakajima, K. Ultra-low crosstalk multi-core fiber with standard 125-μm cladding diameter for 10,000km-class long-haul transmission. *IEICE Transactions on Communications* 1199–1205 (2020).

[160] Puttnam, B. J., Luís, R. S., Rademacher, G., Awaji, Y. and Furukawa, H. 319 tb/s transmission over 3001 km with s, c and l band signals over $>$120nm bandwidth in 125 μm wide 4-core fiber. In *Proc. of Opt. Fiber Commun. Conf. and Exhib. (OFC)*, 1–3 (2021).

[161] Wang, Y., Fujisawa, T., Sakamoto, T., Matsui, T., Nakajima, K. and Saitoh, K. Step index 8-core fiber with 125-μm cladding diameter for o-band use. In *Proc. of Opto. Commun. Conf. (OECC)*, 1–3 (2020).

[162] Matsuo, S., Takenaga, K., Sasaki, Y., Amma, Y., Saito, S., Saitoh, K., Matsui, T., Nakajima, K., Mizuno, T., Takara, H., Miyamoto, Y. and Morioka, T. High-spatial-multiplicity multicore fibers for future dense space-division-multiplexing systems. *Journal of Lightwave Technology* **34**, 1464–1475 (2016).

[163] Vudathu, S. P., Boning, D. and Laur, R. A critical enhancement in the yield analysis of microsystems. In *2007 IEEE International Reliability Physics Symposium Proceedings. 45th Annual*, 422–428 (2007).

[164] Stoneking, D., Bilbro, G., Trew, R., Gilmore, P. and Kelley, C. Yield optimization using a GaAs process simulator coupled to a physical device model. In *Proceedings IEEE/Cornell Conference on Advanced Concepts in High Speed Semiconductor Devices and Circuits*, 374–383 (1991).

[165] El-Kareh, B., Ghatalia, A. and Satya, A. Yield management in microelectronic manufacturing. In *Proceedings. of 45th Electronic Components and Technology Conference*, 58–63 (1995).

[166] Schenkel, F., Pronath, M., Zizala, S., Schwencker, R., Graeb, H. and Antreich, K. Mismatch analysis and direct yield optimization by spec-wise linearization and feasibility-guided search. In *Proceedings of the 38th Design Automation Conference (IEEE Cat. No.01CH37232)*, 858–863 (2001).

[167] Lanza, M., Smets, Q., Huyghebaert, C. and Li, L.-J. Yield, variability, reliability, and stability of two-dimensional materials based solid-state electronic devices. *Nature Communications* **11**, 5689 (2020).

[168] Buglia, H., Jarmolovičius, M., Vasylchenkova, A., Sillekens, E., Galdino, L., Killey, R. I. and Bayvel, P. A closed-form expression for the gaussian noise model in the presence of inter-channel stimulated raman scattering extended for arbitrary loss and fibre length. *Journal of Lightwave Technology* **41**, 3577–3586 (2023).

[169] van Uden, R. G. H., Correa, R. A., Huyghebaert, C., Lopez, E. A., Huijskens, F. M., Xia, C., Li, G., Schülzgen, A., de Waardt, H., Koonen, A. M. J. and Okonkwo, C. M. Ultra-high-density spatial division multiplexing with a few-mode multicore fibre. *Nature Photonics* **8**, 865–870 (2014).

[170] Knight, J. C., Birks, T. A., Russell, P. S. J. and Atkin, D. M. All-silica single-mode optical fiber with photonic crystal cladding. *Opt. Lett.* **21**, 1547–1549 (1996).

[171] Smith, D. R., Padilla, W. J., Vier, D. C., Nemat-Nasser, S. C. and Schultz, S. Composite medium with simultaneously negative permeability and permittivity. *Phys. Rev. Lett.* **84**, 4184–4187 (2000).

[172] Kerrinckx, E., Bigot, L., Douay, M. and Quiquempois, Y. Photonic crystal fiber design by means of a genetic algorithm. *Opt. Express* **12**, 1990–1995 (2004).

[173] Ghorbani, F., Beyraghi, S., Shabanpour, J., Oraizi, H., Soleimani, H. and Soleimani, M. Deep neural network-based automatic metasurface design with a wide frequency range. *Scientific Reports* **11**, 7102 (2021).